CHARLES UNIVERSITY, FACULTY OF SCIENCE
INSTITUTE OF PETROLOGY AND STRUCTURAL GEOLOGY

Reconstruction of the geological evolution of the Southern Main Ethiopian Rift

Rekonstrukce geologického vývoje jižní části hlavního etiopského riftu

Diploma MSc. Thesis

Diplomová práce

Bc. Štěpán Dvořák

Supervised by:

Doc. RNDr. Kryštof Verner, Ph.D.

Prague, May 2022

Acknowledgment

I would like to express my gratitude to the people who helped and supported me in my geology studies, inspired me, and shared their knowledge with me. First of all, I would like to thank to my supervisor, doc. RNDr. Kryštof Verner, Ph.D. for his advice and comments that helped me in elaborating this thesis, as well as for his kindly attitude and for giving me the opportunity to participate on geological mapping in Ethiopia. I would also like to thank to Mgr. Karel Martínek, Ph.D. for assistance on data processing in ArcGIS, Mgr. Otmar Petyniak, and Ing. Petra Hejtmánková for the digitization of the geological maps. Further, I would like to express my gratitude to RNDr. Jiří Málek, Ph.D. for his help on calculating paleostress, Mgr. Jan Valenta, Ph.D. for great assistance on processing the geophysical data, and Mgr. David Buriánek, Ph.D. for his assistance on processing the chemical analyzes. I would like to express my gratitude to the employees of the Institute of Petrology and Structural Geology for making such a great environment in which is a pleasure to learn and work, further to Mgr. Martin Racek, Ph.D. and RNDr. Radim Jedlička, Ph.D. for their assistance on using electron microscope. I thank the Czech Development Agency for funding mapping projects in Ethiopia and colleagues participating in this project. Last but not least, I would like to thank my friends and family for their support, especially my parents, who constantly support me not only during my studies, which I truly appreciate, and finally to my partner Tamara for her support and being my motivation.

Poděkování

Touto cestou chci vyjádřit svoji vděčnost lidem, kteří mi pomáhali a podporovali mě v mých studiích geologie, inspirovali mě a dělili se semnou o své znalosti. V prvé řadě chci poděkovat vedoucímu mé práce doc. RNDr. Kryštofu Vernerovi, Ph.D. za jeho rady a připomínky, které pomohly při zpracování této diplomové práce, rovněž za přátelský přístup a možnosti podílet se na geologickém mapování v Etiopii. Dále chci poděkovat Mgr. Karlovi Martínkovi, Ph.D. za pomoc při zpracování dat v programu ArcGIS, Mgr. Otmaru Petyniakovi a Ing. Petře Hejtmánkové za digitalizaci geologických map. Rovněž RNDr. Jiřímu Málkovi, Ph.D. za pomoc při výpočtu paleonapětí, Mgr. Janu Valentovi, Ph.D. za značnou pomoc při zpracování geofyzikálních dat, a Mgr. Davidovi Buriánkovi, Ph.D. za pomoc při zpracování chemických analýz. Také chci vyjádřit svůj vděk pracovníkům Ústavu petrologie a strukturní geologie za skvělé prostředí, ve kterém je radost se vzdělávat a pracovat, dále Mgr. Martinu Rackovi, Ph.D. a RNDr. Radimu Jedličkovi, Ph.D. za asistenci s elektronovým mikroskopem. Děkuji České rozvojové agentuře za financování mapovacích projektů v Etiopii a kolegům účastnících se na tomto projektu. V neposlední řadě bych chtěl poděkovat svým kamarádům a rodině za jejich podporu, především mým rodičům, kteří mě neustále podporují nejen v dobách studia, čehož si nesmírně vážím, a na závěr mé partnerce Tamaře, která mě podporuje a je pro mě motivací.

Declaration:

I declare that I am author of this diploma thesis and I have cited all resources used in its preparation. Neither this thesis nor its substantial part has been submitted to fulfill requirements for other master or any other academic degree.

Prohlášení:

Prohlašuji, že jsem tuto diplomovou práci vypracoval samostatně a výhradně s použitím citovaných pramenů, literatury a dalších odborných zdrojů. Tato práce ani její podstatná část nebyla předložena k získání jiného nebo stejného akademického titulu.

In Prague, May 10th, 2022

Abstract:

The Main Ethiopian Rift represents a unique insight into process of continental rifting and its comprehensive research can provide partial clarification of open questions such are the causes, mechanisms, and timing of overall tectonic and magmatic evolution. The Main Ethiopian Rift is an intermediary between the Afar triple junction to the north and Kenyan Rift to the south, representing incipient plate boundary between Nubian and Somalian plates. Based on comprehensive geological research of the northern flank of the Southern Main Ethiopian Rift including field geological and structural mapping, petrological and geochemical description of individual lithologies, morphotectonic analysis of Digital Elevation Model, paleostress analysis and gravity pattern assessment including calculation of Linsser indices, some aspects in geodynamic evolution of northern flank of the Southern Main Ethiopian Rift is interpreted. The area recorded typical continental rift-related tectonic and magmatic evolution including "pre-rift" (Eocene to Oligocene) volcanic activity initiated by extensive flood (plateau) alkaline basalt to trachybasalt basalt eruptions due to crustal thinning and mantle plume(s) ascent, followed by fault-dominated "early-rift" (Miocene) bimodal volcanism associated with origin of the rift valley and "late-rift" (Pliocene to Holocene) bi-modal volcanic activity comprising alternation of alkaline basalts and alkaline to subalkaline rhyolite to trachyte lava flows, formation of numerous lava domes, cinder cones, calderas and large deposition of felsic pyroclastic material. Principal faults and fault zones are mostly vertical, parallel with the NNE(N)–SSW(S) oriented rift axis and prominent morphological escarpments, bearing steeply plunging slickensides and normal kinematic indicators. Subordinate faults are steeply to moderately dipping with ~WNW–ESE trend associated with well-developed steeply to moderately plunging slickensides and normal to oblique-slip kinematics. The regional paleostress field reflects the continuing rifting between the Nubian and Somalian plate, in the succession of earlier E–W extension (N90°) direction, changing to E(ENE)–W(WSW) extension (N80°), gently oblique to the rift-axis.

Keywords: continental rift, petrology, tectonics, paleostress analysis, volcanic activity

Abstrakt:

Hlavní etiopský rift představuje unikátní pohled do procesu kontinentálního riftingu a jeho komplexní výzkum může částečně objasnit otevřené otázky, jako jsou příčiny a mechanismy tektonického a magmatického vývoje v čase. Hlavní etiopský rift spojuje afarský trojný bod na severu s keňským riftem na jihu, představuje hranici mezi núbijskou a somálskou deskou. Na základě komplexního geologického výzkumu severního okraje jižního segmentu hlavního etiopského riftu, včetně terénního geologického a strukturního mapování, petrologické a geochemické charakteristiky jednotlivých litologií, morfotektonické analýzy digitálního modelu reliéfu, paleonapjatostní analýzy, a posouzení mapy tíhových anomálií, včetně výpočtu linsserových horizontálních gradientů, jsou interpretovány některé aspekty

geodynamického vývoje severního okraje jižního segmentu hlavního etiopského riftu. Tato oblast zaznamenala charakteristický tektonický a magmatický vývoj související s kontinentální extenzí, včetně předriftové (Eocén až Oligocén) vulkanické aktivity, iniciované rozsáhlými výlevy alkalických plató bazaltů až trachybazaltů, v důsledku ztenčování kůry a vzestupu plášťové plumy. Navazující zlomová aktivita rané vývojové fáze riftu (Miocén) a bimodálního vulkanismu je spjata se vznikem riftového struktury. Během pokročilé fáze vývoje riftu (Pliocén až Holocén) bimodální vulkanická aktivita zahrnuje střídající se výlevy alkalických bazaltů, alkalických až subalkalických ryolitů až trachytových lávových proudů, tvořící četné lávové dómy, struskové kužele, kaldery a mocné vrstvy kyselého pyroklastického materiálu. Většina zlomů je převážně strmé orientace, které probíhají rovnoběžně s osou riftu ve směru SSV(S)–JJZ(J). Tyto zlomy tvoří výraznou morfologii, které nesou indikátory poklesové kinematiky. Menší část zlomů je orientována ve směru ~ZSZ–VJV, přičemž upadají pod strmými až středními úhly. Tyto zlomové plochy obsahují strmě až středně orientované striace s indikátory poklesové kinematiky. Regionální paleonapjatostní pole odráží extenzi mezi núbijskou a somálskou deskou ve směru hlavní osy extenze V-Z (90°) a následnou změnou v její orientaci ve směru V(VSE)–Z(ZJZ) (80°), kose k ose riftu.

Klíčová slova: kontinentální rift, petrologie, tektonika, palonapjatostní analýza, vulkanická aktivita

Table of content

1. **Introduction** 1

2. **Geological settings** 4

   2.1. The East African Rift System 4

   2.2. The Main Ethiopian Rift 11

3. **Methodology** 18

4. **Lithology and Petrology** 21

   4.1. Basement Rocks 22

   4.2. “Pre-rift” Volcanic Deposits 25

   4.3. “Early” Volcanic Deposits 29

   4.4. “Late rift” Volcanic Deposits 31

5. **Morphotectonic Analysis** 49

6. **Tectonics** 51

   6.1. Primary Structures 51

   6.2. Brittle Tectonics 52

   6.3. Paleostress Analysis 54

   6.4. Gravimetry 55

7. **Geochemistry** 60

   7.1. Basic Rocks 60

   7.2. Acid Rocks 61

8. **Discussion** 63

   8.1. Field Geological Mapping and Lithological Pattern 63

   8.2. Geochemistry 64

   8.3. Paleostress Analysis and Tectonic Evolution 64

   8.4. Gravimetry 65

9. **Conclusions** 67

1. Introduction

The process of rifting encompasses complex interplay between mantle dynamics, lithosphere behavior and plate tectonic stresses. It's a process of stretching of the lithosphere, leading to its extension, and thinning. The rifting comprises divergent type of plate boundary, i.e., two lithospheric plates are moving away from each other. The rift valleys represents continental scale linear fractures, bounded by normal faults, as a result of extension tectonic regime (Kearey et al., 2009; Pluijm and Marshack, 2004; Stüwe, 2007). The term rift was firstly used by the British geologist and explorer John Walter Gregory in his pioneer study from 1894, where he studied the Great Rift Valley, also called the East African Rift System (Gregory, 1894). The rift structure can form either symmetrical valley in form of "graben" which is commonly bounded by parallel normal fault dipping towards the valley center on each side or asymmetric valley "halfgraben" as the valley is bounded only on one side. The lithosphere can extend either perpendicular to the rift axis or in acute angle, in case of oblique rift (Pluijm and Marshack, 2004). The process of continental rifting encompasses several evolution stages, starting from pre-rift stage and ending with oceanic rift stage with seafloor spreading (e.g., Chorowicz, 2005; Chorowicz et al., 1987; Ebinger, 2005; Hayward and Ebinger, 1996). The whole process of rifting begins with rift initiation, following by continental break-up, and terminates with sea floor spreading, i.e., rift-drift transition lasting about 20 to 60 Ma (Pluijm and Marshack, 2004). If the forces causing the stretching aren't sufficient enough in any stage of rifting, the extension stops, and the rift become inactive. These rifts are called failed or unsuccessful and the inactive rift structure is called aulacogen (Ebinger, 2005; Pluijm and Marshack, 2004).

As the Earth is tectonically evolving, it has recorded many rifts within the continental crust during its geological history. Besides the best-known example of continental rift and still ongoing the East African Rift System, another examples of rifts are the European Cenozoic Rift System, Basin and Range, the West Antarctic Rift System, the Baikal Rift, the Oslo Rift, and many others (Olsen, 1995; Şengör and Natal'in, 2001). There are two types of continental rifting, passive and active. The passive rifting mechanism is related with forces generated at plate margins. The active rifting mechanism is associated with mantle plume upwelling causing weakening and fracturing of the lithosphere (Sengör and Burke, 1978; Turcotte and Emerman, 1983). Rifts tend to appear in pre-existing zones of weakness, which allows the easiest pathways of propagation of fractures (Corti, 2009 and references therein; Versfelt and Rosendahl, 1989). Further, their development is strongly affected by presence of magmatism (Corti et al., 2003a).

There are two main widely accepted models explaining development of the rift. McKenzie (1978) proposed a model of the development of the rift basin via pure shear stretching of the lithosphere in upper parts of crust, accompanied with passive mantle upwelling, resulting in symmetric rift valley. On the other hand model proposed by Wernicke (1981) deals with

deeply faulting up to mantle level as a consequence of simple shear, resulting in asymmetric rift valley. It is also worth pointing out that process of rifting takes place not only on Earth, but also on extraterrestrial objects like Mars, Venus or Jupiter's moon Ganymede (Hauber et al., 2010; Ivanov and Head, 2015; Lucchitta et al., 1994; Pizzi et al., 2017).

The main aim of the MSc. thesis focuses on the northern flank of the Southern Main Ethiopian Rift (SMER), as the internal part of the NNE–SSW trending East African Rift System with the extent through whole East Africa. The Main Ethiopian Rift is intermediary between the Afar triple junction to the north and Kenyan Rift to the south, representing incipient plate boundary between Nubian and Somalian plate. Therefore, it's an unique opportunity to study and understate the process of continental rifting (e.g. Corti, 2009). Despite the fact of more than 100 years of research focused both on EARS and MER, several statements still remain unclear (e.g., the timing of rift initiation and extension as well as relationships and contribution of magmatism and faulting on strain accommodation, changes in paleostress during the rifting and also some aspects of geochemical and thermal changes during the volcanic activity (e.g. Corti, 2009; Ebinger, 2005).

This MSc. thesis thematically follows the bachelor thesis entitled "Tectonic and magmatic evolution of the Main Ethiopian Rift" and develops this topic in terms of its own research project, which included a wider range of field and laboratory methods, in the crucial area of northern flank of the Southern Main Ethiopian Rift between the towns of Sodo, Awassa and Daye in the northern Sidama Region and Wolayta Zone in southern Ethiopia (for location see Annex-4).

Using field geological and structural mapping on a 1 : 50,000 scale resulted in compilation of geological maps on a 1: 250,000 scale (Annex-1, Annex-2), detailed petrological and geochemical characterization of mapped lithologies, morphotectonic analysis of Digital Elevation Model (DEM), paleostress analysis calculated based on rift-related normal faults with slickensides, and gravity pattern assessment including calculation of Linsser indications, the entire geodynamic and magmatic evolution of northern flank of the SMER is interpreted.

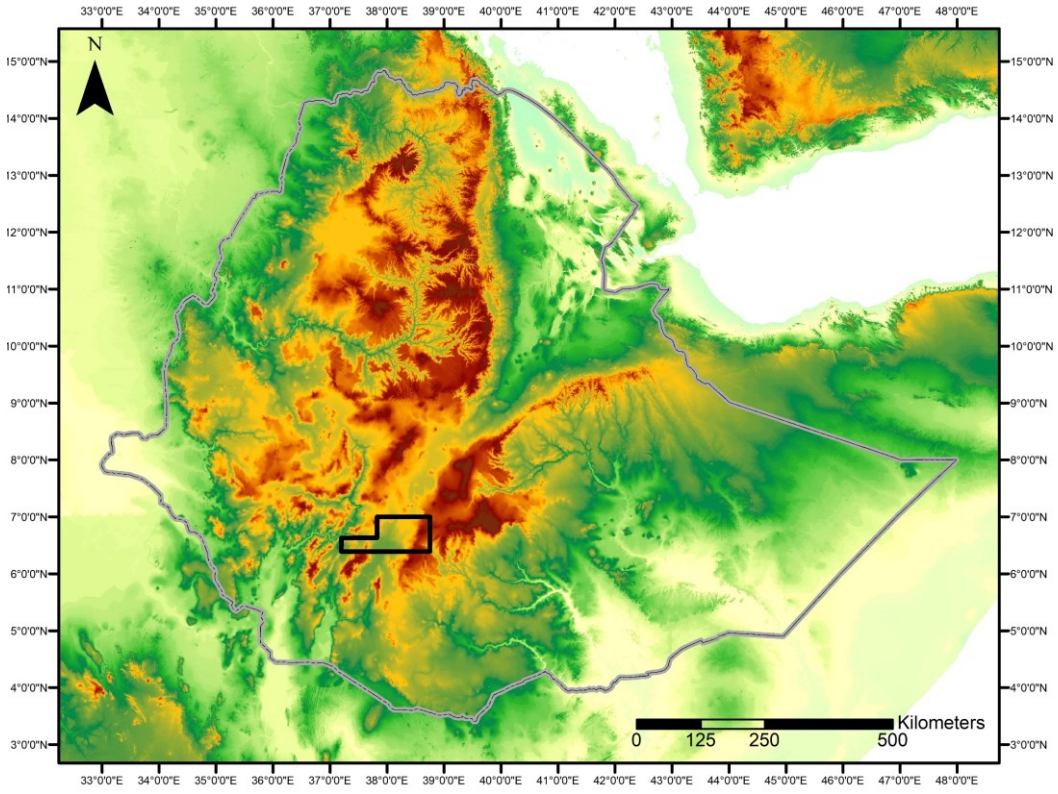

Figure 1-1. Digital Elevation Model of Ethiopia with the location of study area.

2. Geological settings

2.1. The East African Rift System

Characteristics

The East African Rift System (EARS) is AN intra-continental rift system progressively going from Afar Triple Junction to the Mozambique Channel in south-southwest direction (Figure 2-1). The EARS is ca. 5000 km long divergent plate boundary between Nubian (Africa), Somalian and Arabian plate (Jestin et al., 1994; La Rosa et al., 2021; Saria et al., 2014; Chorowicz, 2005, 1992; Stamps et al., 2008; Wolfenden et al., 2004).

The EARS can be divided into two main branches, Eastern and Western (Chorowicz, 2005; Rosendahl, 1987). The Eastern branch represents more evolved stage of rifting in comparison with the Western branch (Olsen, 1995; Ring, 2014). The least evolved part is the Southeastern branch (Chorowicz, 2005). Further, the rift valley is divided into individual rift basins. The Eastern branch includes the lower half of Afar, the Main Ethiopian Rift, Turkana Rift, Kenyan Rift, and Tanzanian Divergence Zone. The Western branch is separated by lakes Albert, Edward, Kivu, Rukwa, Tanganiyka, and Malawi (Chorowicz, 2005; Ring, 2014). The Southeastern branch is composed of offshore basins (Franke et al., 2015; Mougenot et al., 1986). The overall rift valley is composed of series of graben basins bounded by steep border faults or volcanic products (Chorowicz, 2005).

The boundary between Nubian and Somalian plate is manifested by seismic activity (Jestin et al., 1994; Kebede and Kulhánek, 1991). Based on seismic data, the EARS show shallow earthquakes with average focal dept of 20 km with dominantly normal faulting (Kebede and Kulhánek, 1991; Saemundsson, 2010). The whole rift system propagates southwards which could be expressed by decrease of seismic activity, lack of prominent active faults and decrease of the extension rate along Eastern branch in southern direction (Fairhead and Henderson, 1977; Kebede and Kulhánek, 1991; Stamps et al., 2008).

Geological Background and Lithology of the East African Rift System

The development of the East African Rift System is still under ongoing debate (Macgregor, 2015). The rift evolution is preceded by long and complex geological history. The basement of EARS is set on Archean-Proterozoic continental lithosphere, chiefly composed of metamorphic rocks (Ebinger, 1989; Yirgu et al., 2006). Inherited crustal anisotropies strongly controls the evolution of the rift system (Chorowicz, 1992; Hetzel and Strecker, 1994). Especially Precambrian belts, which EARS tend to follow, facilitate propagation of the rift. On the other hand, rift tends to avoid Archean cratons, representing cold and rigid crust, which rift is unable to propagate through (Chorowicz, 1992).

The Eastern branch follows structures of the Mozambique Belt in north-south direction (Hetzel and Strecker, 1994; McConnell, 1972), which resulted in continental collision of East and West Gondwana during Pan-African orogeny (Hetzel and Strecker, 1994; Shackleton, 1986). The Western branch follows mostly Early to Middle Proterozoic belts, representing quite rigid crust (Ring, 2014).

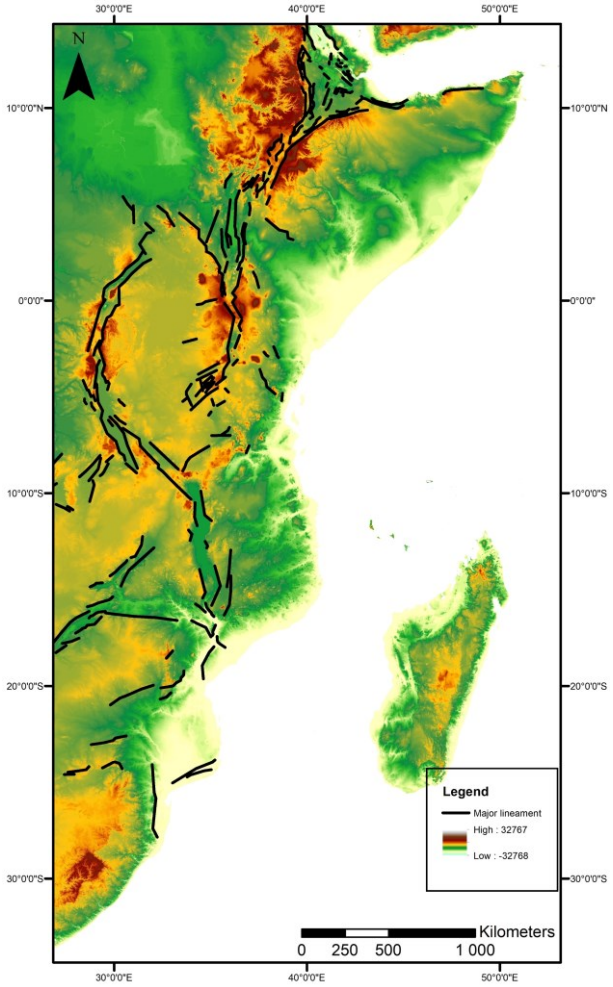

Figure 2-1. Digital Elevation Model of the East African Rift System with major lineaments.

Evolution of the East African Rift System

The evolution of EARS was further affected by former rift systems (also strongly influenced by former structures). During (late Carboniferous) Early-Jurassic to Cretaceous time, the rift system was affected by the Karroo Rift System and later by Central African Rift System. These structures were lately reactivated, especially in Malawi Rift (Castaing, 1991; Ring, 1994; Rosendahl, 1987). One of the greatest contribution on the evolution of the rift has the magmatic activity, causing weakening of the lithosphere (Agostini et al., 2011). From global tomography, there is evident zone beneath Africa, more than 1000 km wide of decrease in

velocity of seismic waves. This zone is referred as African Large Low Shear Velocity Province (LLSVP; Rooney, 2017; Zhao, 2001).

The development of the East African Rift System is associated with impact of mantle plume or plumes. The LLSVP anomaly under Africa generate large number of mantle plumes, causing upwelling of the asthenospheric mantle along EARS. This fact leads to heating of the lithosphere and subsequently uplifting, thinning of the lithosphere and pressure-release magmatism and extension (Ebinger and Sleep, 1998; Grand et al., 1997; Ring, 2014 and references therein).

The EARS records all rift stages from initial phase of rifting to mid ocean ridge and sea floor spreading. Individual rift segments represent different stages of rifting process. The initiation of rifting in EARS had several nucleus centers, starting in Afar and Kenyan Rift, each propagating southwards (Chorowicz, 2005, 1992; Hayward and Ebinger, 1996).

The Afar represents transition between continental rifting and initial seafloor spreading and therefore the most evolved phase of rifting of EARS. The mid-oceanic ridge is already developed, producing new oceanic crust. The upper half of Afar belongs to rift-rift-rift triple junction between Red sea, Gulf of Aden and the East African Rift System, the bottom half is part of the Main Ethiopian Rift (Hayward and Ebinger, 1996; Wolfenden et al., 2004). This area could be referred as oceanic rift phase (Chorowicz et al., 1987). The rifting was initiated in Red Sea around 29.9 to 28.7, after that in Gulf of Aden ca. 27.5 to 23 Ma (Chorowicz, 2005; Hughes et al., 1991). The rifting in northern part of the Main Ethiopian Rift started around 11 Ma, giving rise to the triple junction (Wolfenden et al., 2004). The presence of tension fractures allowed differentiation of alkaline volcanism and first apparition of oceanic material (Baker and Wohlenberg, 1971). The Main Ethiopian Rift represents advanced rift-stage (Chorowicz, 2005; Chorowicz et al., 1987). The deformation is progressively moving from major border faults into the center of the rift valley (Agostini et al., 2011).

As the rift propagating southward, in general, it becomes less and less developed, but this differ from individual segments in the rift system (Chorowicz et al., 1987). In this direction, the rift valley is composed of well-defined graben with uplifted shoulders, filled by water and thick succession of sediments. The subsidence is quite rapid, most of the deformation is localized along the major normal faults with minor strike-slip component. Northern Tanganyika together with northern part of the Western branch of EARS corresponds to the typical rift phase (Chorowicz, 2005; Chorowicz et al., 1987).

Moving to the younger stages of rifting, the initial-rift phase has more pronounced the strike-slip component, creating rhomb-shaped basins, bordered by major faults. Each basin is separated by transform faults, subsidence is still evident. Volcanism appears only if tension gashes are open, in that case, it is dominantly alkaline to peralkaline. This rift phase can be found in Malawi Rift (Chorowicz, 2005; Chorowicz et al., 1987).

The least developed stage of rifting is referred as pre-rift phase. Pre-rift phase is marked by fracturing with strike-slip faulting and formation of tension gashes, serving a channel for later volcanism, graben is not evolved yet. The volcanic activity is minor with chiefly tholeiitic hyperalkaline trend. This stage corresponds to the Limpopo in Southern Africa (Chorowicz, 2005; Chorowicz et al., 1987).

Link between evolution of the East African Rift System and humankind

The development of the East African Rift System and evolution of the Homo species share close time and spatial relationship. The EARS become an important area for study hominid evolution, as it yields fossils of hominids. As the EARS was evolving, it created a habitat suitable for human species within the rift valley. The tectonic regime, doming and volcanic activity, had created a barrier, in which the humans were evolving. The rift floor become specific environment in terms of climate isolation, vegetation, prey, and predator interactions (Bailey et al., 2000; Chorowicz, 2005; Leakey, 1973).

Magmatism of the East African Rift System

First magmatism related to the EARS appeared in Southern Ethiopia and Northern Kenya (Turkana Rift) from 45 to 34 Ma, composed primarily of basaltic volcanism. This period of time corresponds to the pre-rift magmatism and its related to the activity of the mantle plume(s) (George, 1998; George and Rogers, 2002; Rooney, 2017). This episode occurred ca. 20 Ma before any extension (Ebinger and Sleep, 1998; Ring, 2014). The pre-rift magmatism was dominated by basaltic volcanism (George, 1998; Rooney, 2017).

The most significant phase of magmatism related to the EARS commenced between 33.9 to 27 Ma, known as Oligocene Traps. This extensive volcanic activity affected area from lake Turkana to Sudan, Somali and Yemen, covering 1 to 2 km thick succession of mainly basaltic volcanic products (Chorowicz et al., 1998; Rooney, 2017). These flood basalt were erupted at area of more than 1000 km in diameter, in relatively short period of time of 1 Ma or even less, giving rise to the development of the Ethiopian and Somalian volcanic plateaus (Ebinger and Sleep, 1998; Rochette et al., 1998; Rooney, 2017; Ukstins et al., 2002). This phase is probably linked to initial extension of the lithosphere in Afar area and therefore with initiation of the East African Rift System (Ebinger et al., 1993b). This massive volcanic activity is also associated with extinction event marking the boundary between the Eocene and Oligocene epochs (Ayalew et al., 2002; Hofmann et al., 1997 and references therein). However, it is uncertain if there was only one or more mantle plumes. Ebinger and Sleep (1998) suggest single large mantle plume, which has migrated southwards. On the other hand, George (1998) suggest two mantle plumes contributing EARS magmatism.

Soon after the initial basaltic event, the magmatism was accompanied by rhyolitic volcanism dated to 30.2 Ma, as a result of the interaction of the mantle plume and melts derived from

the continental lithosphere causing changes in magma composition from mafic to bimodal (Ayalew et al., 2002; Rooney, 2017; Ukstins et al., 2002). Later on, magmatic activity was relatively reduced, only in Turkana the volcanism persisted (Brown and Mcdougall, 2011; Rooney, 2017). Between 29.9 to 22 Ma, the basaltic activity was again renewal, mainly in the Somalian Plateau in form of fissural basalts and shield volcanoes in the Ethiopian Plateau with intense magmatic activity in Turkana (Rooney, 2017 and references therein). Since Pliocene, the rhyolitic volcanism had occurred together with basalts, trachytes, phonolites, and nephelinites. In late Pliocene and Quaternary, the trachytic volcanism was focused in the center of the rift floor (Chorowicz, 2005; Woldegabriel et al., 1990). In Western branch of EARS, the volcanic activity has commenced episodically in several segregated segments at ca. 12 Ma in northern part, to 7 Ma, in the southern part (Ebinger, 1989; Pasteels et al., 1989). These volcanic products are potassium rich, enriched in incompatible elements and highly silica undersaturated (Rogers, 2006; Rogers et al., 1992).

The volcanic activity started to be focused mainly towards the rift floor and margins in Mid-Miocene in Afar and Early Pliocene in Kenyan Rift with many active central volcanoes (Baker and Wohlenberg, 1971; Mohr et al., 1972).

The present-day volcanic and magmatic activity is focused in chiefly in Eastern branch of the East African Rift System (Chorowicz, 2005; Ring, 2014; Wolfenden et al., 2004), especially in Afar, northern part of the Ethiopia and Kenya via basaltic eruptions (Mohr et al., 1972). In the Northern Tanzania, nephelinite-carbonatite volcano of Ol Doinyo Lengai still produce carbonatite lava and ash since Quaternary (Mohr et al., 1972).

In general, the magmatic and volcanic activity is aligned along rift axis on extensional fractures with several exceptions off-axis volcanism, for example Mt. Kenya or in the rift shoulders in the Main Ethiopian Rift (Chorowicz, 2005; Corti et al., 2004; Korme et al., 1997). The off-axis volcanism could be related to pre-existing weakness zones (Bosworth 1987; Korme et al. 1997) or by the orthogonal rifting as the magma is squeezed laterally, causing an off-axis emplacement (Corti et al., 2004). The volcanic activity in the Eastern branch of EARS is more prominent and produce much bigger volumes of magmatic product in comparison with the Western branch of EARS (Ring, 2014; Rogers, 2006).

Nubian and Somalian Kinematics

The present-day kinematic of the East African Rifts System remains unclear. The Nubian Somalian plate boundary follows ancient preexisting zones of weakness, focusing the strain with combination of microplates involved in plate models (Calais et al., 2006; Fernandes et al., 2004; Jestin et al., 1994; Saria et al., 2014; Stamps et al., 2008). This divergent plate boundary goes from Afar (roughly 11°N) up to Mozambique (roughly 20°S) (Fernandes et al., 2004). Modern plate motion models include not only the interaction between two plates; Nubian (African) and Somalian but assume relationship between at least three microplates; Lwandle,

Rovuma, and Victoria (Fernandes et al., 2004; Saria et al., 2014; Stamps et al., 2008). Since the first investigation attempts up to the present, in order to determine the extension direction in which African continent is opening, nearly all possible directions of extension were supposed. The kinematics in whole EARS was changing in time and vary from segment to segment (Bosworth et al., 1992; Bosworth and Strecker, 1997; Chorowicz, 2005; Delvaux et al., 1992). Nevertheless, from overall fault pattern and geometry of the whole EARS, the principal extension is in general in the E–W direction.

The direction, in which the rift system is moving along the axis, is in general well established. The whole rift system propagates southwards, which is supported by decrease in seismic activity from north to the south together with decrease of the extension rate along the Eastern branch (Kebede and Kulhánek, 1991; Oxburgh and Turcotte, 1974; Stamps et al., 2008). Oxburgh and Turcotte (1974) estimate the EARS propagate southwards at a mean rate of 2.5 cm/year, while Kampunzu and Mohr (1991) estimate the rate to be twice as big.

The amount of total separation of the African plate is also under debate (Corti, 2009). The lowest value of separation was estimated ca. 23 km for past 11 Ma (Lemaux et al., 2002) on the contrary Royer et al. (2006) suggest ca. 130 to 190 km of separation for same period of time. The most often estimated values of separation are around 30 to 40 km (Corti, 2009 and references therein). DeMets and Merkouriev (2016) conclude 40 to 50 km of separation in the Main Ethiopian Rift, which is consistent with geophysical data, Ebinger et al. (1993) suppose the amount of separation to cannot be less than 25 km in case of the Main Ethiopian Rift. The lowest value of displacement is in the Southeastern branch, where the total extension is less than two kilometers (DeMets and Wilson, 2008).

Nocquet et al. (2006) estimate the maximum extension rate of the Nubian and Somalian plate motion to be 4.7 to 6.7 mm/year in the Northern Ethiopia. Similar values were determined by Fernandes et al. (2004) in Afar to be 6.9 mm/year. Slowest rate of extension were estimated in the Nubian-Somalian-Antarctica triple junction to be ca 2 mm/year (Fernandes et al., 2004). Similar values were obtained by Chu and Gordon (1999). In general the rate of extension decreases southwards (Calais et al., 2006; Saria et al., 2014; Stamps et al., 2021, 2008). Saria et al. (2014) conclude the decrease of extension rate southwards, where in the southernmost part it reaches less than 1 mm/year.

Previous study conclude strain accommodation along narrow areas of bounding plates (Saria et al., 2014). Most recent study of Stamps et al. (2021) conclude the main part of deformation to be accommodated via ca. 600 km broad zone between Somalian and Rovuma plate, which indicate extending of the rift system across both branches trough individual rift segments. Modern studies show steady relative motion between Somalian and Nubian plate for last 3 Ma (Nocquet et al., 2006; Stamps et al., 2008). Most recent study of Stamps et al. (2021) show

slow rotation of Somalian plate with the rate of 0.076°/Ma and rotation of Lwandle microplate at rate of 0.045°/Ma.

2.2. The Main Ethiopian Rift

Overall Characteristics

The Main Ethiopian Rift (MER) belongs to the northernmost part of the East African Rift System (Ebinger, 2005) which connects the Afar-Red Sea-Gulf of Aden (rift-rift-rift triple junction) on the north with Kenyan Rift to the south (Fig. 2-2) (Corti, 2009; Wolfenden et al., 2004). The MER represents nascent plate boundary between Nubian and Somalian plate as it is in the break-up stage (Corti, 2009, 2008; Philippon et al., 2014). This rift segment is the key part in terms of understanding of the evolution of EARS, since it records all rift stages from initiation of rifting to the magmatic-rift stage, up to incipient sea floor spreading (Figure 2-2) (Corti, 2009; Ebinger, 2005; Keir et al., 2006). Its widely considered as the best place for studying the ongoing process of rifting with active volcanic and seismic activity (Corti, 2009; Corti et al., 2013; Wolfenden et al., 2004).

The Main Ethiopian Rift forms a symmetrical graben with uplifted shoulders and steep border faults (Woldegabriel et al., 1990). The MER is commonly divided into three parts, Northern, Central and Southern segment (Figure 5-1). The individual segments represents different rift phases, they vary from fault architecture, strain localization, and ages of the volcanic activity (e.g., Agostini et al., 2011; Corti, 2009; Hayward and Ebinger, 1996). The MER progressively propagates in NE–SW to N–S direction from ca 11.5°N to ca 5°N with total length about 1000 km and width about 80 km (Corti, 2009; Korme et al., 1997). The elevation within the rift floor descent from the highest values of 1700 m in Lake Ziway (Corti, 2009), up to 155 m below sea level in Lake Assal in Afar. The average elevation of the rift floor is about 1600 m (Korme et al., 1997). The MER propagates through the Ethiopian and Somalian Plateaus made of uplifted basement rocks, overlying sedimentary sequences, and Eocene-Recent basalts (Boccaletti et al., 1998; Woldegabriel et al., 1990).

The Main Ethiopian Rift is manifested by complex fault pattern. The MER comprise two types of normal faults (the border faults and rift floor related Wonji Fault Belt, WFB) (Agostini et al., 2011; Boccaletti et al., 1999, 1998; Corti, 2008). In general, border faults of MER show large vertical offset with high angle and their orientation vary within individual segments. On the top parts, they make flat shoulder with elevation ca. 2200 m, where volcanic complexes reach elevation up to 4200 m.

The Wonji Fault Belt (WFB) are active tectomagmatic segments with right-stepping en-echelon N–S to NNE–SSW trending direction (Boccaletti et al., 1998; Pizzi et al., 2006). These segments accommodate the vast majority of strain extension (ca. 80%) and corresponds to oblique rifting (Bilham et al., 1999; Corti, 2009, 2008). The extension is probably caused by magma-induced faulting (Bastow et al., 2005; Corti, 2008; Keranen et al., 2004; Pizzi et al., 2006). These structures obliquely cut the rift floor with respect to the major border faults and are closely

spaced arranged in sigmoidal shape (Boccaletti et al., 1998; Corti, 2009). The WFB were active during Pleistocene, commonly related with intense magmatic (volcanic) activity. These segments are set on the strongly thinned lithosphere which allows the pathways for magma intrusion trough fissures (Agostini et al., 2011; Boccaletti et al., 1998). Keranen et al. (2004) interpreted these structures as protoridges axis which will eventually become centers for future seafloor spreading. Their size of WFB reach up to 60 km in length and 20 km in width (Ebinger and Casey, 2001) and their presence decreases southwards (Agostini et al., 2011).

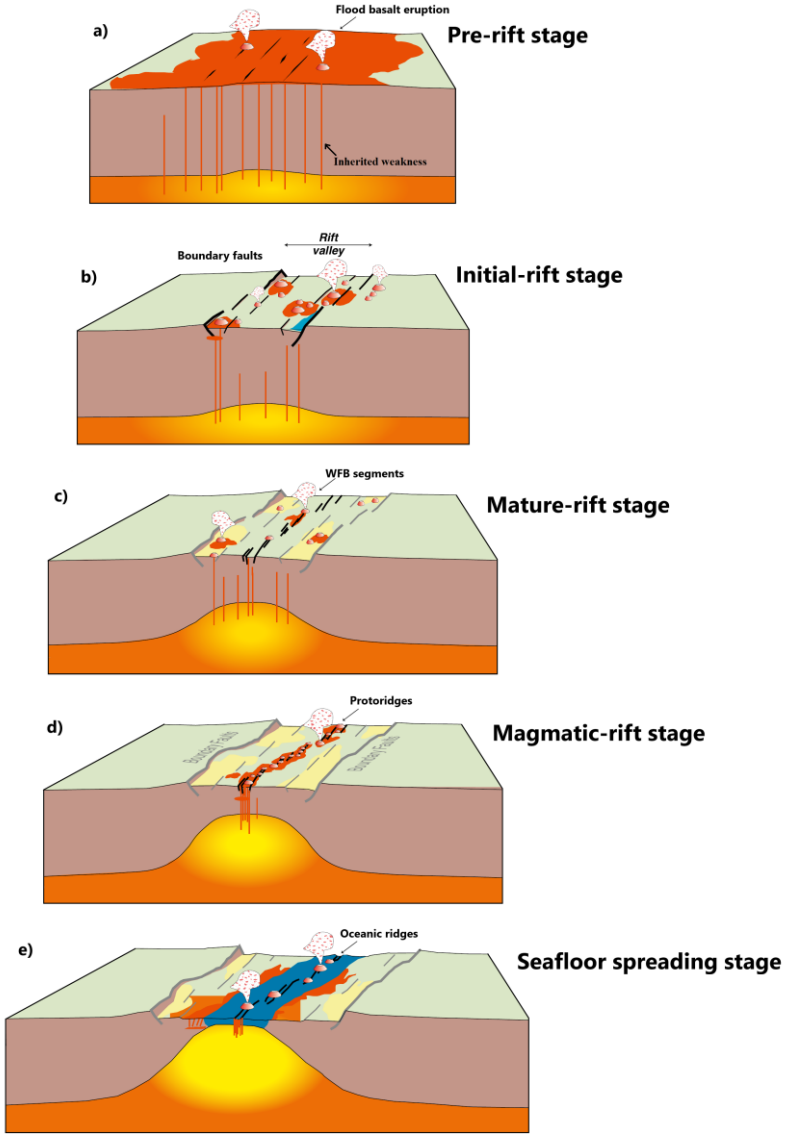

Figure 2-2. Schematic evolution model of the Main Ethiopian Rift, modified after Corti and Manetti (2012), nomenclature after (Chorowicz et al., 1987; Corti, 2009). (a) Pre-rift flood basalt eruption via pre-existing zone of weakness; (b) Extension along main boundary faults with syn-rift volcanism; (c) Strain migration from main border fault to the rift valley center and activation of the Wonji Fault Belt (WFB); (d) Strain localized into magmatic segments and accommodated via diking and faulting; (e) Progressively lithospheric thinning and heating, rupture of lithosphere leading into seafloor spreading with new oceanic lithosphere creation

Regional Classification of the Main Ethiopian Rift

Northern Segment (NMER)

The northern segment of the Main Ethiopian Rift (NMER) propagates through southern Afar depression, reaching up to the Lake Koka, where the Boru Toru Structural High separates this segment from CMER (Bonini et al., 2005; Corti, 2009). The Afar represents probably the most researched area withing the whole EARS. The NMER is bounded by Arboye and Asela-Sire border faults to the east (Wolfenden et al., 2004). The Asela-Sire border fault is diminishing southwards. The NMER is characterized by the ~N30°–N40° trending border faults (Agostini et al., 2011; Corti, 2009; Erbello et al., 2016). These marginal faults are overprinted by later minor faults and are mainly inactive. The western margin of NMER is not separated by major border fault, but rather by right stepping en-echelon faults. (Agostini et al., 2011; Corti, 2009; Keir et al., 2006). In the north-west part of NMER, Ankober border fault separates the MER from the Red Sea Rift (Wolfenden et al., 2004). The valley of NMER show asymmetric graben tilted to the southeast towards Arboye fault (Wolfenden et al., 2004). In general, the NMER segment trends in NE (~50°–55°) direction (Agostini et al., 2011). The thickness of the crust differs about 5 km from rift shoulder to its center valley. The thickness of the crust along the rift axis reaches about 25 km in the area of Afar/NMER boundary and thickens up to 35 km along NMER/CMER boundary (Corti, 2009 and references therein).

Central Segment (CMER)

In the CMER, the eastern shoulder is bounded by Langano-Asela border fault, the western shoulder is marked by Guraghe and Fonko border faults. These border faults results in more or less symmetrical rift valley (Boccaletti et al., 1998; Bonini et al., 2005; Corti, 2009). The major border faults trends ~N25°–N30° (Agostini et al., 2011). Near Lake Langano, the border fault is affected by rhomboidal shape structures (Boccaletti et al., 1998). The western part of CMER margin is extensively cover by syn-rift volcanoclastic product and lavas (Boccaletti et al., 1998 and references therein). The western margin of CMER is affected by quite extensive oblique-slip en-echelon sinistral structures (Boccaletti et al., 1998). The overall trend of CMER is ~N30°–40°E (Agostini et al., 2011). The crust in CMER reach up to 40 km in thickness (Corti, 2009 and references therein).

Southern Segment (SMER)

In case of SMER (southern segment of MER), the border faults display variation in their orientation. Agostini et al. (2011) subdivide SMER according to the trend of border faults into SMERn (northern segment of SMER) with ~N20°–25° trend and SMERs (southern segment of SMER) with ~N0°–15° trend. The Southern segment of MER is bounded by N–S to NE–SW trending Chenca border fault on the west and by NNE–SSW trending Agere Selam major border fault to the east (Corti, 2009). The whole MER progressively narrows southwards from

NE–SW to N–S direction (Agostini et al., 2011; Boccaletti et al., 1998; Ebinger et al., 1993b; Korme et al., 1997), especially in SMER in the Lake Abaya, where the whole MER reaches the narrowest point**.** The SMER splits into two near parallel rift valleys by ~100 km long Pre-Cambrian Amaro Horst into Chamo or Ganjuli Basin to the west and Galana Basin to the east (Corti, 2009; Ebinger et al., 2000, 1993b; Levitte et al., 1974). Both basins are bounded by steep faults trending in ~N–S direction. In case of the Galana Basin, the faults bounding the basins are liner, whereas in the Chamo Basin, the bounding faults are segmented and show zig-zag pattern. These structures are also preserved in the Chew Bahir Basin and they are related to inherited structures (Corti, 2009; Ebinger et al., 2000, 1993b). The crustal thickness in SMER is suggested to be ~30 km and decrease southwards (Dugda et al., 2005).

The geological mapping and investigations within SMER are sparse. The only regional geological of map of the Dila map sheet, covering most of the Sidama Region was compiled at a scale of 1: 250,000 by the Geological Survey of Ethiopia (Yismaw et al., 2015). Several geological studies of northern part of Abaya Lake were constrained (Chernet, 2011, EIGS-GEP, 1981), updated by (Corti et al., 2013). Further, more detailed investigation creating set of geoscience maps on a scale 1: 50,000 (sub-sheets Awassa, Leku, Mejo and Dila) was done in frame of the development projects financed by the Czech Republic in the years 2012 to 2018 (Rapprich et al., 2014; Hroch et al., 2018; Verner et al., 2018; Buriánek et al., 2018).

Ethiopian – Kenyan Rift Transition

The Main Ethiopian Rift on its southern segment terminates into so called Broadly Rifted Zone (BRZ), which is a region of ca 300 km wide zone of basins and ranges, where both Ethiopian and Kenyan Rift overlap. The BRZ is result of southward propagation of SMER and northwards propagation of Kenyan-Turkana Rift (Ebinger et al., 2000, 1993b). The BRZ is set just between 2 large uplifted zones – Ethiopian Plateau and Kenyan Dome (Pik et al., 2008). The Ethiopian Plateau is attributed with Afar mantle plume activity. The Kenyan Dome is characterized with uplift, which caused an increase of elevation about 1.5 to 2 km. This uplift event might be associated with lithospheric thinning during rifting process (Gani et al., 2007). According to Gani et al. (2007), the uplift event is associated with mantle plume and commenced through 3 pulses, starting from 29 to 10 Ma, 10 to 6 Ma, and from 6 Ma to present. The crust beneath the SMER and Kenyan Rift vary from 37 to 38 km (Dugda et al., 2005). Similar values were obtained by Maguire et al. (2006).

Geological Setting of the Main Ethiopian Rift

Pre-rift Evolution of the Main Ethiopian Rift

The Main Ethiopian Rift is set on the Arabian-Nubian Pre-Cambrian Shield, part of East African Orogeny, composed of highly metamorphosed rocks (e.g., Stern, 2002, 1994). The Precambrian basement in Ethiopia can be subdivided into three units; the oldest Lower

Complex, composed mainly of high-grade biotite amphibolite gneiss and migmatites, cropping out in Southern Ethiopia. The Middle Complex is built by metasediments and ophiolites, aligned in N–S to NE-SW direction, same direction as propagation of MER. This suture is a result of Tibetan-style continental collision. Further, these rocks were affected by shearing, thrusting, and faulting. The uppermost part of Pre-Cambrian basement is least deformed and comprise of carbonates, sediments and metavolcanites indicating back-arc basin succession (Abdelsalam and Stern, 1996; Kazmin et al., 1978; Korme et al., 2004; Stern, 1994).

During Paleozoic period, long lasting peneplanation caused denudation of nearly entirely mountain ridge (Corti, 2009; Gani et al., 2009; Korme et al., 2004). The Paleozoic sequences are rather rare in Ethiopia, representing regional unconformity. The Paleozoic period is restricted in the Northern Ethiopia in form of sedimentary strata (Korme et al., 2004). As supercontinent Gondwana was breaking off during Mesozoic Era, several rift branches developed, and affected the area between the Horn of Africa and Madagascar. This extension created tectonic basins, allowing shallow sea deposition, especially NE–SW trending Karoo rift during Early Permian (Guiraud et al., 2005). During Jurassic to Cretaceous, the rifting was ongoing and resulted in the Central African Rift System. This activity is manifested by creating NW–SE troughs of Blue Nile, Anza, Melut and Muglad Rift (Corti, 2009). Thick marine succession of sandstones, argillites and gypsum were developed showing repetitively transgressive and regressive succession, as this area was subsidenced and uplifted between Permian and Cretaceous period (Korme et al., 2004). These NW–SE striking rift basins were lately inverted and rejuvenated up to the Paleogene (Corti, 2009).

All of these pre-rift processes and structures created pre-existing zones of weakness and heavily affected the evolution of the Main Ethiopian rift and the whole East African Rift System sensu stricto (Chorowicz, 1992; Corti, 2009; Hetzel and Strecker, 1994; Kazmin et al., 1978; Korme et al., 2004).

Magmatic Activity of the Main Ethiopian Rift

The Main Ethiopian Rift is associated with an extensive volcanic activity (Corti, 2009 and references therein). The volcanic activity related to the rift occurred in several pulses and can be divided into two main events “pre-rift” volcanism and “syn-rift” volcanic activity. The “syn-rift” volcanism can be further subdivided into “early-rift” volcanism and “late-rift” volcanism.

Pre-rift magmatic event

The volcanic activity started by pre-rift flood-basalt event at ca 45 to 35 Ma. These transitional tholeiite basalts, known as Amaro-Gamo Basalts, were erupted with borders of Southern Ethiopia and Kenya (Ebinger et al., 2000, 1993b; George and Rogers, 2002). During late-Eocene, a massive and rapid volcanic event had affected the Afar. The eruption of traps, known as Ethiopian-Yemen flood basalts, is associated with the impact of the Afar mantle

plume (Coulié et al., 2003; Hofmann et al., 1997; Pik et al., 1998). This event is linked with the initiation of rifting in Red Sea, Gulf of Aden, and EARS (Courtillot et al., 1999). The resulting eruption covered area of more than 750 000 km^2 with thickness normally reaching 500 to 1500 m, locally more than 2 km (Coulié et al., 2003; Hofmann et al., 1997). This eruption was so enormous than had an impact on climate change and caused significant extinction (Hofmann et al., 1997 and references therein). Based on dating done by Hofmann et al. (1997), this eruption commenced between 31 to 28 Ma with significant concentration between 30 and 29 Ma.

This flood basalt event has resulted in building up Ethiopian and Somalian Plateaus and caused uplifting. According to Gani et al. (2007), the 2 km uplift of plateau had commenced simultaneously with major volcanic event. The volcanic plateau consists of several volcanic centers of tholeiite and alkaline basalts varying in timing of eruption (Kieffer et al., 2004). The traps are accompanied with rhyolites, ignimbrites and minor trachytes on the top of the flood basalts (Ayalew et al., 2002). These rhyolites were dated by Prave et al. (2016) and yield ages around 31 Ma. The volcanic activity related with Ethiopian traps switch into syn-rift bimodal at 25.3 Ma in the Afar, caused by the interaction of Afar plume with African lithosphere (Rooney, 2017). During that time, between 24 and 20 Ma, a dramatic quiescence of volcanic activity occurred and only volcanic activity was limited by less significant shield volcanoes (Rooney, 2017; Ukstins et al., 2002). The volcanic activity within Afar was later restored and appeared via fissural basalt eruption and shield building events (Kieffer et al., 2004; Rooney, 2017). The earliest volcanism within NMER commenced at 24 to 23 Ma by eruption of pre-rift flood basalts (Chernet et al., 1998).

The Amaro-Gamo unit is unconformly followed by Getra-Kele Basalts, the second episode of flood volcanism. These alkalic basalts were erupted between 19 to 11 Ma (Ebinger et al., 1993b; George, 1998; George and Rogers, 2002), simultaneously with the extension in Southern Ethiopia. The Getra-Kele Basalts are related with synchronous development of SMER. The Getra-Kele Basalts makes ca. 500m thick layer (George, 1998; George and Rogers, 2002). According to study of George and Rogers (2002), the Getra-Kele Basalts were derived from a lithospheric mantle source, enriched by migrating carbonate-rich melts. Between 18 to 14 Ma, the Amaro Horst in SMER was being uplifted (Ebinger et al., 1993a, 1993b).

The Getra-Kele unit is interbedded by fluvio-lacustrine strata in Chamo Basin, yielding ages ranging from 17 to 15 Ma (Ebinger et al., 1993b; WoldeGabriel et al., 1991). This unit is intruded by trachytic to syenitic volcanic, yielding ages of 13.7 to 13.7 Ma along with the border fault of the Chamo and Galana basins (Ebinger et al., 1993b). The uppermost part of this unit is covered by slightly younger ~12 to 11 Ma alkali basalts and hawaiites (WoldeGabriel et al., 1991).

Syn-rift magmatic event

After volcanic quiescence, syn-rift bimodal volcanism occurred at around 10 Ma via basalts and rhyolites as a result of westward migration of the Gulf of Aden. From 7 to 5 Ma, significant volcanism related to southwards migration of the Afar mantle plume commenced and was focused within WFB (Chernet et al., 1998; Hayward and Ebinger, 1996; Wolfenden et al., 2004). The bimodal volcanism in NMER, focused in the rift floor, remained until Quaternary, whereas in Afar, the ongoing volcanism is dominated by basalts with new oceanic crust being produced (Kendall et al., 2005; Rooney, 2020; Wolfenden et al., 2004).

The detailed study on CMER lithology, based on dating and stratigraphy correlation, was done by Woldegabriel et al. (1990), where they recognize 6 main volcanic event commencing within CMER, each separated by a hiatus. First volcanic activity started with voluminous Ethiopian flood basalts in Early-Oligocene, followed by Shebele Trachytes, yielding ages from 17 to 12 Ma, and later by Guraghe Basalts, with ages ranging from 10.25 to 8.4 Ma (Bonini et al., 2005; Woldegabriel et al., 1990; WoldeGabriel et al., 1991). These basalts and trachybasalts series are covered by widespread peralkaline pantelleritic ignimbrites yielding ages from 5 to 4.1 Ma and can be correlate with the Nazret Group of widespread volcanic unit within rift floor (Bonini et al., 2005).

The volcanic activity in the Southern segment of MER is modest in comparison with the other segments. The Quaternary to Recent volcanic activity is bimodal and mainly focused in the rift valley (Philippon et al., 2014). One of the youngest succession is represented by widespread Nech Sar olivine basalts yield ages of 1.34 to 0.77 Ma and related trachybasalt of Bobem Volcano, dated ca. 0.66 Ma, and Tosa Sucha volcano (Bridge of God), which may have erupted in historic time (Ebinger et al., 1993b). These basalt are synchronous with those in NMER, represented by Wonji Fault Belt-related basalts, but in comparison with them, they are much more alkaline, probably due to lower extension, which affects the magma evolution (Bonini et al., 2005 and references therein). Bonini et al. (2005) explained the restoration of volcanic activity in SMER as a result of reactivation of Kenyan Rift-related structures, induced by southward MER propagation along rift axis.

The youngest volcanic products are represented by calderas complexes, from north to south, Fentale, Kone, Boset-Bericha, Gedemsa, Tullu Moye, Aluto Shala, and Corbetti calderas in the rift floor, which some of them were erupted in historical times (Fontijn et al., 2018; Rapprich et al., 2016).

3. Methodology

Fieldwork and Data Collection

All of the data were obtained during field geological mapping of the Sidama Region and Gamo Zone in 1: 50,000 scale (in the period from January 2020 to December 2021) resulted in compilation of geological, soil and hydrogeological maps on a 1: 100,000 scale (Verner and Megerssa eds., in print) as a result of development aid project "Ensuring Sustainable Land Management in Selected Areas of Ethiopia on the Basis of Geoscientific Mapping", financed by Czech Development Agency. As a member of the scientific team, I have contributed on field data collection, rock sampling and preparation for analytical works, overall interpretation of the data and geological map compilation. All observation points and analyzed samples used in this thesis are listed in Table 8 and electronical supplementary Table 3.

The geological maps on scale of 1: 250,000 cover the area of northern Sidama Region and easternmost part of Wolayta Zone (Annex 1) and northern part of Gamo Zone (Annex 2) in Southern Ethiopia. The study area is located in Southern Ethiopia, ranging between ~7° and 6°23' north latitudes, and 37° 19' and 38° 75' east longitudes. These maps were compiled using the methodology according to Hanžl and Verner (eds.), (2018), in frame of my MSc. thesis, with the assistance of supervisor Mr. Kryštof Verner and later digitalized with the help of GIS expert from the Czech Geological Survey Mrs. Petra Hejtmánková and Mr. Otmar Petyniak.

Petrography and Microanalysis

Eleven thin sections were prepared by the Czech Geological Survey in Prague, and petrography examined in detail using Nikon Eclipse LV100N microscope with installed digital camera at the Institute of Petrology and Structural Geology at Charles University. The microanalyses of the rock-forming minerals were obtained by a JEOL JXA-8530F field-emission gun electron probe micro-analyzer (FEG-EPMA) equipped with wavelength and energy dispersive spectrometers (WDS and EDS), at the Institute of Petrology and Structural Geology at Charles University. For purpose of analysis, the samples of polished thin-sections with carbon-coating were analyzed by accelerating voltage of 15 kV, and beam current of 15 nA. The elements were measured on WDS crystals standards: F-topaz, Na-albite, Al-corundum, Si-quartz, P-apatite, Cl-tugtupite, K-sanidine, Ca-diopside, Ti-rutile, Cr-Cr2O3, Mn-rhodonite, Fe-magnetite, Zn-sphalerite, Ba-baryte. For feldspars and large grains, a beam of 5 µm in diameter was used, for smaller grains, the beam was 1 to 2 µm in diameter.

Morphotectonic Analysis (Digital Elevation Model)

The morphotectonic analysis was used in order to indicate large tectonic structures, using SRTM 1 Arc-Second Global shaded relief images (https://earthexplorer.usgs.gov/) and ArcGIS, ArcMap 10.6.1. software (https://www.esri.com/). The principal procedure for this analysis

follows Dhont and Chorowicz (2006). In this method, large lineament, which are marked by sharp contact, are interpreted as neotectonic fault structures. The shaded relief images were illuminated in N, NW, and NE direction, which highlighted visualization of the lineaments. The interpreted tectonic structures were compared with geological maps (Annex-1, Annex-2). In addition, the Google Earth Pro software was used to eliminate anthropogenic linear elements. The lineament interpretation was done on a scale of 1: 100, 000. The data of faults strike were obtained in ArcMap and analyzed using SpheriStat 3 software. The DEM for EARS was done using Global 30 Arc-Second Elevation (GTOPO30), the tectonic lineaments were interpreted in scale of 1: 500,000.

Paleostress Analysis

The paleostress analysis was performed on ROCK 2019 software using methods of Málek et al., (1991) in cooperation with Mr. Jiří Málek. This method is iterative inverse method, based on the total inversion method of (Angelier et al., 1982). This method compares the observed shear stress with the calculated ones, which corresponds to theoretical stresses. The ROCK 2019 software uses the distribution of shear stress direction within the fault planes of different orientations reactivated by a single stress tensor. The data are automatically divided into separated homogenous subsets, which records different stress phases. This division is part of the optimization process, where the parameters are calculated simultaneously (Angelier et al., 1982, Angelier 1994, Coubal et al., 2015, Málek et al., 1991). The input data for paleostress calculation are fault plane parameters i.e., orientation of fault plane and slickenside orientations (Málek et al. 1991). This software allows to consider intensity of the preservation of linear features and also the probability of fracture reactivation, which is often proportional to the ratio of shear. The output data consists of 4 parameters describing the stress tensor, 3 angles determining direction of stress axes, and ϕ parameter characterizing shape of stress ellipsoid.

Gravimetry and Linsser Indications Calculation

The geophysical investigation (gravimetry) was used to improve the interpretation of tectonic lineaments and contacts of distinct lithologies within the study area. The gravity data (complete Bouguer anomalies-CBA) were collected in archives of the Geological Survey of Ethiopia and obtained from the project 682400. The individual gravity points were recalculated to a regular grid (200 x 200 m) using the krigging method and are presented in a form of contour lines (Figure 6-7) using the SURFER software (Golden Software Inc.). The data were further processed with assistance of Mgr. Jan Valenta, Ph.D. by calculation of Linsser indications by method of Šefara (1973), which is based on the method of Linsser (1967). The analysis was severely limited by a low data density within the study area (Figure 6-7).

Geochemistry

For geochemistry investigation, 13 samples were analyzed. Whole-rock geochemical data are presented in annexes (see Tab. 1, 2 ,6). The samples ca. (3-5 kg) were collected during geological mapping. After cleaning procedure and removal of weathered parts, the samples were crushed in the laboratories of the Geological Survey of Ethiopia in Addis Ababa and the Czech Geological Survey Brno to grain fraction (2- 3) cm by steel jaw crusher and homogenized. The jaw crushers were blown by an air compressor and wash out after each sample crushing to avoid possible contamination. Finally, aliquots of ca. 200 g were grinded in mill by agate planetary balls. Whole-rock analyses were provided by the Bureau Veritas Commodities Canada Ltd. (Acme Analytical Laboratories), Canada by ICP-OES following a lithium metaborate or tetraborate fusion and dilute nitric digestion of a 0.2 g sample. The REE and refractory metals were determined by ICP-MS following a lithium metaborate or tetraborate fusion and nitric acid digestion of a 0.2 g sample. In addition, separate 0.5 g splits were dissolved in aqua regia and analyzed by ICP-MS. The calculations and plotting of whole-rock geochemical data was performed on R software using statistical package GCD kit (Janoušek et al., 2006).

4. Lithology and Petrology

From the geological point of view, the study area includes the structure of the Main Ethiopian Rift (boundary between Central and Southern segment) and volcanic highland plateau, Ethiopian Plateau on the west and Somalian Plateau on the east, which are set on metamorphic basement rocks (for location see Figure 1-1). The Southern segment of the Main Ethiopian Rift (SMER) is associated with both Ethiopian and Kenyan rifts (Ebinger et al., 2000; Philippon et al., 2014). This area is in comparison with other parts of the Main Ethiopian Rift or whole East African Rift System, relatively poorly documented. Even though, the SMER is important in terms of understanding of MER evolution, the data remains relatively sparse. Another motivation for focusing on this area is rapid increasing of the population, within Sidama, Gamo Gofa, and Wolayita Zone, more than 10 million people live, therefore it represents an important area for geological investigation. Despite this fact, several papers focusing on geochemistry (George and Rogers, 2002; Shinjo et al., 2011; Stewart and Rogers, 1996; WoldeGabriel et al., 1991) and tectonics (Ebinger et al., 2000, 1993b; Emishaw et al., 2017; Philippon et al., 2014; WoldeGabriel and Aronson, 1987) were published.

The area of interest comprises lithologies of metamorphic basement rocks of Proterozoic ages, overlying by pre-rift volcanic rock from Eocene to Oligocene, and syn-rift volcanic rocks from Miocene up to Holocene. The volcanic highland plateaus, bordering the MER valley, are made of several succession of volcanic eruptions. The rift valley is composed chiefly of pre-rift and syn-rift volcanic products. Both plateaus and rift valley are set on Pre-Cambrian metamorphic basement rocks. The youngest succession is presented by various type of sediments, filling the rift valley.

Geological maps description

Compiled geological map of northern Sidama Region and easternmost flank of Wolayta Zone (Annex-1) encompasses the rift floor valley and eastern plateau. The rift floor valley is filled with thick sequences of various volcanic rocks (rhyolite to trachyte, basalt to trachybasalt lava flows, redeposited sediments, and volcaniclastic material, reaching thickness up to 1700 m (see Annex-3). The individual lithologies have primary flat-lying contacts, often modified by normal, rift-related faults. The rift floor valley of mapped area contains several caldera complexes (Diguna Fango, Cherica, Kilisa, Geremba, and part of Hawasa Caldera (integral part of Corbetti Caldera Complex), constituted of succession of prevailing rhyolite to trachyte lava flows, alternated with ignimbrites and pyroclastic deposits covering ca. 50% of mapped area (see legend items 18, 13, 11, 10). The eastern plateau is built by metamorphic basement rock assemblage cropping out mainly in the southeastern tip of the map (Annex-1; see legend items 30, 29, 28, 27), overlayed by pre-rift volcanic rocks of Eocene to Oligocene age, constituted by basalt to trachybasalt lava (legend item 26), reaching up to 1700 m in thickness (see Annex-3), with interbedded layers of rhyolitic ignimbrite (legend item 25) having thickness up to 300

m in total. This succession is overlaid by younger up to ca. 1000 m thick sequence of trachyte to trachybasalt lava flows (24) with alternation of numerous pyroclastic strata of Oligocene age.

The geological map of northern Gamo Zone (Annex-2) encompasses eastern margin of the rift floor valley and western plateau. The rift floor valley is filled by ca. 1000 m thick sequences of rhyolite ignimbrite and related pyroclastic fall deposits belonging to the Hawasa Caldera (see legend item 3), isolated rhyolite lava domes and subordinate alkaline basalt lava flows partly covered by Quaternary sediments (see legend items 1, 2). The pre-rift volcanic and pyroclastic rocks of Eocene to Oligocene age (called as Amaro-Gamo Basalts) crops out on the western plateau, constituted mainly by basalt to trachybasalt lava interbedded by layers of rhyolitic ignimbrite (Shole Ignimbrite) and basic fall-deposits (see legend item 4, 5, 6). The overall thickness of these sequence exceeded 1700 meters.

The overall geological pattern of the mapped areas (Annex-1, Annex-2) is strongly modified by normal, rift-related faulting.

4.1. Basement Rocks

The basement rocks of study area comprises of low to high grade metamorphic rocks belonging to Adola-Moyale Belt, part of Southern Ethiopian Shield of Proterozoic age (Stern et al., 2012; Verner et al., 2021; Worku and Schandelmeier, 1996). The Adola-Moyale Belt is here represented by various metamorphic rocks and by the syn- to post-collisional granitoids in the lowermost part (Worku and Schandelmeier, 1996; Verner et al., 2021). The basement rocks are exposed chiefly in deeply eroded river valleys (see Annex-1). The Southern Ethiopian Shield is made of medium to high-grade volcano sedimentary rock assemblage; amphibolites, paragneisses, migmatites, mica-schists and orthogneisses, which are intruded by small granitic plutons.

Igneous and metamorphic rocks assemblage (only in geological cross-section)

The crystalline basement rock, covered by Cenozoic volcanic sequences, consists of granitoids and metamorphic rocks of Proterozoic-Cambrian ages. Neoproterozoic to Cambrian granitoids are represented by granodiorite to granite, locally with bodies of diorites to gabbro. The metamorphic rocks are represented by greenschist-facies to upper amphibolite facies rocks (Abdelsalam and Stern, 1996; Verner et al., 2021; Worku and Schandelmeier, 1996).

Biotite to amphibole-biotite orthogneiss

Biotite to amphibole-biotite orthogneiss is exposed on the easternmost part of Sidama and crops out along rivers. The gneisses are medium grained of light gray color, composed mainly

of quartz, feldspars, biotite, and contain quartz dikes (Fig. 4-2). These gneisses are strongly foliated, orthogonal joint system (Fig. 4-1) is well developed with variable spacing ranging from ~10 cm to 1m. The metamorphic foliation is defined by the strong preferred orientation of the biotite grains and incline gently in SE direction.

Figure 4-1. Orthogonal joint system in orthogneiss, (Lodoma river, NG030).

Figure 4-2. On the left strongly foliates orthogneiss (Lodoma river, NG030); on the right extremely weathered gneiss with preserved quartz dikes (Antsokia, BZ176).

Biotite to muscovite-biotite paragneiss

Biotite to muscovite-biotite paragneiss is mainly exposed below the southwestern part of Sidama Zone, in the vicinity of the Genale River. Paragneisses are in contact with granitic intrusions and amphibolite. These weathered, locally extremely weathered paragneisses are medium- to fine-grained of light to dark gray color. These rocks are strongly foliated (Figure 4-3) and records multiple deformations. They consist of biotite (29-41 vol. %), plagioclase (25-

38 vol. %), K-feldspar (0-9 vol. %), muscovite (0-9 vol. %), and subordinate tourmaline and garnet (Verner and Megerssa eds., 2018).

Figure 4-3. Intensively deformed biotite paragneiss with pronounced metamorphic foliation (Qadela village, AM138).

Amphibolites

Amphibolites are medium to fine grained with gray to dark gray color, exposed in Genale River valley (Figure 4-4). Amphibolite makes several mm to cm wide alternating bands of leucocratic layers and dark gray melanocratic layers. These rocks are slightly weathered, several meter large blocks are exposed along the streams and river. Amphibolite is composed of amphiboles (46-80 mod. %), plagioclase (12-43 mod. %), epidote-clinozoisite (up to 9 mod. %), quartz (up to 6 mod. %), biotite (up to 5 mod. %), garnet (up to 5 mod. %). Accessory minerals are presented by magnetite and/or ilmenite. The leucocratic bands are dominated by plagioclase, minority by quartz, the melanocratic bands are dominated by chiefly by amphiboles and biotite (Verner and Megerssa eds. 2018).

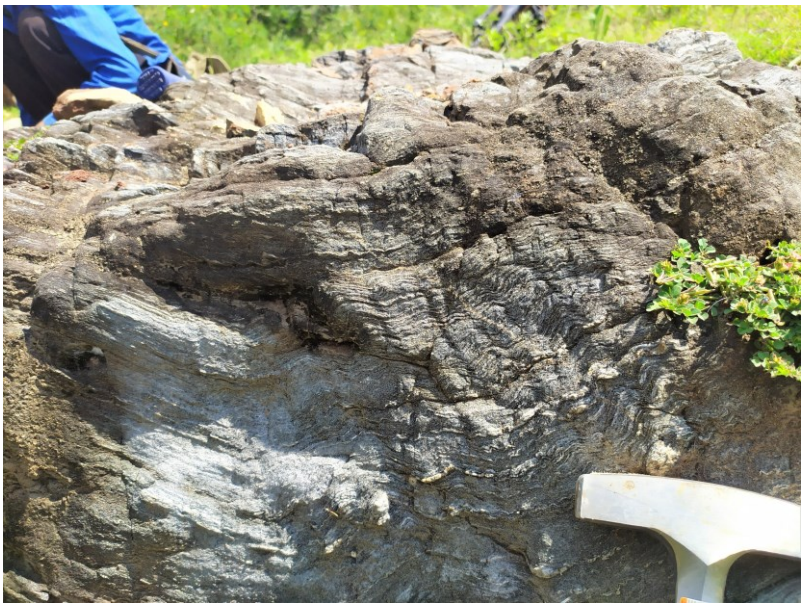

Figure 4-4. Folded amphibolite (Genale river, BZ174).

4.2. “Pre-rift” Volcanic Deposits

The metamorphic basement is unconformly overlined by pre-rift flood basalts, representing the initiation of volcanic activity in SMER and whole EARS, starting at ca 45 to 35 Ma. These transitional basalts, known as Amaro-Gamo Basalts, are overlying the red sandstones in Amaro region (Ebinger et al., 1993b; George and Rogers, 2002). This sequence progressively thickens northwards and it can rich up to 1700 m in thickness (Levitte et al., 1974). This unit makes a massive lava flows with weathered surface, subordinately pyroclastic deposits are presented.

These basalts are conformable overlie by Amaro Tuff, represented by welded rhyolitic ignimbrites, known as Shole Ignimbrites, yielding ages around 36.9 Ma and with pyroclastic deposits (Ebinger et al., 1993 and references therein). The total thickness of these ignimbrites together with subordinate rhyolite lava reaches up to 300 m, but seldom reaching thickness more than 100 m (Levitte et al., 1974). The Amaro-Gamo unit is accompanied by strongly weathered trachytes and trachybasalts of Oligocene age, forming lava flows and volcanic necks. The source for Amaro-Gamo unit is linked with the mantle plume (Ebinger and Sleep, 1998; George and Rogers, 2002; Stewart and Rogers, 1996).

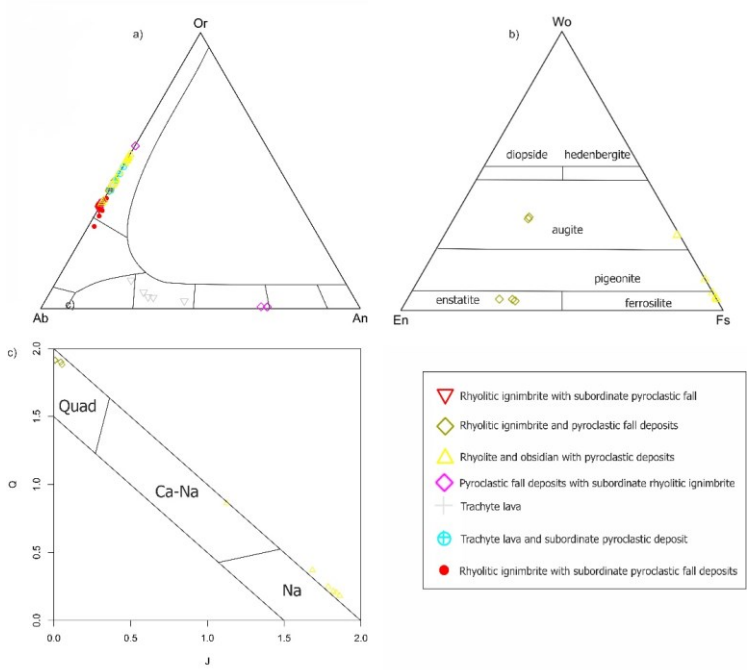

Figure 4-5. Classification diagrams; (a) Ab-An-Or feldspars; (b, c) En-Wo-Fs and J-Q pyroxene classification diagram modified after Morimoto et al. (1988).

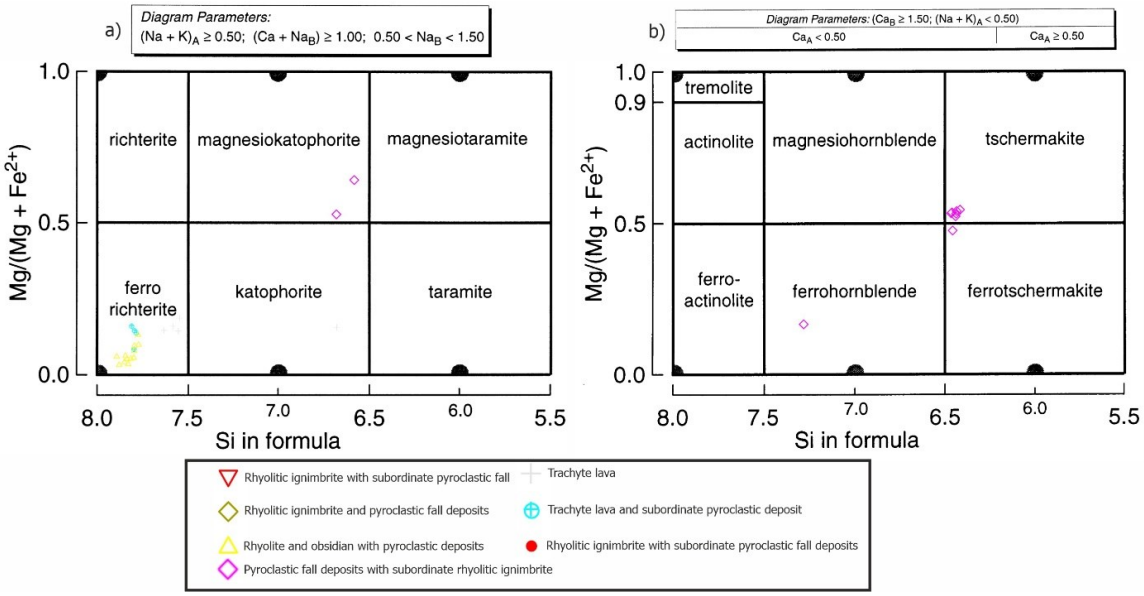

Figure 4-6. Amphibole classification diagrams; (a) for Na-Ca amphiboles; (b) for Ca amphiboles, after (Leake et al., 1997).

Eocene-Oligocene

Basalt to trachybasalt lava with subordinate basaltic pyroclastic deposits

Basalt to trachybasalt lava with subordinate basaltic pyroclastic deposits are the oldest rift-related volcanic units. This unit is largely exposed in Sidama Region, especially in its eastern part in the eastern volcanic highland, reaching total thickness about 1500 m, from Bululta,

Mejo, Daye and continuing northwards, and in the northern part of Gamo Zone (Fig. 4-7). This unit also occurrence in vicinity of rift valley close to Teferi Kela. These volcanic and volcanoclastic rocks are referred as Amaro-Gamo Basalts (Stewart and Rogers, 1996). The basalt consists of plagioclase (up to 60 vol. %) and clinopyroxene (up to 50 vol. %). The olivine and interstitial glass are presented in subordinate amount, ilmenite and magnetite are presented as accessory. The glass is partially decomposed into clay minerals and chlorite. Basalts to trachybasalts are characterized by a hyalo-ophitic to ophitic texture in their groundmass with flow structure of plagioclase and pyroxene (Figure 4-8). These rocks make up to several meter thick massive lava flows of dark gray to black color, with slightly to strongly weathered surfaces in the field, frequently are affected by faulting and columnar jointing with spacing up to 2 m. These lava flows are locally intercalated with the paleosoils.

Figure 4-7. View on pre-rift basalts traps forming highlands of northern part of Gamo Zone.

Figure 4-8. On the left basalts to trachybasalts in open quarry (BZ184); on the right microphotograph of basalt to trachybasalt under cross polarized light (AM032).

Rhyolitic ignimbrite with subordinate rhyolite lava

Rhyolitic ignimbrite with subordinate rhyolite lava is extensively exposed within rift floor valley in north to south direction from Bokaso to Kebado towns, reaching total thickness of 50 to 300 m. Further, they are encompassed within Amaro-Gamo Basalts. The ignimbrites make relatively thin intercalates south from Selam Ber and west of Gocho. These ignimbrites contain layers of subordinate acid lavas with ashfall deposits. The ignimbrites are fine- to medium grained of various color, light gray, orange, reddish to yellowish color, and are affected by columnar jointing and intense welding (Figure 4-9). Welding of ignimbrite is well noticeable, flattened parts of pumice and glass make up to 5 cm large fiamme, creating eutaxitic texture. The matrix is fine-grained containing a glass fragments up to 1 mm large. Ignimbrites comprise euhedral to subhedral crystal fragments (5-40 %) of sanidine, quartz, and plagioclase up to 2 cm large in diameter (Hroch et al. 2018).

Figure 4-9. Rhyolitic ignimbrite west of Arbe Gona (AM009).

Oligocene

Trachyte to trachybasalt

Trachyte to trachybasalt is exposed in the eastern volcanic highland of Sidama, in southern Sidama within rift valley, and in northwest part of Gamo Zone. This unit is encompassed in large basalts to trachybasalt lava unit of Amaro-Gamo Basalts and probably represent younger pre-rift volcanism phase. These trachytes to trachybasalts form strongly weathered lava flows and volcanic neck. They are light gray fine-grained to porphyritic rocks with trachytic texture (Figure 4-10). Trachyte and trachyandesite are dominated by subhedral to euhedral sanidine to anorthoclase ($Ab_{56-68}An_{0-1}Or_{29-43}$) laths (Fig. 4.4a) (55–75 vol. %) with preferred orientation, and by clinopyroxene. Locally, amphibolite of fluoro-richterite and Mg-Fe-Mn grunerite composition are presented (Tab. 5). Accessory minerals include magnetite and ilmenite.

During weathering, the trachytes change their color to dark gray and feldspars are decomposed into clay minerals.

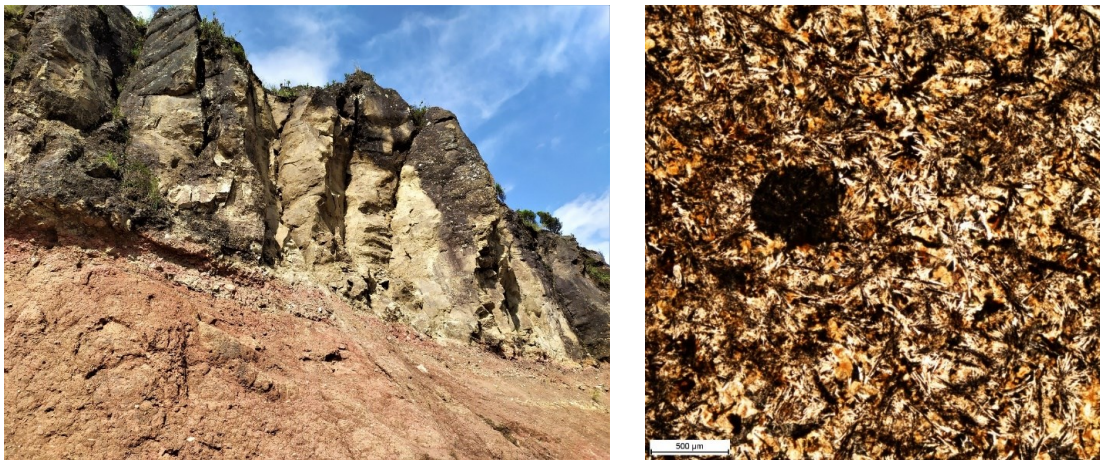

Figure 4-10. On the left trachyte to trachybasalt (Bunake river, BZ152); on the right microphotograph of trachytic texture of trachyte to trachybasalt (Shiko, BZ126).

4.3. "Early" Volcanic Deposits

Miocene

Rhyolite lava with subordinate volcanic breccia and ignimbrite

This unit form small lava flows and lava domes, and volcanic necks, locally interbedded by up to 2 m thick ignimbrite layers (mainly in the area between Dila, Abera, and Kebado). These fine-grained flow-banded porphyritic rhyolites are light gray to red. They contain phenocrysts of quartz, anorthoclase, rarely also clinopyroxene, groundmass is fairly equigranular, sometimes trachytic and consists of quartz, anorthoclase, rare albite, and volcanic glass in various stages of alteration. The interbedded ignimbrites are dark-gray with glassy, vitro-porphyritic texture.

Pliocene

Welded rhyolitic ignimbrite

Welded rhyolitic ignimbrite are exposed south-eastern from Hagere Selam along streams valley and locally around Kebado. These ignimbrites crop-out in various color, due to weathering, pink, orange to dark gray, fresh samples are white to bluish gray (Figure 4-11). Locally are affected by columnar jointing. The ignimbrites contain fiamme, from several mm

up to 3 cm large, with varying amount of lithic fragment, feldspar, and quartz. These ignimbrites were dated by Woldegabriel et al (1990) and yield ages of 2.49 ± 0.1 Ma.

Figure 4-11. Welded rhyolitic ignimbrite (Malgano Kolisho, BZ087).

Basaltic lava and basaltic pyroclastic deposits

Basaltic lava and basaltic pyroclastic deposits are exposed especially in southern part of Sidama, in vicinity of Hagere Selam, Tula, and Abera, and south to southern-eastern direction from Bokaso town. These basalt form dark gray massive lava flows, with columnar joints, during weathering, they exhibit reddish crust (Figure 4-12).

Figure 4-12. Basalt lava (Tula, TD021).

4.4. “Late rift” Volcanic Deposits

Above mentioned volcanic events were followed by a dramatic decrease in volcanic activity. This period of quiescence lasted for ~10 to 11 Ma (Bonini et al., 2005; Ebinger et al., 2000, 1993b). The volcanic activity within this period is presented only by small eruptions of peralkaline pantelleritic ignimbrites intercalated with minor basaltic lava flows in the areas beyond the rift escarpments (Chenca escarpment) yielding ages of 7 Ma (Bonini et al., 2005). The volcanic activity was restored in Late Pliocene, continuing to Holocene. The volcanism is mostly bi-modal (Bonini et al., 2005; Rooney, 2010; Woldegabriel et al., 1990). The Quaternary to recent volcanic activity is mainly focused in the rift valley (Philippon et al., 2014). The bimodal volcanism is represented by basalts, trachytes, rhyolites, rhyolitic ignimbrites, and varied pyroclastic deposits (Corti, 2009; Woldegabriel et al., 1990).

Lower Pleistocene

Rhyolitic ignimbrite with subordinate pyroclastic fall deposits

Rhyolitic ignimbrites with subordinate pyroclastic fall deposits are extensively exposed in central (Bursa, Arbe Gona) and eastern part of Sidama (Daye), further extend around town Hoghiso, within rift floor and eastern plateau. These ignimbrites are medium grain-size of bluish gray to white color, with developed columnar joints (Figure 4-14). The thickness varies from less than 1 to 8 m. They contain oligoclase ($Ab_{61\text{-}63}$ An_0 $Or_{36\text{-}38}$) (Fig. 4-4a) phenocrysts, minority labradorite to bytownite feldspars**.** Accessory minerals include olivine magnetite, and ilmenite. These ignimbrites are commonly welded with varying amount of fiamme and feldspar crystals (Figure 4-13). The fiamme size extend from 1 mm up to 3 cm in length, feldspars are locally 1 mm large. Besides, they contain quartz, shards of flattened glass, displaying a well-developed parallel alignment, and structural remnants of the original pumices.

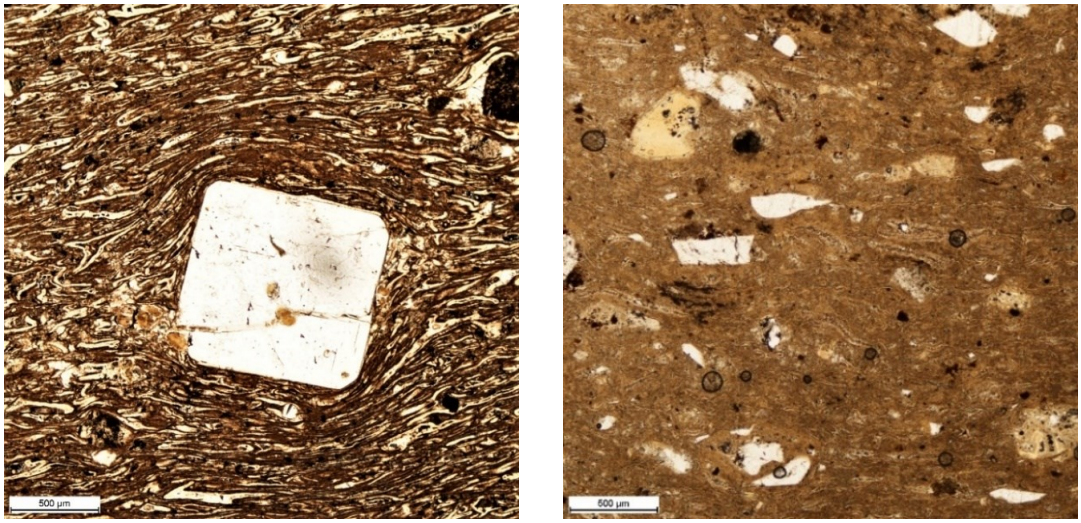

Figure 4-13. On the left microphotograph of sanidine in welded rhyolitic (AM027); on the right microphotograph of remnants of original pumices Arbe Gona (BZ132).

Figure 4-14. Rhyolitic ignimbrite (Genale river, BZ225).

Rhyolitic and trachytic ignimbrite

Rhyolitic and trachytic ignimbrites are exposed north and south from Dila and west from Kebado. These ignimbrites are fine-grained of gray to yellowish color (Figure 4-15), making up to 5 m thick layers of both welded and unwelded ignimbrites, and ash fall deposits. They contain feldspar phenocrysts, glass shards, fiamme up to 2 cm long, basaltic, and rhyolitic subangular to rounded fragments. These succession of rhyolitic and trachytic ignimbrites were dated by Buriánek ed. (2018) and yield ages of 1.21 ± 0.27 Ma. The ignimbrites are affected by jointing and display variation in the degree of welding.

Figure 4-15. Unwelded rhyolitic ignimbrite (south of Chuko, TD023).

Rhyolitic ignimbrite and pyroclastic fall deposits

Rhyolitic ignimbrite and pyroclastic fall deposits are extensively exposed within rift valley center (west part of Sidama) and north, northeast, and west part of Gamo Zone. The succession of welded to unwelded rhyolitic ignimbrites associated with minor pyroclastic fall deposits are linked with eruptions of Hawasa Caldera and its main stage of formation (Rapprich ed. 2013). These ignimbrite were dated by JICA (2012) and WoldeGabriel et. al (1990) on K-Ar method and yield ages of 1.1 to 1.85 Ma. The discrete flow units are separated by pumice fall deposits. The ignimbrites are medium grained of gray to white, up to yellowish color. The ignimbrites contain euhedral to feldspar (Ab_{53-57} An_0 Or_{43-47}) (Figure 4-5a) phenocrysts (up to 15%), oval shaped grains of quartz. The matrix contains welded glass-shards with small amphibolite crystals. Lithic fragments are visible with size varying from 1 to 3 cm, the pumice content reach up to 4 vol. %, further fragments of glass up to 1 cm large are presented (Figure 4-17). Accessory minerals include olivine and ilmenite**.** The highly weathered parts contain Mn carbonates identified as rhodochrosite, which makes spheroidal aggregates (Figure 4-16). The interbedded ash layers are characterized by lapilli of 0.1 to 0.5 cm in size.

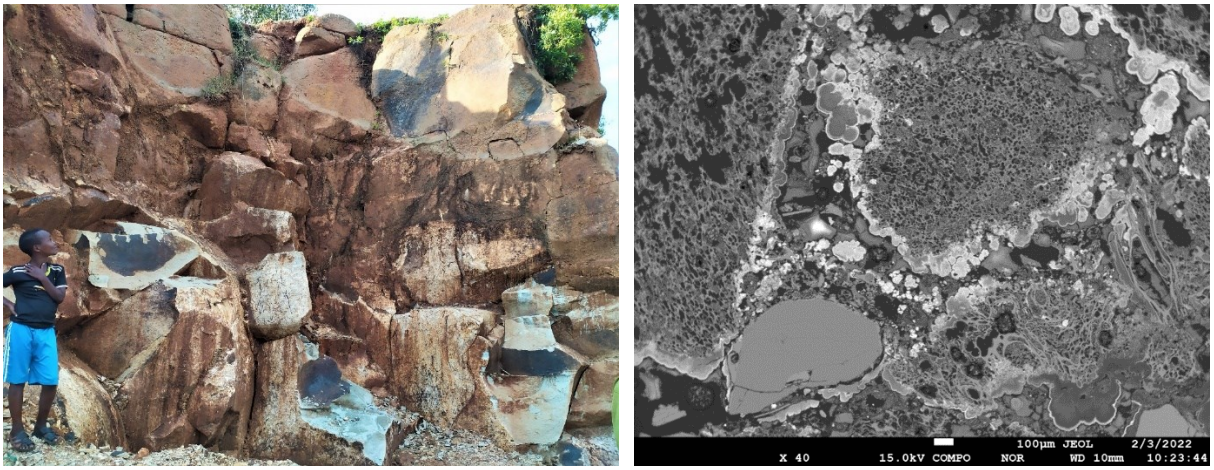

Figure 4-16. On the left welded rhyolitic ignimbrite in open quarry (Loka Abaya National Park, KE409); on the right microphotograph of rhodochrosite spheroid in rhyolitic ignimbrite in electron probe (DE037).

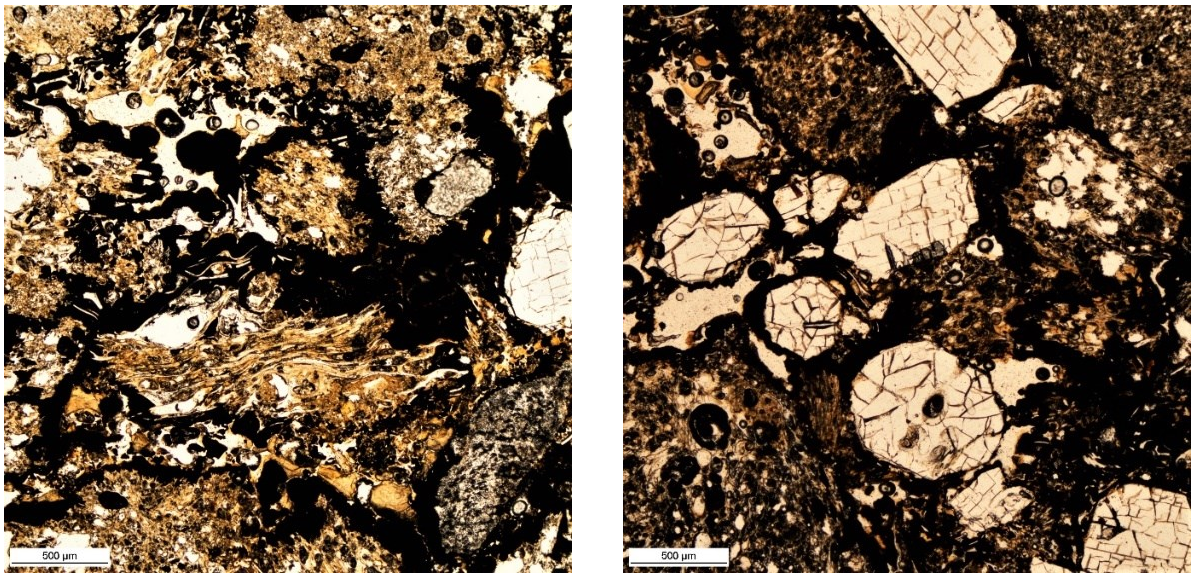

Figure 4-17. Microphotograph under plane polarized light of pyroclastic fall deposits (south of Yirba, DE037).

Alkali rhyolite lava and pumice fall deposits

The alkali rhyolite lava and pumice ash fall deposits are white to bluish-gray rocks exposed mainly in vicinity of the Hawasa Caldera (Wesha Soyama), further southeast from Yirba and northeast from Dila. They form a glassy brecciated rhyolite lava domes with columnar jointing (Figure 4-18). This unit has been dated by WoldeGabriel et al. (1990) using the K-Ar method and yield ages of 0.96 ± 0.1 Ma. Locally ignimbrites, tuff rich in lithic fragments are presented.

Figure. 4-18. Open quarry in alkali rhyolite (Boricha Dome, TE028).

Alkali basalt

Alkali basalts are mainly exposed in the area between Besa Ware, Daye and Arbe Gona. Further they crop out in area east from Tula, where they form elevations within rhyolitic

ignimbrites. The basalts are fine- to medium grained of gray color to brownish color, making massive lava flows with presented flow structures (Figure 4-20), occasionally having vesicular texture. Locally they are embedded with the fine basaltic scoria layers. The basalts are dominated by plagioclase of andesine to oligoclase phenocrysts (Ab_{53-66} An_{23-43} Or_{2-10}) (Figure 4-5a) reaching the content up to 60 vol. %, further by clinopyroxene (up to 50 vol. %). The orthopyroxene is presented by enstatite to pigeonite (XMg 0.8-1.2 and Ca 0.06 to 0.64 apfu) (Figure 4-6). The plagioclases and pyroxens form 1. to 2 mm euhedral crystals, with some upwards of 4 mm (Figure 4-19). Locally olivine is presented, the matrix contains glass fragments, pyroxene, plagioclase, and opaque minerals, locally euhedral crystal of apatite was identified. These basalts have been dated by Woldegabriel et al. (1990) yielding ages of 1.60 ± 0.1 Ma, using the K-Ar method.

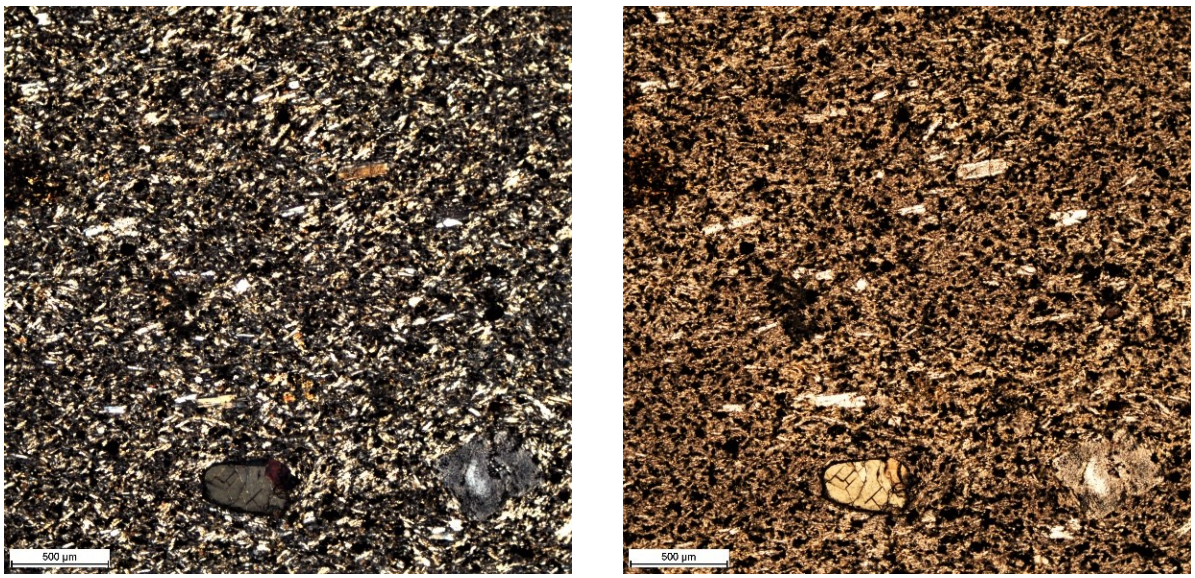

Figure 4-19. Microphotograph of alkaline basalt, on the left under cross polarized light, on the right under plane polarized light (west of Tula, NG037).

Figure 4-20. On the right, pahoehoe lava flow, on the right rheomorphic folds inside alkaline basalt (west of Tula, NG037).

Pleistocene

Obsidian and rhyolite to trachyte lava

Obsidian and rhyolite to trachyte lava is exposed within the Diguna (Duguma) Fango Caldera which produced large volumes of acidic lava flows and formed lava dome (Chernet, 2011; Corti et al., 2013). The rhyolite lava displays columnar jointing, locally rheomorphic folds are presented (Figure 4-21). The rhyolites display slightly welding and contains subhedral grains of feldspar ($Ab_{44-61}An_0Or_{38-55}$) (Figure 4-5a) reaching up to 2 mm in dimeter (Fig. 4-22), further euhedral to subhedral grains of ferrosilite orthopyroxene up to 1 mm in diameter. Subhedral grains of quartz and shards of glass is presented, which is partially decomposed. The matrix is composed of feldspars, pyroxene, and amphibolite. The volcanic glass encompasses amphibolite needles in range of 50 to 200 microns of ferro-richterite (Figure 4-6, 4-22). Euhedral grains of quartz and feldspars are presented together with subhedral grains of aenigmatite. The volcanic glass reveals flow texture by arrangement of amphibolite needles (Fig 4-22).

Figure 4-21. On the left rheomorphic fold in obsidian lava within rhyolite; on the right rhyolite lava with pyroclastic deposit on the top (open quarry in the Diguna Fango, SD006).

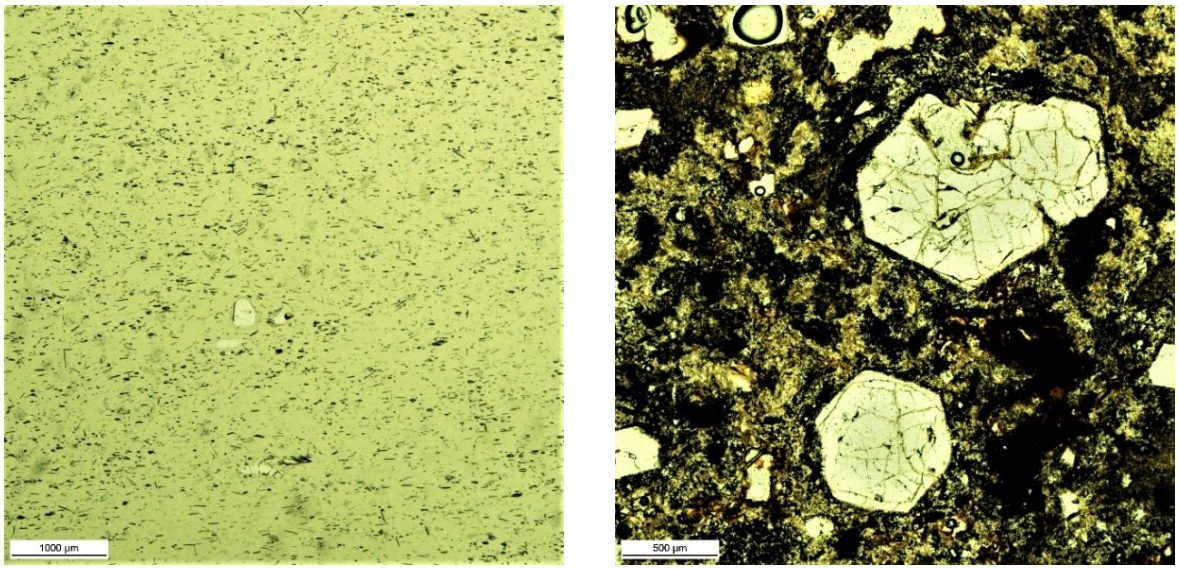

Figure 4-22. Microphotograph of obsidian lava, on the left under plane polarized light; on the right pyroclastic deposit under cross polarized light (Diguna Fango Volcano, DE522,522A).

Trachyte lava is mainly exposed on the northern edge and within Diguna Fango Caldera. The trachyte is porphyritic with trachytic texture (Figure 4-23), dominated by euhedral to subhedral phenocryst of feldspar (Ab_{53-56} An_0 Or_{44-47}) (Figure 4-5a) up to 3 mm in diameter. Further it contains euhedral grains of quartz, which are often cracked, fluoro-richterite (Figure 4-6). The groundmass is composed of feldspar, amphibole, and glass.

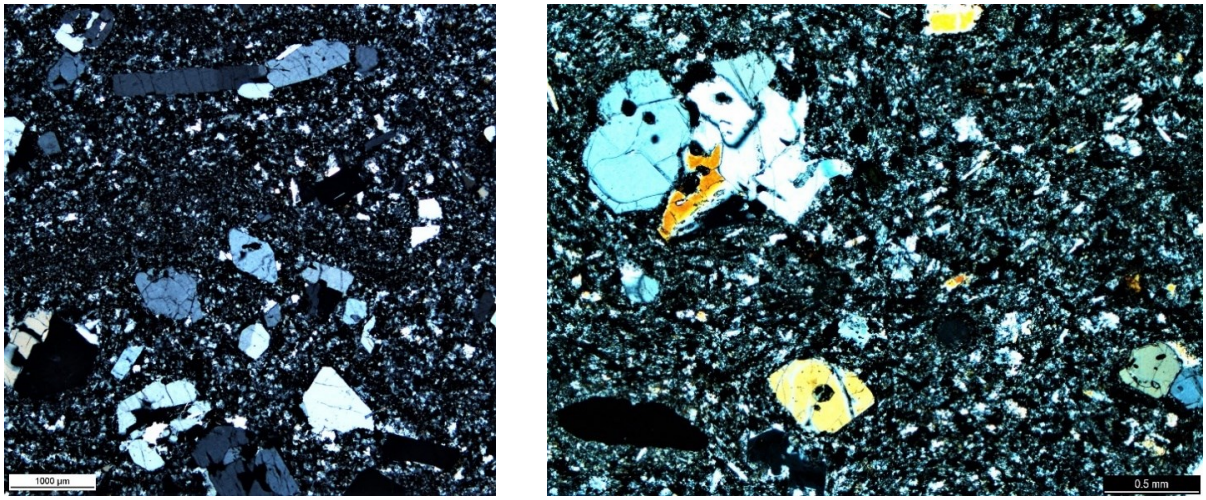

Figure 4-23. Microphotograph of trachytic lava under cross polarized light (edge of Diguna Fango Caldera, DE521).

There is no provided dating on Diguna Fango Caldera so far. The only dating has been reported by (EIGS-GEP, 1981), for Obitcha rhyolite flow situated ca 25 km southwest from Fango and they reported age of 1.57 Ma using K-Ar method. This age could be assumed for Diguna Fango Caldera. The Diguna Fango Caldera has more than 10 km in diameter and it lies along active volcano-tectonic axis of rift valley and is strongly affected by faulting (Chernet, 2011).

Pyroclastic fall deposits with subordinate ignimbrite

Pyroclastic fall deposits with subordinate ignimbrites are situated southwest of Diguna Fango Caldera. The pyroclastic fall deposit consists of euhedral to subhedral grains of feldspar (Ab_{48-53} An_0 Or_{47-52}) (Figure 4-5a, 4-23) up to 1 mm large, furthert ferro-richterite (Figure 4-5a) and aenigmatite. Oval to subhedral grains of quartz are presented together with shards of glass. The groundmass is dominaned by glass, small grains of amphiole and feldspars, and by accesory minerals probably magnetite. The pyroclastic fall depostit contain partiali alterated lithic fragments of fiamme pumice up to 2 mm in diameter, which are randomily oriented within pyroclastic deposit (Figure 4-24).

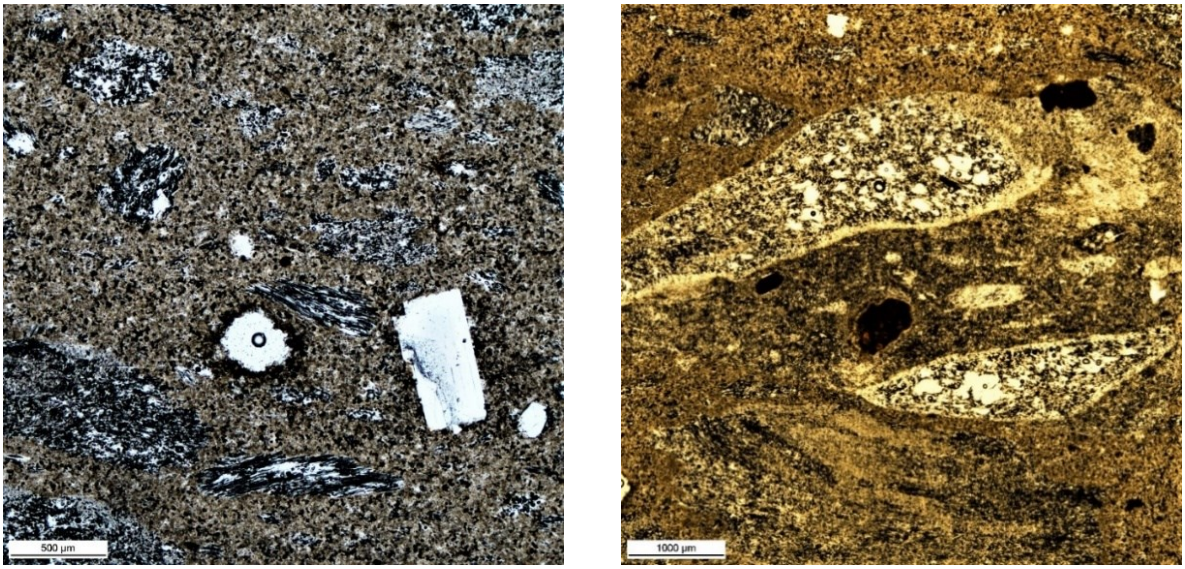

Figure 4-24. Pyroclastic fall deposit above trachyte lava (northeast part of Diguna Fango Caldera, DE523A).

Welded to unwelded rhyolitic ignimbrite with subordinate pyroclastic deposits

The welded to unwelded rhyolitic ignimbrite are commonly highly weathered with color varying from bluish gray to yellowish (Figure 4-25). This unit is associated with the Corbetti Caldera (Rapprich eds., 2013). The amount of welding decreases with increasing distance from caldera. The ignimbrites had been dated using K-Ar method and yield ages of 0.19 Ma (JICA, 2012). These ignimbrites crop-out extensively southeast from Hawasa caldera. The subordinate pyroclastic deposits commonly contain lapilli with size of the order of centimeters, lithic fragments and fiamme, total thickness reach more than 100 m. The individual ignimbrite units are separated by pumice fall deposits.

Figure 4-25. Welded rhyolitic ignimbrite cover by pyroclastic fall deposits with visible lapilli (west of Tula, BZ228).

Rhyolite to trachyte lava

Rhyolite to trachyte lava is exposed northwest form Dila in small form of volcanic plate. These rocks are fine-grained to porphyritic of light to dark gray color. They contain sanidine phenocrysts in a partly devitrified groundmass.

Pumice and ashfall deposits

Pumice and ashfall deposit are associated with Plinian to phreatomagmatic eruptions of the Hawasa Caldera and croup-out in its vicinity (Rapprich eds., 2013). This succession is dominated by matrix-supported yellowish to brownish ash fall deposits with small clasts of pumice or vitreous rhyolite lithic fragments. Well-sorted massive ash layers are rich in accretionary lapilli and clast-supported pumice-rich layer. The pumice size reaches up to 30 cm in diameter (Figure 4-26, 4-27). Total thickness of pumice and ash fall reaches up to 10 m. Locally, they are presented with paleo-soil horizons of thickness up to 30 cm, (Figure 4-27).

Figure 4-26. Cave inside of pumice and ashfall (west of Kocho, BZ239).

Figure 4-27. On the left, contact of pumice and ash fall with paleo-soil (Hoghiso, BZ238); on the right close-up look on pumice fragment (Kocho, BZ239).

Pyroclastic fall deposits with subordinate rhyolitic ignimbrite

Pyroclastic fall deposits with subordinate rhyolitic ignimbrite represent the last stage of Hawasa Caldera eruptions. This succession is largely exposed as the erosional relics south to southwest of Hawasa Caldera. The white to reddish ignimbrites (Figure 4-28) comprise of both welded and unwelded succession, they consist of discreate flow units, each separated by pumice ash fall deposits. The ignimbrites consist of slightly resorbed phenocrysts of plagioclase, bytownite to labradorite (Ab_{28-31} An_{68-71} Or_{0-1}) and alkali feldspar (Ab_{40-62} An_0 Or_{39-59}) (Figure 4-5a), further crystals of quartz, glass shards, and amphiboles of tschermarkite and barroisite composition (Figure 4-6). Partially decomposed accretionary lapilli were observed (Figure 4-29). The ignimbrite has been dated using the K-Ar method and yield ages of 0.46 ± 0.05 Ma (Hroch et al. 2018). The latest eruption commenced around 396 BC (Rapprich et al., 2016).

Figure 4-28. Pyroclastic fall deposits with subordinate ignimbrite (Bonkicha, AM066).

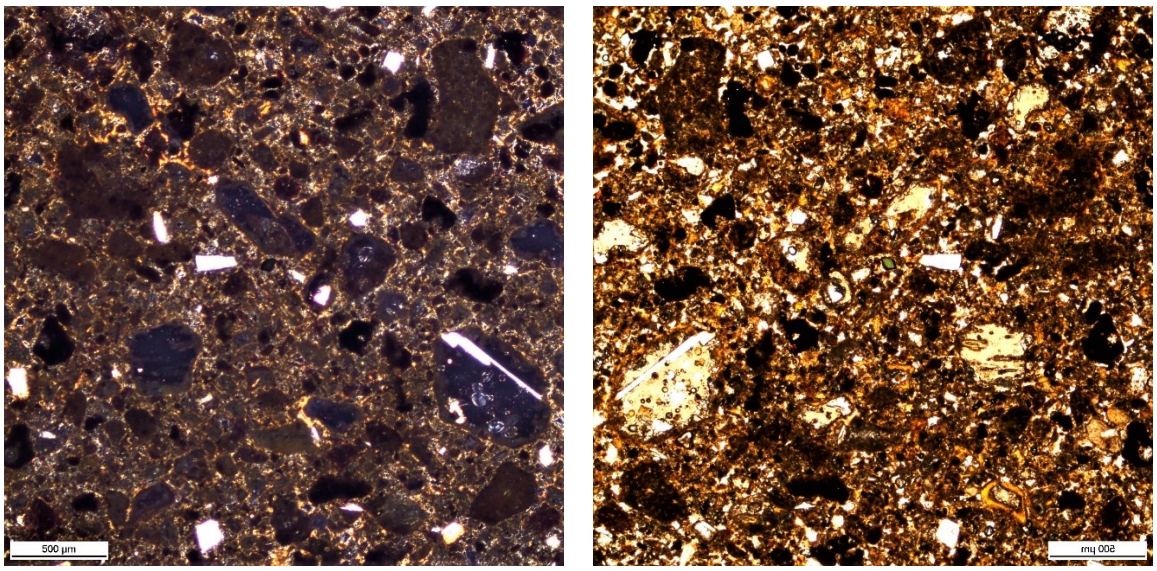

Figure 4-29. Microphotograph of pyroclastic fall deposits; on the left under cross polarized light; on the right under plane polarized light (Bonkicha, AM066).

Obsidian and rhyolite lava

Obsidian and rhyolite lava forms a small lava flow and dome mainly occur and are genetically related to Chabi Volcano and Hawasa Caldera (Rapprich eds., 2013). Further, they are exposed west of Arbe Gona Town. The obsidian lava overlays pumice deposits and locally is covered by the young pumice fall deposit. This unit was dated by Woldegabriel et al. (1991) by 40Ar/39Ar method and yielded an age of 0.02 ± 0.01 Ma, for more recent obsidian Chabbi Volcano, whereas K-Ar age obsidian from Hawasa Caldera is 1.02 ± 0.14 Ma (Žáček eds., 2014).

Pleistocene

Pumice fall and flow deposits with subordinate polygenetic sediments

Pumice fall and flow deposits with subordinate polygenetic sediments occurs around centre of Diguna (Duguma) Fango Caldera and Chiracha volcano. This unit consist of the pumice-rich layers (thickness up to 10 m) and alternated with ash fall deposits with normal gradation up to 2 m thick and ash-lapilli deposits. The pumice fall deposits are strongly weathered and change their color from gray to yellowish white, the layers are stratified with gentle dip and contain lapilli and pumice up to 5 cm large in diameter. Locally its intercalated with lacustrine sediments. Fall deposits are moderately sorted, containing angular to sub-rounded tephra (Figure 4-28).

Figure 4-30. Pumice fall and flow deposits (Diguna Fango, SD005).

Obsidian and rhyolite lava

Obsidian and rhyolite lavas are focused within center of the rift valley, around Mount Kilisa, Chiracha volcano north and west of Lake Abaya, locally crop-out around town Hoghiso. These young lavas are linked with Wonji Fault Belt (Boccaletti et al., 1998). Obsidian forms fresh black colored flows within older pumice fall and pyroclastic deposits with subordinate polygenetic sediments (Figure 4-31).

Figure 4-31. Obsidian lava in pyroclastic fall deposits (north of Lake Abaya, SD002).

Alkaline basalt lava and basaltic pyroclastic deposits

Alkaline basalts and basaltic pyroclastic deposits are situated in centre of rift valley, cropping-out in southwest Sidama around Chirecha caldera and within central part of the Hawasa Caldera. This unit form small scoria cones (Figure 4-33) and lava flows. This unit forms fissure vesicular basalts of dark gray colour near Chirecha volcano (Figure 4-32). The associated pyroclastic deposits consist of lapilli-stone and form small volcanic cones of massive texture and are poorly sorted clasts.

Figure 4-32. On the left rheomorphic fold in alkaline basalt; on the right vesicular basalt (Cherica volcano, BZ297).

Figure 4-33. Basaltic scoria cones close to Cherica volcano.

Pleistocene-Holocene

Colluvial sediments

Colluvial sediments represent accumulations from instabilities on slopes such as rockfalls, landslides, and creeping. They consist of re-sedimented sandy to loam soils with fragments of weathered rocks of various sizes ranging from cm to m scale (Figure 4-34). Colluvial sediments developed usually in foothills on steep slopes. The most extensive accumulations of colluvial sediments are on foothill of the Hawasa caldera rim. Further around large rivers like Genale, and around Hantate town. In the eastern part, these sediments are mostly associated with deep-seated landslides forming extensive accumulations of clay-supported matrix of highly weathered volcanic rocks with several meters' large blocks (Figure 4-34). In the western part of map area, colluvial sediments are predominantly sandy character associated with occurrences at the foothills of fault scarps (Figure 4-34) as this area is build up by weakly consolidated or unconsolidated volcanoclastic ignimbrites and basalts.

Figure 4-34. On the left, sandy colluvial sediments (Beke, SD024); on the right colluvial sediments with boulders of orthogneiss (Michicha, BZ175).

Polygenetic sediments

The polygenetic sediments represent succession of redeposited volcanoclastic material of alluvial and lacustrine sediments with vertical and lateral transitions between individual facies. These sediments are exclusively located in vicinity of the Hawasa Caldera (Figure 4-35). The alluvial deposits consist of sandy clays, and sands with lenses of fine-grained gravels. The lacustrine sediments are composed of silt and fine-grained sand, locally with clasts of pumice. The polygenetic sediments contain numerous pumice clasts and fragments of weathered ignimbrites and tuffs and locally obsidian up to 2 cm of diameter (Rapprich eds., 2013).

Figure 4-35. Polygenetic sediment on the cost of Hawasa Lake.

Lacustrine sediments

As the lacustrine sediments represents former lake bottom, they are concentrated in tectonically predisposed depressions, in study area especially in the vicinity of Lake Abaya and Hawasa Lake. They form unconsolidated fine-grained sediments of grayish to yellowish color, composed of clay, silts and sand.

Alluvial fan deposits

Alluvial fans originate from the erosion of material accumulated on slopes. The erosion and transport of the material is related to seasonal rainfalls. The alluvial fans are located in the mouths of streams and in the foothills of scarps. These accumulations are generally formed by clayey, silty, and sandy redeposited soils, sand, and gravel layers. System of alluvial fans forms a continuous rim at the foothills of the eastern caldera slope of the Hawasa Caldera, where these accumulations alternate to the colluvial accumulations of frequent slope instabilities, and on the northern flank of Lake Abaya, where predominantly sandy accumulations of re-sedimented pyroclastic and un-welded ignimbrites are formed. The estimated thickness is several meters with the maximal in the proximal part of fans.

Fluvial sediments

The youngest succession within study area is represented by fluvial sediments. These sediments are poorly developed, situated along streams and river in Sidama Region and Gamo Zone. The fluvial sediments are most developed within the Bilate river on the western border of Sidama Region and the Genale river on the eastern part of Sidama Region. These sediments are coarse-grained clast-supported gravels and coarse-grained sands, accompanied by several meter large boulders, with estimated thickness in the range of the first's meters (Figure 4-36). They are formed by fine-grained loam soils and silt rich in organic matter. In more active channels, these sediments are rather sandy. Locally in flat areas along stream, the wetlands with fine grained sediments with a high portion of organic matter cover parts of the floodplains (Figure 4-37).

Figure 4-36. Gravel lateral bar of intermittent river (Chiracha, BZ296).

Figure 4-37. Floodplain of Gamo Zone.

Regolith

Volcanic rocks, especially unconsolidated ones, are exposure to intensive chemical weathering. Due to tropical climate, rock surface suffers from chemical changes disintegration, and become prone to water erosion. The weathering product differs from the protolithe, in case of basaltic volcanic product, their color change to reddish, yellowish, and brownish silty to clayey loams with high plasticity. In case of felsic volcanic product, like ignimbrites and pumice rich pyroclastic deposits, change their color into yellow, orange to brownish color. The weathering represents instability of slopes, landslides, intense water erosion (Figure 4-38, 4-39).

Figure 4-38. On the left residual soil of ignimbrite (Dale, BZ264); on the right, instability of slope due to weathering in northern Gamo.

Figure 4-39. On the left weathered rhyolitic ignimbrite; on the right, weathered basalt from Gamo highlands.

5. Morphotectonic Analysis

The morphotectonic analysis was performed on entire structure of the Main Ethiopian Rift. The map of morphotectonic analysis show interpretation of major tectonic lineaments (Figure 5-1). The map consists of rift valley of MER, for which the strikes were obtained. The strikes of the lineaments were obtained and are plotted in Figure 5-2. The rift valley is bordered by major boundary faults, the rift floor itself is notably affected by faulting. The intensity of faulting decreases southwards. For the northern segment of MER (NMER), 1031 lineaments were attributed and the overall strike points to NE direction. For the central segment CMER, 814 lineaments were attributed and their overall strike points to NNE direction, and for the SMER 522 lineaments were attributed in total with overall strike pointing to N–S direction, (see electronical supplementary Tab. 1). The axis of the rift valley progressively narrows southwards (Figure 5-2).

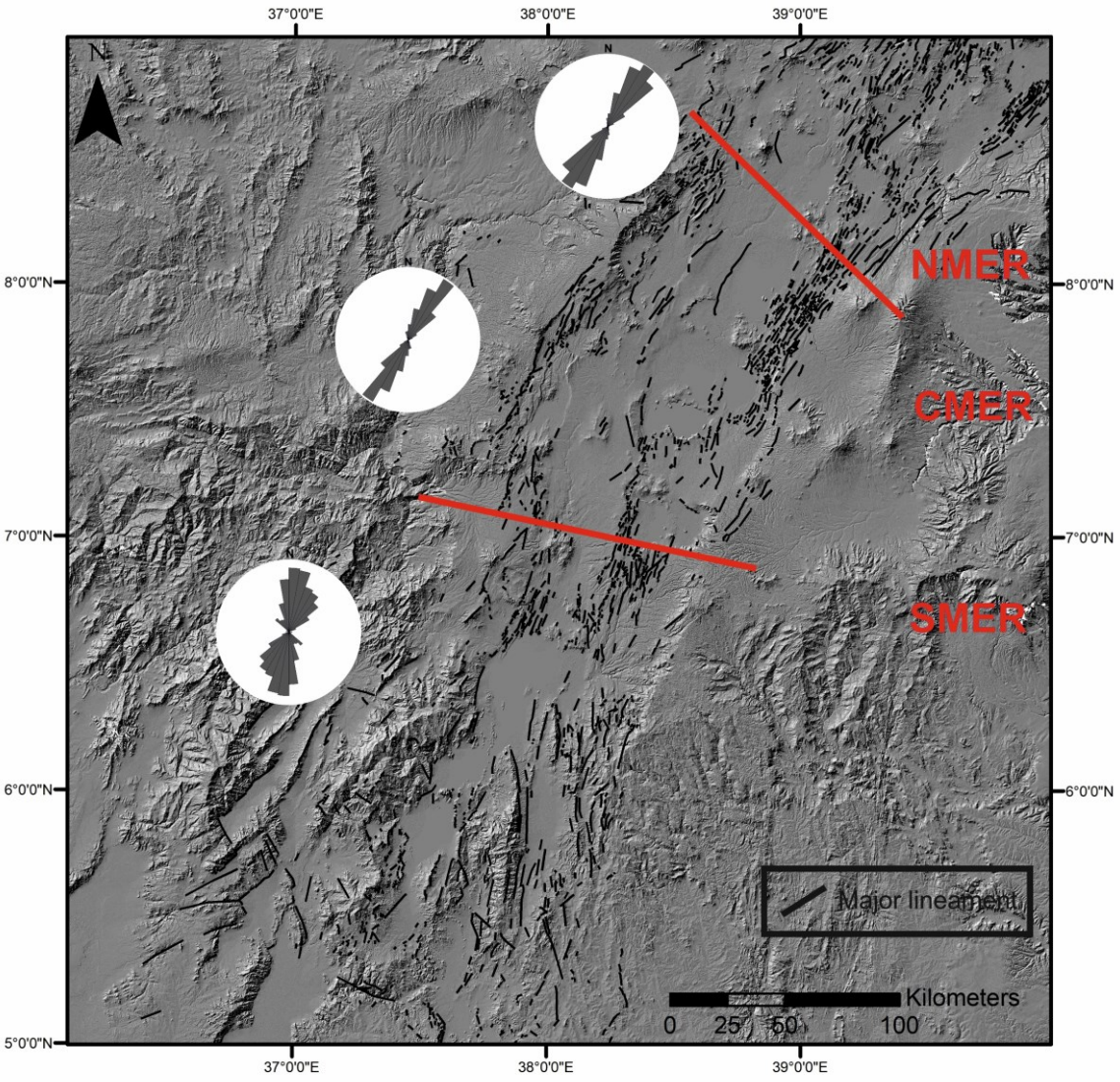

Figure 5-1. Morphotectonic analysis of MER, line indicate boundary between individual segments after (Corti, 2009).

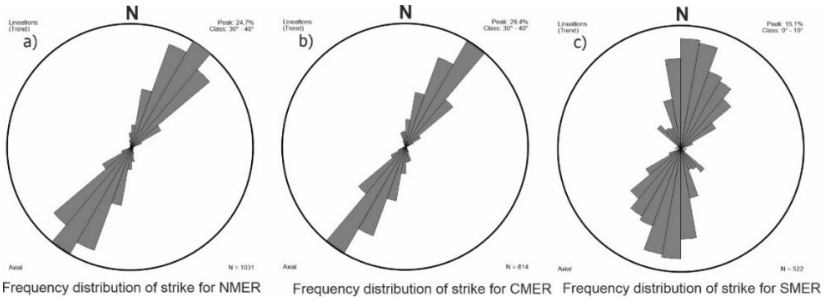

Figure 5-2. Results of morphotectonic analysis for individual rift segments.

6. Tectonics

The geology of Southern Ethiopia consists of two main parts, the basement metamorphic rocks of Proterozoic age and the Main Ethiopian Rift. The metamorphic basement rocks, as part of Southern Ethiopian Shield, are associated with Pan-African orogeny (Stern et al., 2012; Verner et al., 2021; Worku and Schandelmeier, 1996). These rocks had captured multiple deformations which were recognized in the field as schistosity, folding, compositional banding, jointing (Figure 4-1, 4-2, 4-3).

The second part of Southern Ethiopia geology consist of the southern segment of the Main Ethiopian Rift. As the MER represent the internal part of East African Rift System, it records extension between Nubian and Somalian plate. This extension leads into deformation of the continental crust via faulting and by magmatic activity. The SMER preserve characteristic tectomagmatic evolution including pre-rift flood basalt eruption from Eocene to Oligocene, followed by fault-dominated syn-rift stage from Miocene to Pliocene, which had formed the rift valley, up to magma-dominated extension and associated volcanism in break-up stage, as we see it today (Agostini et al., 2011; Corti, 2009; Ebinger, 2005; Ebinger and Casey, 2001; Kendall et al., 2005).

6.1. Primary Structures

The volcanic and volcano sedimentary rocks display a variety of primary fabrics both in pre- and syn-rift sequences of SMER. The primary fabrics of volcanic and volcano-sedimentary rocks are mostly defined by planar preferred orientation of rock-forming minerals, lithic fragments and stretched welded pumice fragments (Figure 4-13). The volcanic rocks, especially ignimbrites and pyroclastic deposits, show bedding with small dipping angle (Figure 6-1). The origin of bedding within volcanic deposits (ignimbrites and related pyroclastic deposits) is interpreted as flow-stretching of viscous silicic lava or hot glass fragments during the flow (Figure 4-13). The volcanic rocks exhibit flow-foliation presented by elongated grains (Figure 4-22.). The primary fabrics are also locally folded into asymmetric open folds due to a lava flow or origin of a domal structure resulting in rheomorphic folds in rhyolite domes with ignimbrites and subordinate obsidian flows (Figure 4-21, 4-32). The contacts of distinctive volcanic flows and individual lithologies are in most cases subparallel to gently dipping. Locally, the lithologies are separated by faulting (Figure 6-4).

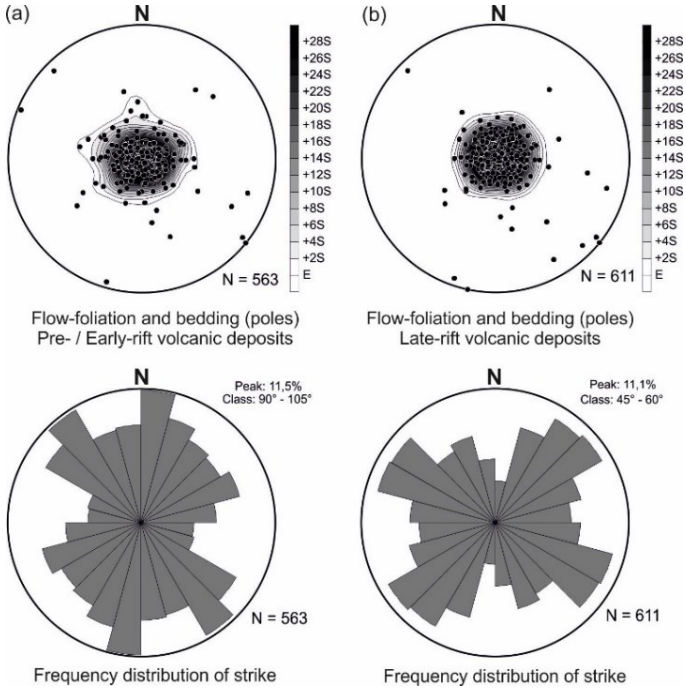

Figure 6-1. Orientation diagrams of the primary structures in pre- to early-rift volcanic and volcano-sedimentary sequences and rose diagrams of corresponding strike orientation shown on the lower row; (a) Flow foliation and bedding planes (poles) in the pre-rift to syn-rift volcaniclastic rocks deposits and frequency distribution of strike; b) Flow foliation and bedding planes in late-rift deposits and frequency distribution of strike, data from Sidama and Gamo. Equal projection to the lower hemisphere.

6.2. Brittle Tectonics

The study area is affected by several sets of brittle structure, e.g., normal faults to oblique-slip faults and fault zones, and extensional joints. The most prominent structural feature modifying the geological framework is represents normal faults (Figure 5-1, 6-4).

Faults

The vast majority of these faults are parallel with the (NNE)(N)–(SSW) (S) oriented axis of the rift and morphological escarpments, trending ~NNE–SSW, ~N–S or ~WNW–ESE direction (Figure 5-1). These faults are chiefly vertical normal faults with well-developed steeply plunging slickensides (Figure 6-2a, 6-3). From studied faults, lineation asymmetry corresponds to a normal movement in the direction of the slickensides. The minor oblique to strike-slip fault with both left- and right-lateral kinematic indicators were mapped. A subordinate set of normal faults has a ~E–W trend (Figure 6-2a). The frequency in the orientation of faults in individual directions is shown on the rose diagram (Figure 6-2a). Locally, cataclasite fault breccia was observed along main fault zones (Figure 6-3).

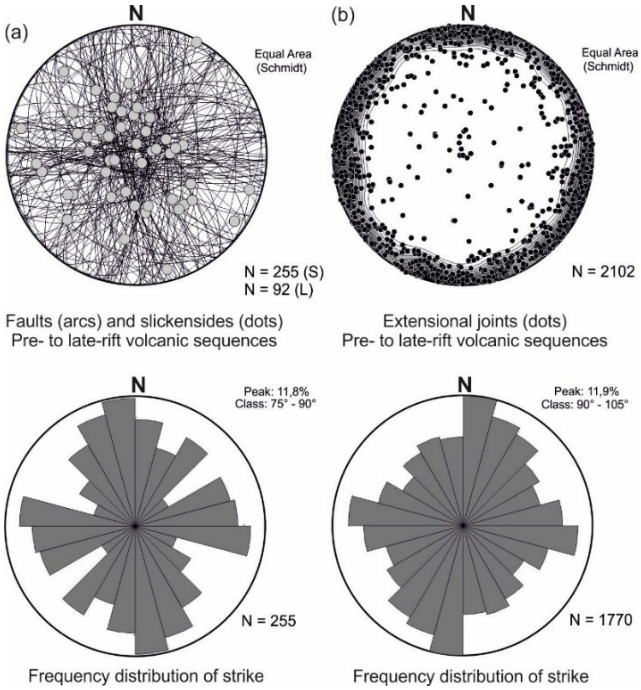

Figure 6-2. Orientation diagrams (upper row) and rose diagrams of corresponding strike orientation shown on the lower row; (a) Faults / fault zones in pre- to late-rift volcanic deposits (arcs), slickensides (dots) and frequency distribution of fault strike; (b) Extensional joints in pre- to late- rift volcanic deposits (poles) and frequency distribution of joint strike, data from Sidama and Gamo.

Figure 6-3. On the left fault with well-preserved slickensides (BZ199); on the right fault breccia from northern Gamo.

Figure 6-4. On the left multiple normal faults with orientation parallel to the rift (Diguna Fango Volcano, SD002); on the right prominent normal fault in Lake Chamo.

Extensional Joints

Another prominent structure related to rift are the extensional joints. The data obtained from joints provide useful information about stress field, as joints their planes define the trajectories of principal stress σ3 (Pluijm and Marshack, 2004). Extensional joints are present both in basement metamorphic and volcanic rocks (Figure 4-1, 4-11, 6-5). Extensional joints trend ~N(NNE)–S(SSW) or W(WNW)–E(ESE) direction (Figure 6-2b). The orientation of extensional joints is largely consistent with regional faults of MER. The spacing between individual joints vary from a few cm up to several meters.

Figure 6-5. On the left extensional joints in rhyolitic ignimbrite (northern Gamo); on the right in pyroclastic fall deposits (north of Lake Abaya, KE407).

6.3. Paleostress Analysis

The paleostress analysis represent powerful tool in order to understate and determine the stress field and geodynamics evolution of study area. The geodynamics processes are mainly controlled by stress field and its interpretation is key factor in understanding tectonic evolution of the rift system (Delvaux et al., 1997; Maerten et al., 2016). However, it is

necessary to be cautious using and interpretating paleostress data. It needs to be taken account the possibility of reactivation of faults, as the preserved structures can represent overprinted state with different stress tensor (Nemcok and Lisle, 1995).

Phase I

In the first phase the stress analysis was assigned for 23 faults. The principal stress σ1 is in the vertical position, the principal stress σ3 lies in the horizontal direction below the azimuth about 90 °.

Phase II

In the second phase the stress analysis was assigned for 10 faults, out of a total of 35. The principal stress σ1 is oriented in NNE–SSW direction. The values of σ2 and σ3 are similar and the principal stress σ3 is oriented at medium angle and azimuth of about 255 °.

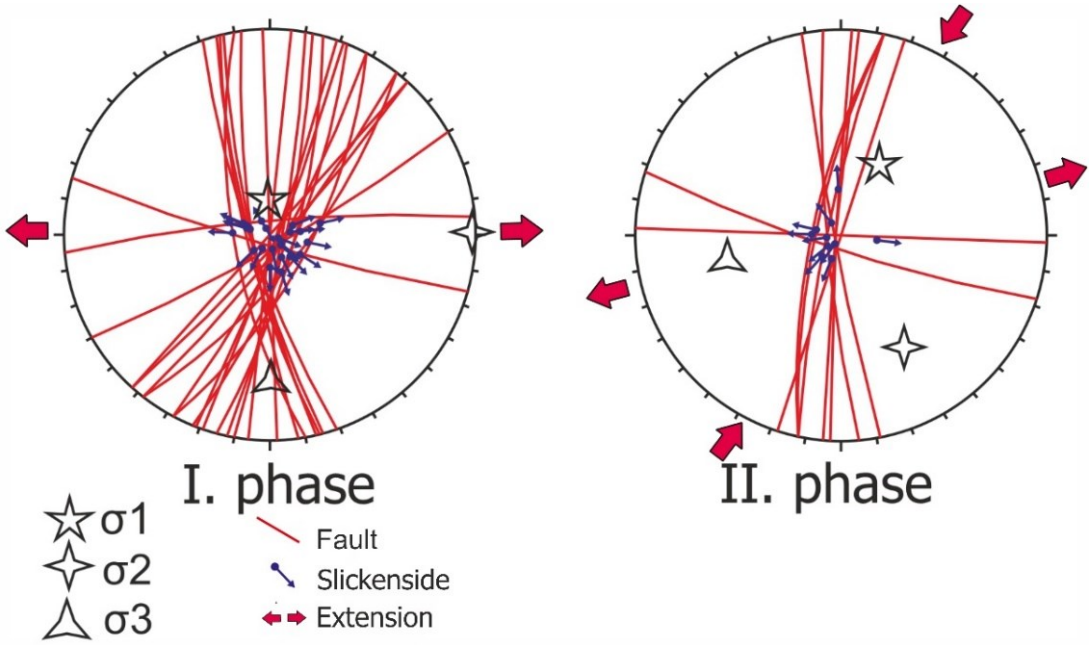

Figure 6-6. Results of paleostress analysis, equal projection to lower hemisphere.

6.4. Gravimetry

The gravity was applied in order to characterize large-scale structures and boundaries between distinct lithologies with different densities (Figure 6-8). Further, detailed investigation of gravity data by Linsser indications (Figure 6-9,10) was performed. For gravity investigation, different densities for individual lithologies were used (Tab. 7). However, the investigation on the very most western part is limited by of lack of data (Figure 6-7). The whole area is characterized by a significant gravity gradient between the deep gravity low (-270

mGal) on northeastern part from the area of interest, and the gravity high (-70 mGal) on the west to southwest from the area of focus, (see electronical supplementary Tab. 2).

The low values of Bouguer anomalies are associated with thickened part of crust with a low density upper crustal material. The low gravity anomalies situated on the northeast are related probably to the ignimbrite succession (see geological map of Dila, Yismaw et al. 2015). In contrast, the high values of Bouguer anomalies on the westernmost part of the area of interest and southwest are possibly related to series of thick pre-rift related volcanic rock of basaltic composition (see Annex-1).

Further, high gravity anomalies could be also caused by a thickened lithosphere which is also reflected in seismic investigation of Dugda et al. (2005), Keranen et al. (2009), and Ogden et al. (2021) indicating the depth of the Moho, which varies here between 42 km on the N and NE and 36 km on the S and SE (Kassa et al., 2021).

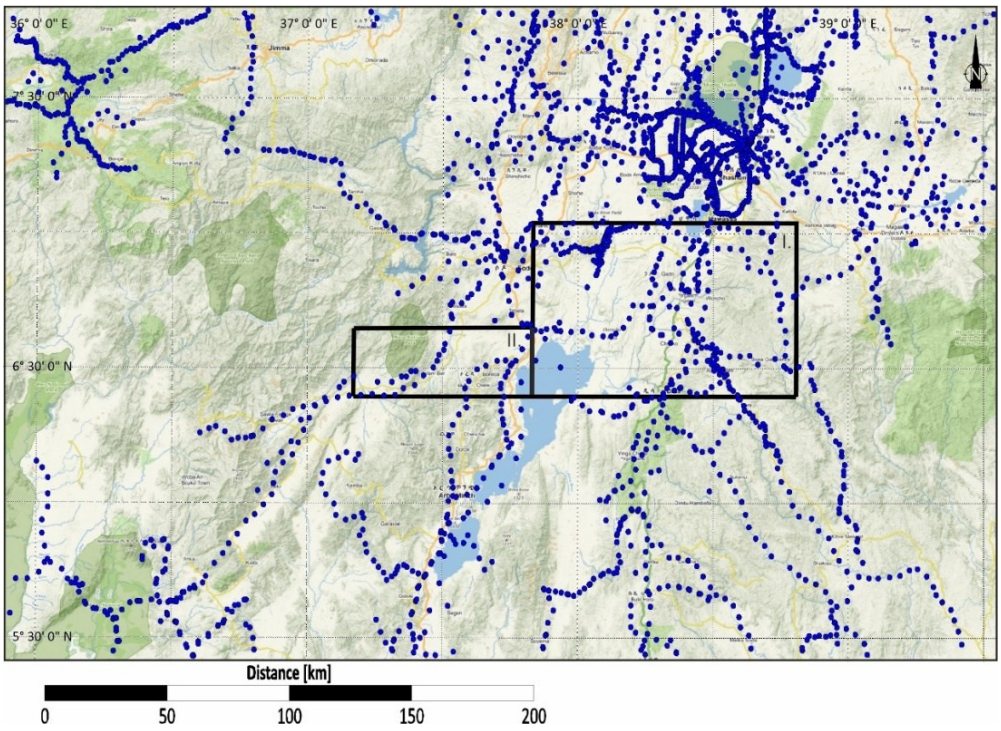

Figure 6-7. Topographic map showing density of the gravity data points.

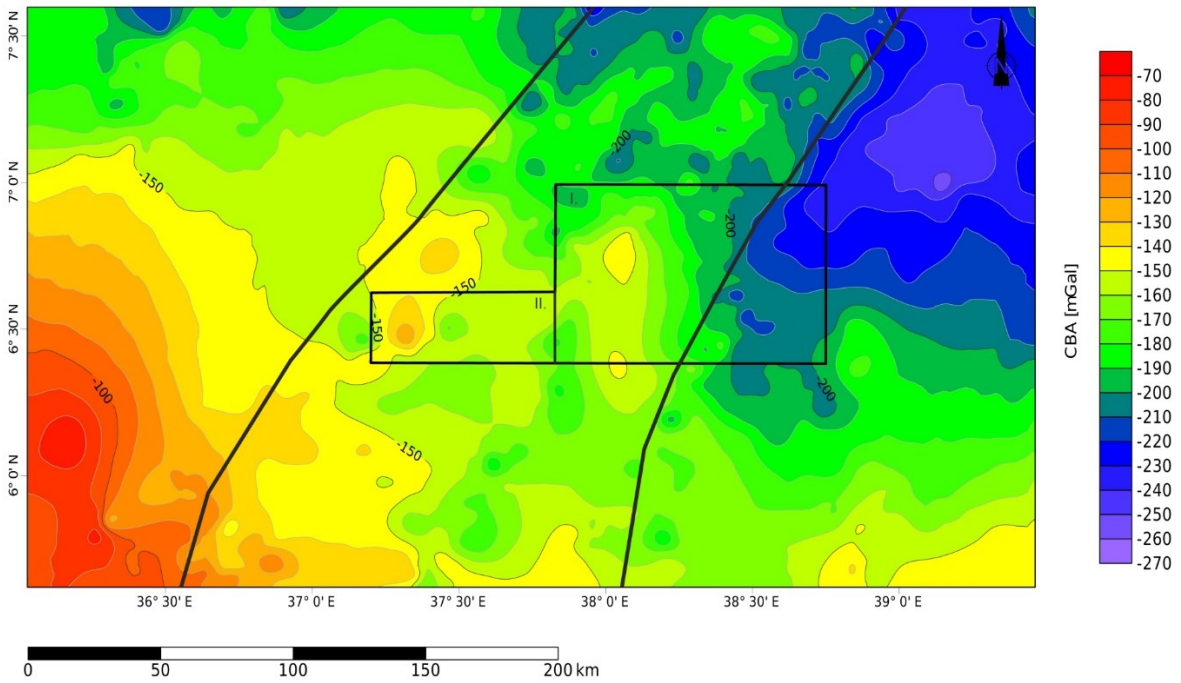

Figure 6-8. Map of complete Bouguer anomalies with selected study area and schematic rift valley boundary.

The gravity map with Linsser indications (Figure 6-9, 6-10) indicate field with the highest gradient of CBA. The size of the sign is function of how well the gravity data fits the theoretical response of a supposed model of vertical step. The higher the correlation, the bigger the sign. The dip of the sing indicates direction of the gradient slope from high to low.

From right to left, the gravity lows on eastern part of map I. (Figure 6-9) are related to low density volcanic acidic rocks (ignimbrites and pyroclastic deposits). The gravity low (-200 to -210) is in a good correlation with syn-rift basalts of lower thickness, the gravity low (-190 to -160) can be attributed to syn-rift related acidic rocks and pyroclastic deposits of larger thickness. The signs of Linsser indications correlate both with faults and lithological boundaries. The gradient on top right corner probably corresponds to the rim of the Hawasa Caldera (see Annex-1, Annex-2).

The high gravity values in eastern part of map I. (Figure 6-9) are attributed to a thick volcano-sedimentary succession filling the rift valley, here the Lake Abaya. The indications marked on the left corresponds to a major boundary fault on the edges of Lake Abaya (Figure 6-9).

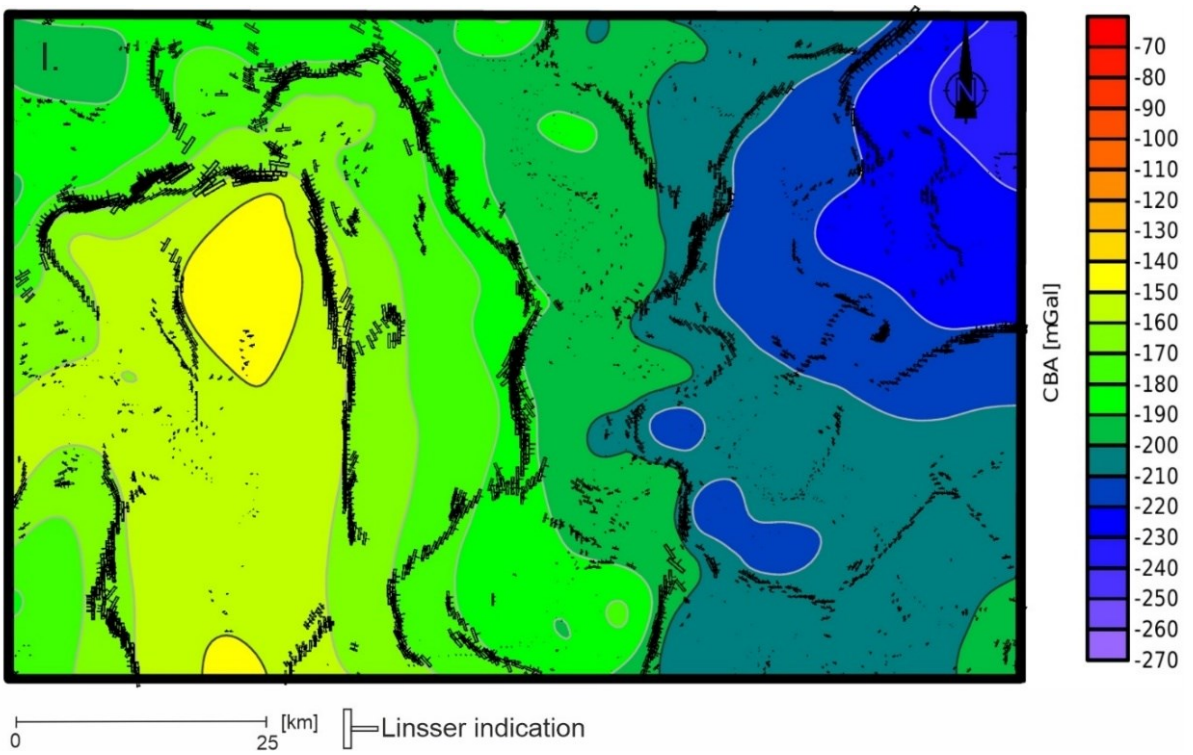

Figure 6-9. Gravity map of complete Bouguer anomalies with Linsser indications for Sidama area.

The western part of the study area on map II. displays higher gravity anomalies (Figure 6-10) in comparison to eastern part of the map I. (Figure 6-9). From right to left, the Linsser indication signs correspond to major fault on western flank of Lake Abaya, dipping to the east. Further, moving to the west, the indications mark another large fault dipping to the east. This boundary also corresponds to lithological transition between pre-rift basalts and trachytes. The highest gravity values are situated western of Maze National Park. Here the elevation decreases below 1 km. This area corresponds to Beto Basin, linked with Broadly Rifted Zone (Ebinger et al., 2000). Here the high gravity anomalies could be attributed to metamorphic basement rock overlined by basalts and sediments (see Ebinger et al., 2000).

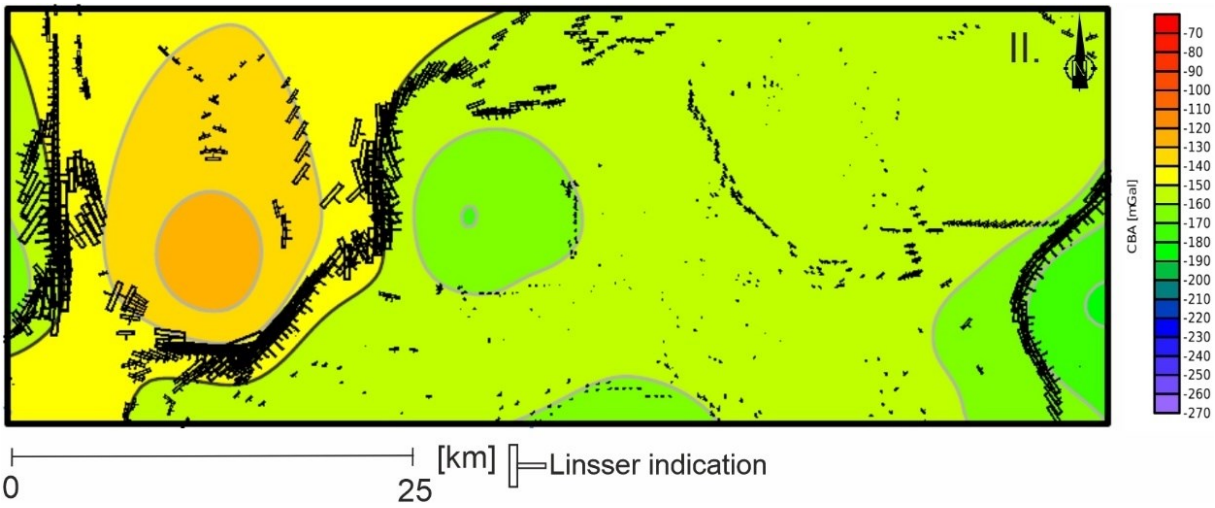

Figure 6-10. Gravity map of complete Bouguer anomalies with Linsser indications for the Gamo area.

The gravity maps (Figure 6-8, 6-9) correlates with the geological map of Sidama area (Annexes 1). The transition from lower to higher gravity fit well with the geological map together with major faults, separating pre-rift basalts with syn-rift ignimbrites and pyroclastic deposits. The Linsser indications follows trends of the major faults, further reflects lithological boundaries between the pre-rift and late-rift volcanic deposits. (Figure 6-9). The gravity maps (Figure 6-8, 6-10) are in agreement with the geological map of Gamo area (Annexes 2). The Linsser indications fit with the trends of the major faults of Gamo area. The gravity high reflects the distribution of dense basement rock (see Annex 2, Annex 3; Igneous and metamorphic rocks assemblage).

7. Geochemistry

The classification based on TAS diagram allows to identify study rock samples based on relative proportions of alkalis ($Na_2O + K_2O$) and SiO_2 content (Figure 7-1 b, total alkalis vs. SiO_2; LeBas et al., 1986) as rhyolite, basalt, trachyte. The TAS classification reveal bimodal (basic-acid) distribution of volcanic rocks with a lack of intermediate compositions based on relative proportions of alkalis and silica content. Dashed line indicate boundary between alkaline and subalkaline suite. The Nb/Y vs Zr/Ti diagram (Figure 7-1a) of Winchester and Floyd, (1977) modified after Pearce (1996) allows classification for weathered rocks as these elements remains immobile during alteration processes (Pearce and Norry, 1979). The Nb/Y vs Zr/Ti diagram reveal alkaline rock suite (Figure 7-1a).

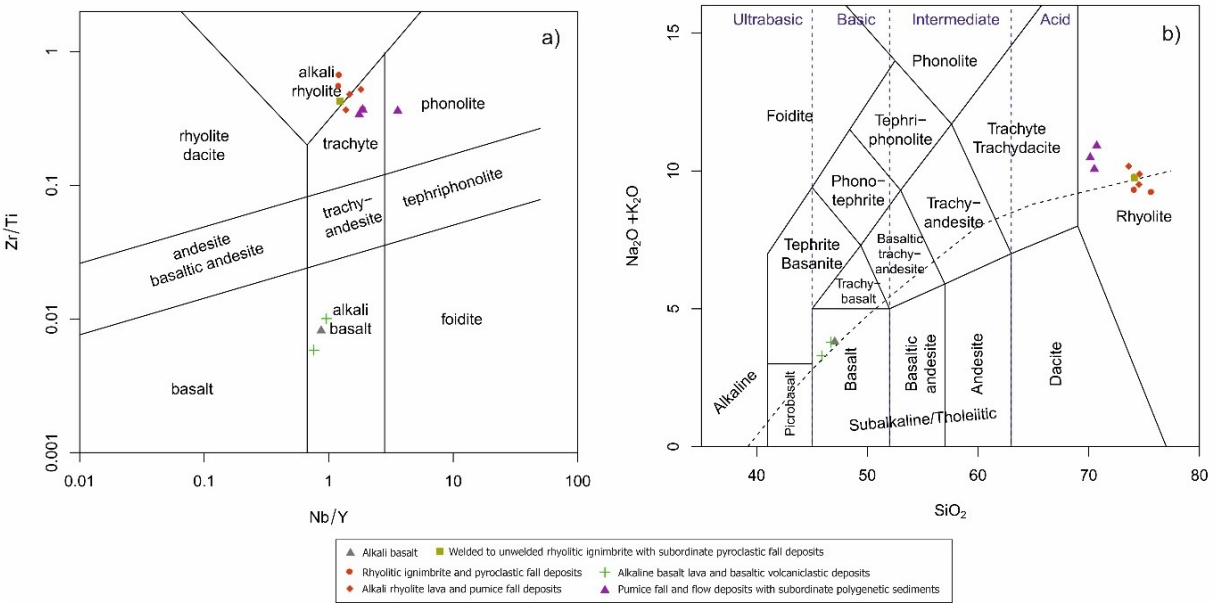

Figure 7-1. Chemical composition of the volcanic rocks; (a) Nb/Y versus Zr/Ti diagram (Pearce, 1996); (b) Total alkalis (Na2O + K2O) versus SiO2 (TAS; LeBas et al., 1986).

7.1. Basic Rocks

The alkali basalt (see Annex-5, Tab. 7) occurs around eastern rim of the Hawasa Caldera and make a massive lava flows with presented flow structures (Figure 4-20). The studied basic samples of alkaline basalt lava and basaltic volcaniclastic deposits (see Annex-5, Tab. 7) are situated along the major fault in the rift valley (see geological map of Sidama area, Annex-1) and forms small scoria cones.

The TAS classification for basic rock falls into alkaline basalt field (Figure 7-1b). The basic rocks exhibit lower content of SiO_2 (44-45 wt. %), K_2O (0.68-0.92 wt. %), Na_2O (2.56-2.8 wt. %) in comparison to acid rocks. Further, they display elevated content of MgO (5.64-7.9 wt. %), TiO_2 (2.75-2.95 wt. %), Fe_2O_3 (12.3-13.5 wt. %), Al_2O_3 (14.01-15.05 wt. %), and CaO (10.11-11 wt. %) (Tab. 1).

Basic rocks in Nb/Y vs Zr/Ti diagram (Figure 7-1a) are characterized by low Zr/Ti (0.005-0.01) ratios and high Nb/Y (0.76-0.95) ratios which corresponds to alkali basalt field (Winchester and Floyd, 1977).

Chondrite-normalized REE patterns of basic samples (alkali basalt, alkaline basalt lava and basaltic volcanoclastic deposits) (Figure. 7-2a) display a gently decreasing trend from LREE to HREE and positive Eu anomalies (1.09-1.13). The basic samples have strongly elevated content of Sr (527-584 ppm), Ba (272-365 ppm) in comparison to acidic rocks. Alkali basalts are further enriched in Ni, Cu, and Co. The total content of REE for basic rock is low (168-175 ppm). In primitive mantle-normalized multi-element variation diagram (Figure 7-2b) the basic rocks correspond to intraplate volcanic pattern with a decline in Pb (0.3-1.4 ppm) and Cs (0-0.3 ppm) (Winchester and Floyd, 1977).

7.2. Acid Rocks

The studied acid samples of rhyolitic ignimbrite and pyroclastic fall (see Annex-5, Tab. 7) are related with Hawasa Caldera eruption (see Rapprich eds., 2013) and extensively cover rift valley on both mapped area (see Annex-1, Annex-2). This unit is accompanied by alkali rhyolite lava and pumice fall deposits, which occur along major faults in the rift valley center. The welded to unwelded rhyolitic ignimbrite with subordinate pyroclastic fall deposits occur in vicinity of Hawasa Caldera and it's related to main stage of eruptions in forming of the Corbetti Caldera (see Rapprich eds., 2013). The pumice fall and flow deposits with subordinate polygenetic sediments represents the last stage od Hawasa Caldera eruption (Hroch et al. 2018).

The TAS classification for acidic rocks (Figure 7-1b) falls into subalkaline to alkaline rhyolitic field. However, in Nb/Y vs Zr/Ti diagram (Figure 7-1a) these rocks are more scattered and corresponds to alkali rhyolites, trachytes, and phonolite. The acidic rocks display high content of SiO_2 (67-75 wt. %), suggesting highly evolved acidic rocks (Best, 2003, p88-121). The content of Al_2O_3 is slightly lower (10.46-12.76 wt. %) compared to basic rocks. Further they exhibit elevated content of K_2O (4.5-5.4 wt. %), slightly higher Na_2O (4.19-6.0 wt. %). In contrast, content of CaO is low (0.11-0.31 wt. %), as TiO_2 (0.22-00.51 ppm). The acid rock falls into boundary of alkaline and subalkaline/tholeiitic suites. On the other hand, acid rocks display Nd/Y ratios (1.19-3.58) which is normal to alkaline series (Pearce, 1996).

Chondrite-normalized REE patterns of acid samples display negative Eu anomalies (0.34-0.59) and positive Ce anomaly (Figure 7-2a). The total amount of REE for acid rock is high (289-790 ppm). In primitive mantle-normalized multi-element variation diagram (Figure 7-2b), acid rocks notably decrease in content of Ba (3-150 ppm), especially rhyolites and ignimbrites, further in Sr (1-14 ppm), P_2O_5 (0.01-0.04 ppm), and TiO_2 (0.22-0.51 ppm).

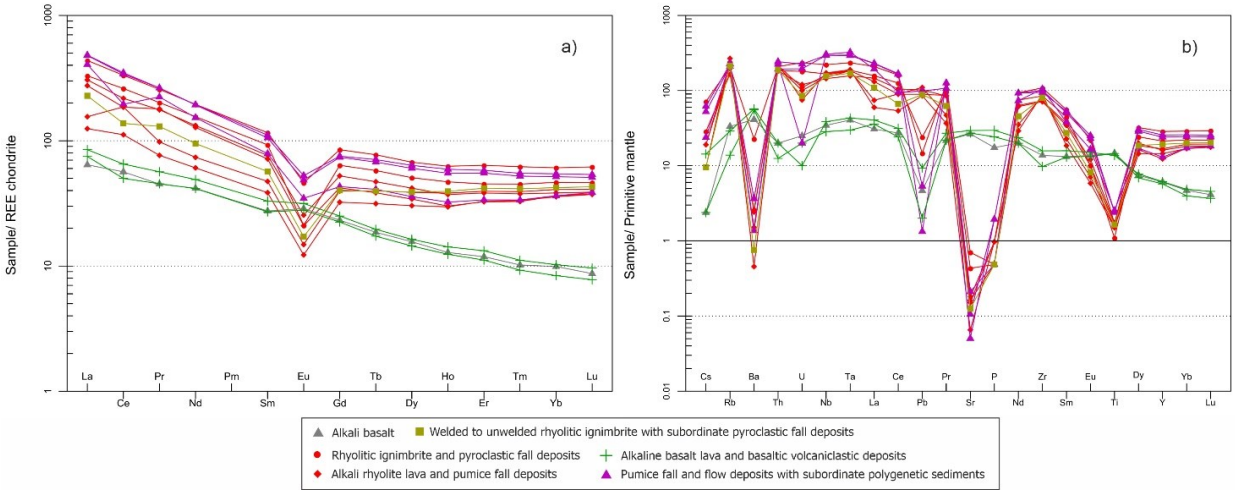

Figure 7-2. Chemical composition of the volcanic rocks; (a) chondrite-normalized rare earth element (REE) patterns (the values for normalization are based on Boynton 1984); (b) primitive mantle-normalized multi-element variation diagrams (the values for normalization are based on McDonough and Sun, 1995).

8. Discussion

Based on comprehensive geological research of the northern flank of the Southern Main Ethiopian Rift (SMER; for location see Figure 1-1) including (a) field geological and structural mapping on a 1 : 50,000 scale resulted in compilation of geological maps (Annex 1, Annex 2), (b) detailed petrological and geochemical description of individual lithologies, (c) morphotectonic analysis of Digital Elevation Model (DEM), (d) paleostress analysis calculated based on rift-related normal faults with slickensides, and (e) gravity pattern assessment including calculation of Linsser indications, the entire geodynamic and magmatic evolution of northern flank of the SMER is discussed and interpreted.

8.1. Field Geological Mapping and Lithological Pattern

The geological mapping of the area of our interest (Figure 1-1, Annex-4) resulted in compilation of geological maps on a scale 1: 250,000 (this study; Annex-1, Annex-2) shows a unique geological settings of northern flank of the Southern Main Ethiopian Rift and uplifted plateaus. The individual rock lithologies were analyzed based on geological position, appearance, structural pattern, optical microscopy and petrographical description, chemistry of rock forming minerals, and their relationships.

The metamorphic rocks belonging to the Neoproterozoic Arabian-Nubian Shield (e.g., Fritz et al., 2013) form the lowest unit exposed mainly in the south-eastern margin of map segment (Annex-1), mainly in deeply eroded valleys of Gambelto, Gonjebe, and Genale rivers. Three distinct volcanic events took place within the studied area (Figure 1-1) can be distinguished: (a) “Pre-rift” stage (Eocene to Oligocene), (b) “Early-rift stage” (Miocene) and (c) “Late-rift” stage (Pliocene to Holocene). The “pre-rift” stage volcanic activity started by subsequent volcanic eruptions of Ethiopia-Yemen Flood Basalts and surrounding Amaro-Gamo Basalts (e.g., Ebinger et al., 1993) alternating with numerous ignimbrite flows alternated by trachyte lava flows (e.g., Halcrow, 2008). This volcanic episode was characterized by extrusion of flood tholeiitic to alkaline lava flows (Kieffer et al., 2004). The eruption of these flood basalts occurred mostly through extensional fissures (e.g., Corti, 2009). Most of these basalts and related felsic rocks were apparently erupted in a short time interval mainly between 31 and 28 Ma (e.g., Ukstins et al., 2002). Subsequent “early-rift” volcanic sequence comprises predominantly rhyolite lavas, volcanic breccia, and glassy-rich welded ignimbrites. The “late-rift” stage is associated with deposition of ignimbrites and rhyolite lava flows with dominant exposure in the north-western part of mapped area (Annex-1). These ignimbrites are locally covered by basalt lava flows and related pyroclastic deposits. The deposition of the prevailing rhyolitic ignimbrites and pyroclastic deposits are associated with formation of the Hawasa and Corbetti calderas (Rapprich ed., 2013; Hutchison et al., 2016).

The major rift-related extension and uplift since ca. 30 Ma (Eocene) comes from continental extension associated with magmatic (volcanic) activity driven by ascent of large mantle plumes impinging at the base of the lithosphere and subsequent eruptions of large volumes of fissural basaltic lava flows alternated by ascent of crustal melts derived from surrounding continental crust (e.g., Gani et al. 2007).

8.2. Geochemistry

Studied basalts belonging to Eocene pre-rift volcanic formations (alkali basalt, alkaline basalt lava and basaltic volcanoclastic deposits) reveal a lower Zr/Ti (0.005-0.01) ratios and high Nb/Y (0.76-0.95) ratio, also display a gently decreasing trend from LREE to HREE and positive Eu anomalies (1.09-1.13), further enriched in Ni, Cu, and Co corresponding to alkaline basalts (Winchester and Floyd, 1977) in intraplate conditions. In addition, acidic rocks which are representative volcanic rocks for late-rift stage (rhyolites, rhyolite ignimbrites and felsic fall-deposits) have alkaline to subalkaline composition (according to classification of Pearce, 1996) displaying negative Eu anomaly (0.34-0.59) and decrease in Ba content (3-150 ppm). The drop in content in acid rocks of Ba and Sr could be caused by the fractionation of feldspar, further decreased content of P might be caused by fraction of apatite, and in case of Ti it could be caused by fraction of Fe-Ti oxides (Neumann and Ramberg, 1978). The positive Eu anomaly in basic rocks indicate plagioclase enrichment as Eu^{2+} substitute for Ca 2+, whereas in acidic rock the negative Eu anomaly suggest fractionation of plagioclase.

The magmatic (volcanic) activity associated with MER during the break-up stage was caused predominantly by decompression melting of the mantle (White, 1992; Ziegler and Cloetingh, 2004). Rooney et al. (2012) supposed the main source for “late-rift stage” magmatism is more variable including ascent of mantle plume, melting of asthenospheric upper mantle, and also the continental lithosphere. In contrast, Ayalew et al. (2016) state the source of magma to be from veined lithosphere as a result of the mantle upwelling and negligible crustal assimilation.

The studied rock samples of Pleistocene ages are both acid and basic, supporting bimodal suite for Quaternary volcanism, typical for continental rift setting (Abebe et al., 2007; Neumann and Ramberg, 1978). The most recent volcanic activity is focused along WFB tectomagmatic segments (Abebe et al., 2005; Boccaletti et al., 1998). From whole-rock geochemistry analysis, the acid rocks have high silica content which points on highly evolved rocks (Best, 2003).

8.3. Paleostress Analysis and Tectonic Evolution

Principal faults and fault zones related to the Main Ethiopian Rift significantly affect the geological framework of the study area and are mostly parallel with the NNE(N)–SSW(S) oriented rift axis and morphological escarpments. These faults are mostly vertical, trending

~NNE–SSW to ~N–S and are associated with well-developed steeply plunging slickensides and normal kinematics. The main rift-parallel faults can be grouped into structures forming main escapements of the rift valley and faults within the rift valley, commonly having a sigmoidal shape and making right-stepping en-echelon pattern known also as Wonji Fault Belt (Boccaletti et al., 1998; Pizzi et al., 2006). Subordinate faults are steeply to moderately dipping with ~WNW–ESE trend associated with well-developed steeply to moderately plunging slickensides and normal to oblique-slip kinematics. Extensional joints are mostly vertical, trending ~N(NNE)–S(SSW) or W(WNW)–E(ESE). Their orientation is largely consistent with regional faults. The morphotectonic analysis is fully consistent with mapped faults.

The results of paleostress analysis provided consistent set of 38 faults which define 2 subsequent tectonic phases. The first phase reveals extension in E–W (N90°) direction, slightly oblique to the rift axis. The second phase shows gently shifted direction of continental extension in E(ENE)–W(WSW) (N80°) direction, oblique to rift axis. These results are in agreement with paleostress data provided by Corti et al. (2013) in SMER showing an extension in ~W–E (100°) direction with local variation of the stress field. Similar E–W extension was also provided by Boccaletti et al. (1998), Philippon et al., (2014) or Pizzi et al. (2006). In contrast, Muluneh et al. (2014) describes WNW–ESE extension derived from focal mechanism inversions for MER as a consequence of local deviation of the stress field. The oblique extension is possibly caused by WFB induced by magmatic activity along these segments (Agostini et al., 2011). The overall structural pattern of the CMER and SMER resulted in continental extension of Nubian and Somalian plates (Agostini et al., 2011) being propagated via pre-existing zones of weakness (e.g., Ziegler and Cloetingh, 2004; Corti et al. 2008). The tectonic evolution of MER is currently highly debated. In general, the model either suggest polyphase or constant extension, but they also differ in timing and kinematic directions (Corti, 2009; Erbello et al., 2016).

8.4. Gravimetry

The geophysical investigation is poorly constrained compared to other MER sectors (Kebede and Mammo, 2021). Complex gravity analysis of nearly entire structure of MER was provided by Mahatsente et al. (1999, 2000), Mickus et al. (2007) and Kassa et al. (2021). The gravity maps (Figure 6-8, 6-9, 6-10) showing gravity field distribution and Linsser indications in SMER, correlate well with the geological maps (Annexes-1, Annexes-2). The transition from lower to higher gravity fit with the geological map together with major fault, separating pre-rift basalts with syn-rift ignimbrites and pyroclastic deposits. The gravity high besides thick layers of volcanic rock and dense metamorphic rocks might be related to the rift-related tectonics and / or asthenospheric upwelling and plume intrusion (Kassa et al., 2021; Mahatsente et al., 2000; Mickus et al., 2007). In addition, recent work of Kebede and Mammo (2021) reveals a detailed investigation within SMER by method of full tensor gravity gradiometry. The gravity data over

on Figure 6-8, and those obtained by Kebede and Mammo, (2021), are in agreement. The SMER doesn't reveal high Bouguer anomaly as Afar and NMER, as the level of lithospheric thinning is not sufficient enough to cause increase gravity anomaly, which also points to southwards decreasing in rift maturity (Mahatsente et al., 2000; Mickus et al., 2007).

9. Conclusions

Based on comprehensive geological research of the northern flank of the Southern Main Ethiopian Rift including geological mapping, field structural research, remote sensing analysis, gravity survey, petrological and geochemical assessment of main rock lithologies following conclusions can be drawn:

(a) The studied area in the northern flank of the Southern Main Ethiopian Rift (SMER) recorded typical continental rift-related tectonic and magmatic evolution including (a) pre-rift (Eocene to Oligocene) volcanic activity initiated by extensive flood (plateau) alkaline basalt to trachybasalt basalt eruptions due to crustal thinning and mantle plume(s) ascent, followed by (b) fault-dominated early-rift (Miocene) bimodal volcanism associated with origin of the rift valley and (c) late-rift (Pliocene to Holocene) bi-modal volcanic activity comprising alternation of alkaline basalts and have alkaline to subalkaline rhyolite to trachyte lava flows, formation of numerous lava domes, cinder cones, calderas and large deposition of felsic pyroclastic material.

(b) Principal faults and fault zones are mostly vertical, parallel with the NNE(N)–SSW(S) oriented rift axis and prominent morphological escarpments, bearing steeply plunging slickensides and normal kinematic indicators. Subordinate faults are steeply to moderately dipping with ~WNW–ESE trend associated with well-developed steeply to moderately plunging slickensides and normal to oblique-slip kinematics.

(c) The regional paleostress field calculated from the mapped faults reflects the continuing rifting between the Nubian and Somalian plate, in the succession of earlier E-W extension (N90°) direction, changing to E(ENE)–W(WSW) extension (N80°), gently oblique to the rift-axis.

The Ethiopian Rift System represent a unique insight into process of continental rifting and its detailed research could unravel open questions such are the causes, mechanisms, and timing of initiation of rifting, changes in kinematics, and directions of continental extension, which I would like to focus on my Ph.D. studies.

References:

Abdelsalam, M.G., Stern, R.J., 1996. Sutures and shear zones in the Arabian-Nubian shield. J. African Earth Sci. 23.

Abebe, B., Acocella, V., Korme, T., Ayalew, D., 2007. Quaternary faulting and volcanism in the Main Ethiopian Rift. J. African Earth Sci. 48.

Abebe, B., Coltorti, M., Pizzi, A., 2005. Rates of Late Quaternary deformation along the Wonji fault belt in the Lakes Region, Main Ethiopian Rift. Rend. della Soc. Geol. Ital. 1.

Agostini, A., Bonini, M., Corti, G., Sani, F., Mazzarini, F., 2011. Fault architecture in the Main Ethiopian Rift and comparison with experimental models: Implications for rift evolution and Nubia-Somalia kinematics. Earth Planet. Sci. Lett. 301.

Angelier, J., Tarantola, A., Valette, B., Manoussis, S., 1982. Inversion of field data in fault tectonics to obtain the regional stress — I. Single phase fault populations: a new method of computing the stress tensor. Geophys. J. R. Astron. Soc. 69.

Ayalew, D., Barbey, P., Marty, B., Reisberg, L., Yirgu, G., Pik, R., 2002. Source, genesis, and timing of giant ignimbrite deposits associated with Ethiopian continental flood basalts. Geochim. Cosmochim. Acta 66.

Ayalew, D., Jung, S., Romer, R.L., Kersten, F., Pfänder, J.A., Garbe-Schönberg, D., 2016. Petrogenesis and origin of modern Ethiopian rift basalts: Constraints from isotope and trace element geochemistry. Lithos 258–259.

Bailey, G.N., King, G., Manighetti, I., 2000. Tectonics, Volcanism, Landscape Structure and Human Evolution in the African Rift. Hum. Ecodynamics.

Baker, B.H., Wohlenberg, J., 1971. Structure and evolution of the Kenya Rift Valley. Nature 229.

Bastow, I.D., Stuart, G.W., Kendall, J.M., Ebinger, C.J., 2005. Upper-mantle seismic structure in a region of incipient continental breakup: Northern Ethiopian rift. Geophys. J. Int.

Bendick, R., McClusky, S., Bilham, R., Asfaw, L., Klemperer, S., 2006. Distributed Nubia-Somalia relative motion and dike intrusion in the Main Ethiopian Rift. Geophys. J. Int. 165.

Bilham, R., Bendick, R., Larson, K., Mohr, P., Braun, J., Tesfaye, S., Asfaw, L., 1999. Secular and tidal strain across the main ethiopian rift. Geophys. Res. Lett. 26.

Boccaletti, M., Bonini, M., Mazzuoli, R., Abebe, B., Piccardi, L., Tortorici, L., 1998. Quaternary oblique extensional tectonics in the Ethiopian Rift (Horn of Africa). Tectonophysics 287.

Boccaletti, M., Mazzuoli, R., Bonini, M., Trua, T., Abebe, B., 1999. Plio-Quaternary volcanotectonic activity in the northern sector of the Main Ethiopian Rift: Relationships with oblique rifting. J. African Earth Sci. 29.

Bonini, M., Corti, G., Innocenti, F., Manetti, P., Mazzarini, F., Abebe, T., Pecskay, Z., 2005. Evolution of the Main Ethiopian Rift in the frame of Afar and Kenya rifts propagation. Tectonics 24.

Bosworth, W., 1987. Off-axis volcanism in the Gregory rift, east Africa: Implications for models of continental rifting. Geology 15.

Bosworth, W., Strecker, M.R., 1997. Stress field changes in the Afro-Arabian rift system during the Miocene to Recent period. Tectonophysics 278.

Bosworth, W., Strecker, M.R., Blisniuk, P.M., 1992. Integration of East African paleostress and present-day stress data: implications for continental stress field dynamics. J. Geophys. Res. 97.

Brown, F.H., Mcdougall, I., 2011. Geochronology of the Turkana Depression of Northern Kenya and Southern Ethiopia. Evol. Anthropol. 20.

Buriánek, D., (eds.) Hroch, T., Verner, K., Megerssa, L., Martínek, K., Yacob, M., Haregot, A., Janderková, J., Šíma, J., Kryštofová, E., Valenta, J., Tadesse, E., Mosisa, A., Balke, G., Legesse, F., Assefa, G., Pécskay, Z., Hejtmánková, P., Krejčí, Z. 2018: Explanatory notes to the thematic geoscientific maps of Ethiopia at a scale of 1 : 50 000, Map Sheet 0638-C2 Dila. 130 pages, 7 annexes, 4 maps. Czech Geological Survey, Prague; AQUATEST Ltd., Prague; Geological Survey of Ethiopia, Addis Ababa.

Calais, E., Ebinger, C.J., Hartnady, C., Nocquet, J.M., 2006. Kinematics of the East African Rift from GPS and earthquake slip vector data. Geol. Soc. Spec. Publ. 259.

Castaing, C., 1991. Post-Pan-African tectonic evolution of South Malawi in relation to the Karroo and recent East African rift systems. Tectonophysics 191.

Chernet, T., 2011. Geology and hydrothermal resources in the northern Lake Abaya area (Ethiopia). J. African Earth Sci. 61.

Chernet, T., Hart, W.K., Aronson, J.L., Walter, R.C., 1998. New age constraints on the timing of volcanism and tectonism in the northern Main Ethiopian Rift - southern Afar transition zone (Ethiopia). J. Volcanol. Geotherm. Res. 80.

Chorowicz, J., 2005. The East African rift system. J. African Earth Sci. 43.

Chorowicz, J., 1992. The role of ancient structures in the genesis and evolution of the East African Rift. Bull. - Soc. Geol. Fr. 163.

Chorowicz, J., Collet, B., Bonavia, F.F., Mohr, P., Parrot, J.F., Korme, T., 1998. The Tana basin, Ethiopia: Intra-plateau uplift, rifting and subsidence. Tectonophysics 295.

Chorowicz, J., Fournier, J. Le, Vidal, G., 1987. A model for rift development in Eastern Africa. Geol. J. 22.

Chu, D., Gordon, R.G., 1999. Evidence for motion between Nubia and Somalia along the

Southwest Indian ridge. Nature 398.

Corti, G., 2009. Continental rift evolution: From rift initiation to incipient break-up in the Main Ethiopian Rift, East Africa. Earth-Science Rev.

Corti, G., 2008. Control of rift obliquity on the evolution and segmentation of the main Ethiopian rift. Nat. Geosci. 1.

Corti, G., Bonini, M., Conticelli, S., Innocenti, F., Manetti, P., Sokoutis, D., 2003a. Analogue modelling of continental extension: A review focused on the relations between the patterns of deformation and the presence of magma. Earth-Science Rev. 63.

Corti, G., Bonini, M., Sokoutis, D., Innocenti, F., Manetti, P., Cloetingh, S., Mulugeta, G., 2004. Continental rift architecture and patterns of magma migration: A dynamic analysis based on centrifuge models. Tectonics 23.

Corti, G., Sani, F., Agostini, S., Philippon, M., Sokoutis, D., Willingshofer, E., 2018. Off-axis volcano-tectonic activity during continental rifting: Insights from the transversal Goba-Bonga lineament, Main Ethiopian Rift (East Africa). Tectonophysics 728–729.

Corti, G., Sani, F., Philippon, M., Sokoutis, D., Willingshofer, E., Molin, P., 2013. Quaternary volcano-tectonic activity in the Soddo region, western margin of the Southern Main Ethiopian Rift. Tectonics 32.

Corti, G., Van Wijk, J., Bonini, M., Sokoutis, D., Cloetingh, S., Innocenti, F., Manetti, P., 2003b. Transition from continental break-up to punctiform seafloor spreading: How fast, symmetric and magmatic. Geophys. Res. Lett. 30.

Coulié, E., Quidelleur, X., Courtillot, V., Lefèvre, J.C., Chiesa, S., 2003. Comparative K-Ar and Ar/Ar dating of Ethiopian and Yemenite Oligocene volcanism: Implications for timing and duration of the Ethiopian traps. Earth Planet. Sci. Lett. 206.

Courtillot, V., Jaupart, C., Manighetti, I., Tapponnier, P., Besse, J., 1999. On causal links between flood basalts and continental breakup. Earth Planet. Sci. Lett. 166.

Delvaux, D., Levi, K., Kajara, R., Sarota, J., 1992. Cenozoic paleostress and kinematic evolution of the Rukwa-North Malawi Rift Valley (East African Rift System). Bull. - Cent. Rech. Explor. Elf-Aquitaine 16.

Delvaux, D., Moeys, R., Stapel, G., Petit, C., Levi, K., Miroshnichenko, A., Ruzhich, V., San'kov, V., 1997. Paleostress reconstructions and geodynamics of the Baikal region, Central Asia, Part 2. Cenozoic rifting. Tectonophysics 282.

DeMets, C., Merkouriev, S., 2016. High-resolution estimates of Nubia-Somalia plate motion since 20 Ma from reconstructions of the Southwest Indian Ridge, Red Sea and Gulf of Aden. Geophys. J. Int. 207.

DeMets, C., Wilson, D.S., 2008. Toward a minimum change model for recent plate motions:

Calibrating seafloor spreading rates for outward displacement. Geophys. J. Int. 174.

Dhont, D., Chorowicz, J., 2006. Review of the neotectonics of the Eastern Turkish-Armenian Plateau by geomorphic analysis of digital elevation model imagery. Int. J. Earth Sci. 95.

Dugda, M.T., Nyblade, A.A., Julia, J., Langston, C.A., Ammon, C.J., Simiyu, S., 2005. Crustal structure in Ethiopia and Kenya from receiver function analysis: Implications for rift development in eastern Africa. J. Geophys. Res. Solid Earth 110.

Dunbar, J.A., Sawyer, D.S., 1988. Continental rifting at pre-existing lithospheric weaknesses. Nature 333.

Ebinger, C., 2005. Continental break-up: The East African perspective. Astron. Geophys. 46.

Ebinger, C.J., 1989. Tectonic development of the western branch of the East African rift system. Geol. Soc. Am. Bull. 101.

Ebinger, C.J., Casey, M., 2001. Continental breakup in magmatic provinces: An Ethiopian example. Geology 29.

Ebinger, C.J., Deino, A.L., Tesha, A.L., Becker, T., Ring, U., 1993a. Tectonic controls on rift basin morphology: evolution of the northern Malawi (Nyasa) Rift. J. Geophys. Res. 98.

Ebinger, C.J., Sleep, N.H., 1998. Cenozoic magmatism throughout east Africa resulting from impact of a single plume. Nature 395.

Ebinger, C.J., Yemane, T., Harding, D.J., Tesfaye, S., Kelley, S., Rex, D.C., 2000. Rift deflection, migration, and propagation: Linkage of the Ethiopian and Eastern rifts, Africa. Bull. Geol. Soc. Am. 112.

Ebinger, C.J., Yemane, T., Woldegabriel, G., Aronson, J.L., Walter, R.C., 1993b. Late Ecocene-Recent volcanism and faulting in the southern main Ethiopian rift. J. - Geol. Soc. 150.

Emishaw, L., Laó-Dávila, D.A., Abdelsalam, M.G., Atekwana, E.A., Gao, S.S., 2017. Evolution of the broadly rifted zone in southern Ethiopia through gravitational collapse and extension of dynamic topography. Tectonophysics 699.

Erbello, A., Corti, G., Agostini, A., Sani, F., Kidane, T., Buccianti, A., 2016. Modeling along-axis variations in fault architecture in the Main Ethiopian Rift: Implications for Nubia-Somalia kinematics. J. Geodyn. 102.

Fairhead, J.D., Henderson, N.B., 1977. The seismicity of southern Africa and incipient rifting. Tectonophysics 41.

Fernandes, R.M.S., Ambrosius, B.A.C., Noomen, R., Bastos, L., Combrinck, L., Miranda, J.M., Spakman, W., 2004. Angular velocities of Nubia and Somalia from continuous GPS data: Implications on present-day relative kinematics. Earth Planet. Sci. Lett. 222.

Fontijn, K., McNamara, K., Zafu Tadesse, A., Pyle, D.M., Dessalegn, F., Hutchison, W., Mather,

T.A., Yirgu, G., 2018. Contrasting styles of post-caldera volcanism along the Main Ethiopian Rift: Implications for contemporary volcanic hazards. J. Volcanol. Geotherm. Res. 356.

Franke, D., Jokat, W., Ladage, S., Stollhofen, H., Klimke, J., Lutz, R., Mahanjane, E.S., Ehrhardt, A., Schreckenberger, B., 2015. The offshore East African Rift System: Structural framework at the toe of a juvenile rift. Tectonics 34.

Fritz, H., Abdelsalam, M., Ali, K. A., Bingen, B., Collins, A. S., Fowler, A. R., & Viola, G. (2013). Orogen styles in the East African Orogen: a review of the Neoproterozoic to Cambrian tectonic evolution. Journal of African Earth Sciences, 86, 65-106.

Gani, N.D., Abdelsalam, M.G., Gera, S., Gani, M.R., 2009. Stratigraphic and structural evolution of the Blue Nile Basin, Northwestern Ethiopian Plateau. Geol. J. 44.

Gani, N.D.S., Gani, M.R., Abdelsalam, M.G., 2007. Blue Nile incision on the Ethiopian Plateau: Pulsed plateau growth, Pliocene uplift, and hominin evolution. GSA Today 17.

Geological Survey (U.S.), and EROS Data Center. 1900. EarthExplorer. [Reston, Va.]: U.S. Dept. of the Interior, U.S. Geological Survey.

George, R., 1998. Earliest magmatism in Ethiopia: Evidence for two mantle plumes in one flood basalt province. Geology 26.

George, R.M., Rogers, N.W., 2002. Plume dynamics beneath the African plate inferred from the geochemistry of the Tertiary basalts of southern Ethiopia. Contrib. to Mineral. Petrol. 144.

Grand, S.P., Van Der Hilst, R.D., Widiyantoro, S., 1997. Global seismic tomography: A snapshot of convection in the earth. GSA Today 7.

Gregory, J.W., 1894. Contributions to the Physical Geography of British East Africa. Geogr. J. 4.

Golden Software, LLC. PO Box 281 Golden, CO 80402-0281 USA.

Guiraud, R., Bosworth, W., Thierry, J., Delplanque, A., 2005. Phanerozoic geological evolution of Northern and Central Africa: An overview. J. African Earth Sci. 43.

Hanžl, P., & Verner, K. (eds.). 2018. Basic principles of geological and thematic mapping. Czech Geological Survey.

Hauber, E., Grott, M., Kronberg, P., 2010. Martian rifts: Structural geology and geophysics. Earth Planet. Sci. Lett. 294.

Hayward, N.J., Ebinger, C.J., 1996. Variations in the along-axis segmentation of the Afar Rift system. Tectonics 15.

Hetzel, R., Strecker, M.R., 1994. Late Mozambique Belt structures in western Kenya and their

influence on the evolution of the Cenozoic Kenya Rift. J. Struct. Geol. 16.

Hofmann, C., Courtillot, V., Féraud, G., Rochette, P., Yirgu, G., Ketefo, E., Pik, R., 1997. Timing of the ethiopian flood basalt event and implications for plume birth and global change. Nature 389.

Halcrow 2008: Rift Valley Lakes Basin Integrated Resources Development Master Plan Study Project, Phase 2 Report, Part II Prefeasibility Studies. Halcrow Group Limited and Generation Integrated Rural Development Consultants. Addis Ababa.

Hroch, T., Megerssa, L., (eds.) Buriánek, D., Verner, K., Martínek, K., Yakob, M., Janderková, J., Šíma, J., Kryštofová, E., Ali, Y., Tadesse, E., Legesse, F., Assefa, G., Valenta, J., Pécskay, Z., Hejtmánková P., Krejčí, Z. 2018: Explanatory notes to the thematic geoscientific maps of Ethiopia at a scale of 1 : 50,000, Map Sheet 0638-A2 Leku. 115 pages, 3 annexes, 4 maps. Czech Geological Survey, Prague; AQUATEST Ltd., Prague; Geological Survey of Ethiopia, Addis Ababa.

Hughes, G.W., Varol, O., Beydoun, Z.R., 1991. Evidence for Middle Oligocene rifting of the Gulf of Aden and for Late Oligocene rifting of the southern Red Sea. Mar. Pet. Geol. 8.

Ivanov, M.A., Head, J.W., 2015. The history of tectonism on Venus: A stratigraphic analysis. Planet. Space Sci. 113–114.

Janoušek, V., Farrow, C.M., Erban, V., 2006. Interpretation of whole-rock geochemical data in igneous geochemistry: Introducing Geochemical Data Toolkit (GCDkit). J. Petrol. 47.

Jestin, F., Huchon, P., Gaulier, J.M., 1994. The Somalia plate and the East African Rift System: present-day kinematics. Geophys. J. Int. 116.

Kampunzu, A.B., Mohr, P., 1991. Magmatic Evolution and Petrogenesis in the East African Rift System, in: Magmatism in Extensional Structural Settings.

Kassa, M., Alemu, A., Muluneh, A., 2021. Determination of gravity and isostatic Moho: Implications for the evolution of rifting in the central Main Ethiopian Rift. J. African Earth Sci. 184.

Kazmin, V., Shifferaw, A., Balcha, T., 1978. The Ethiopian basement: Stratigraphy and possible manner of evolution. Geol. Rundschau 67.

Kearey, P., Klepeis, K.A., Vine, F.J., Kearey, Klepeis, and V., 2009. Global Tectonics Third Edition, Science (New York, N.Y.).

Kebede, B., Mammo, T., 2021. Processing and interpretation of full tensor gravity anomalies of Southern Main Ethiopian Rift. Heliyon 7.

Kebede, F., Kulhánek, O., 1991. Recent seismicity of the East African Rift system and its implications. Phys. Earth Planet. Inter. 68.

Keir, D., Ebinger, C.J., Stuart, G.W., Daly, E., Ayele, A., 2006. Strain accommodation by

magmatism and faulting as rifting proceeds to breakup: Seismicity of the northern Ethiopian rift. J. Geophys. Res. Solid Earth 111.

Kendall, J.M., Stuart, G.W., Ebinger, C.J., Bastow, I.D., Keir, D., 2005. Magma-assisted rifting in Ethiopia. Nature 433.

Keranen, K., Klemperer, S.L., Gloaguen, R., Asfaw, L., Ayele, A., Ebinger, C., Furman, T., Harder, S., Keler, G.R., Mackenzie, G.D., Maguire, P.K.H., Stuart, G.W., 2004. Three-dimensional seismic imaging of a protoridge axis in the Main Ethiopian rift. Geology 32.

Keranen, K.M., Klemperer, S.L., Julia, J., Lawrence, J.F., Nyblade, A.A., 2009. Low lower crustal velocity across Ethiopia: Is the Main Ethiopian Rift a narrow rift in a hot craton? Geochemistry, Geophys. Geosystems 10.

Kieffer, B., Arndt, N., Lapierre, H., Bastien, F., Bosch, D., Pecher, A., Yirgu, G., Ayalew, D., Weis, D., Jerram, D.A., Keller, F., Meugniot, C., 2004. Flood and shield basalts from Ethiopia: Magmas from the African superswell. J. Petrol. 45.

Korme, T., Acocella, V., Abebe, B., 2004. The role of pre-existing structures in the origin, propagation and architecture of faults in the Main Ethiopian Rift. Gondwana Res. 7.

Korme, T., Chorowicz, J., Collet, B., Bonavia, F., 1997. Volcanic vents rooted on extension fractures and their geodynamic implications in the Ethiopian Rift. J. Volcanol. Geotherm. Res. 79.

La Rosa, A., Pagli, C., Wang, H., Doubre, C., Leroy, S., Sani, F., Corti, G., Ayele, A., Keir, D., 2021. Plate-Boundary Kinematics of the Afrera Linkage Zone (Afar) From InSAR and Seismicity. J. Geophys. Res. Solid Earth 126.

Leake, B.E., Woolley, A.R., Arps, C.E.S., Birch, W.D., Gilbert, M.C., Grice, J.D., Hawthorne, F.C., Kato, A., Kisch, H.J., Krivovichev, V.G., Linthout, K., Laird, J., Mandarino, J.A., Maresch, W. V., Nickel, E.H., Rock, N.M.S., Schumacher, J.C., Smith, D.C., Stephenson, N.C.N., Ungaretti, L., Whittaker, E.J.W., Youzhi, G., 1997. Nomenclature of amphiboles: Report of the subcommittee on amphiboles of the international mineralogical association, commission on new minerals and mineral names. Am. Mineral. 82.

Leakey, R.E.F., 1973. Evidence for an advanced plio-pleistocene hominid from East Rudolf, Kenya. Nature 242.

Leat, P., 1992. Magmatism and the causes of continental break-up. J. Geol. Soc. London. 149.

LeBas, M.J.L., Maitre, R.W.L., Streckeisen, A., Zanettin, B., 1986. A chemical classification of volcanic rocks based on the total alkali-silica diagram. J. Petrol. 27.

Lemaux, J., Gordon, R.G., Royer, J.Y., 2002. Location of the Nubia-Somalia boundary along the Southwest Indian Ridge. Geology 30.

Levitte, D., Columba, J., Mohr, P., 1974. Reconnaissance geology of the Amaro horst, Southern

Ethiopian rift. Bull. Geol. Soc. Am. 85.

Lucchitta, B.K., Isbell, N.K., Howington-Kraus, A., 1994. Topography of Valles Marineris: implications for erosional and structural history. J. Geophys. Res. 99.

Macgregor, D., 2015. History of the development of the East African Rift System: A series of interpreted maps through time. J. African Earth Sci.

Maerten, L., Maerten, F., Lejri, M., Gillespie, P., 2016. Geomechanical paleostress inversion using fracture data. J. Struct. Geol. 89.

Maguire, P.K.H., Keller, G.R., Klemperer, S.L., Mackenzie, G.D., Keranen, K., Harder, S., O'Reilly, B., Thybo, H., Asfaw, L., Khan, M.A., Amha, M., 2006. Crustal structure of the northern Main Ethiopian Rift from the EAGLE controlled-source survey; a snapshot of incipient lithospheric break-up. Geol. Soc. Spec. Publ. 259.

Mahatsente, R., Jentzsch, G., Jahr, T., 2000. Three-dimensional inversion of gravity data from the Main Ethiopian Rift. J. African Earth Sci. 31.

Mahatsente, R., Jentzsch, G., Jahr, T., 1999. Crustal structure of the Main Ethiopian Rift from gravity data: 3-dimensional modeling. Tectonophysics 313.

McConnell, R.B., 1972. Geological development of the rift system of eastern Africa. Bull. Geol. Soc. Am. 83.

McDonough, W.F., Sun, S. s., 1995. The composition of the Earth. Chem. Geol. 120.

McKenzie, D., 1978. Some remarks on the development of sedimentary basins. Earth Planet. Sci. Lett. 40.

Mickus, K., Tadesse, K., Keller, G.R., Oluma, B., 2007. Gravity analysis of the main Ethiopian rift. J. African Earth Sci. 48.

Mohr, P.A., Baker, B.H., Williams, L.A., 1972. Geology of the eastern rift system of Africa. Spec. Pap. Geol. Soc. Am. 136.

Mougenot, D., Recq, M., Virlogeux, P., Lepvrier, C., 1986. Seaward extension of the East African Rift. Nature 321.

Muluneh, A.A., Cuffaro, M., Doglioni, C., 2014. Left-lateral transtension along the Ethiopian rift and constrains on the mantle-reference plate motions. Tectonophysics 632.

Nemcok, M., Lisle Richard J, 1995. A stress inversion procedure for polyphase fault/slip data sets. J. Struct. Geol. 17.

Neumann, E. R., & Ramberg, I. B. (eds.). 2012. Petrology and Geochemistry of Continental Rifts: Volume One of the Proceedings of the NATO Advanced Study Institute Paleorift Systems with Emphasis on the Permian Oslo Rift, held in Oslo, Norway, July 27–August 5, 1977 (Vol. 36).

Nocquet, J.M., Willis, P., Garcia, S., 2006. Plate kinematics of Nubia - Somalia using a combined DORIS and GPS solution. J. Geod. 80.

Ogden, C.S., Keir, D., Bastow, I.D., Ayele, A., Marcou, S., Ugo, F., Woodward, A., Kibret, B.A., Gudbrandsson, S., 2021. Seismicity and Crustal Structure of the Southern Main Ethiopian Rift: New Evidence From Lake Abaya. Geochemistry, Geophys. Geosystems 22.

Olsen, K.H., 1995. Continental rifts: evolution, structure, tectonics, Continental rifts: evolution, structure, tectonics.

Oxburgh, E.R., Turcotte, D.L., 1974. Membrane tectonics and the East African Rift. Earth Planet. Sci. Lett. 22.

Pasteels, P., Villeneuve, M., De Paepe, P., Klerkx, J., 1989. Timing of the volcanism of the southern Kivu province: implications for the evolution of the western branch of the East African Rift system. Earth Planet. Sci. Lett. 94.

Pearce, J.A., 1996. A User's Guide to Basalt Discrimination Diagrams, in: Trace Element Geochemistry of Volcanic Rocks: Applications for Massive Sulfide Exploration.

Pearce, J.A., Norry, M.J., 1979. Petrogenetic implications of Ti, Zr, Y, and Nb variations in volcanic rocks. Contrib. to Mineral. Petrol. 69.

Philippon, M., Corti, G., Sani, F., Bonini, M., Balestrieri, M.L., Molin, P., Willingshofer, E., Sokoutis, D., Cloetingh, S., 2014. Evolution, distribution, and characteristics of rifting in southern Ethiopia. Tectonics 33.

Pik, R., Deniel, C., Coulon, C., Yirgu, G., Hofmann, C., Ayalew, D., 1998. The northwestern Ethiopian Plateau flood basalts: classification and spatial distribution of magma types. J. Volcanol. Geotherm. Res. 81.

Pik, R., Marty, B., Carignan, J., Yirgu, G., Ayalew, T., 2008. Timing of East African Rift development in southern Ethiopia: Implication for mantle plume activity and evolution of topography. Geology 36.

Pizzi, A., Coltorti, M., Abebe, B., Disperati, L., Sacchi, G., Salvini, R., 2006. The Wonji fault belt (Main Ethiopian Rift): Structural and geomorphological constraints and GPS monitoring. Geol. Soc. Spec. Publ. 259.

Pizzi, A., Domenica, A. Di, Komatsu, G., Cofano, A., Mitri, G., Bruzzone, L., 2017. Spreading vs. Rifting as modes of extensional tectonics on the globally expanded Ganymede. Icarus 288.

Pluijm, vand der B.A., Marshack, S., 2004. Earth structure. An introduction to structural geology and tectonics, Nature.

Prave, A.R., Bates, C.R., Donaldson, C.H., Toland, H., Condon, D.J., Mark, D., Raub, T.D., 2016. Geology and geochronology of the Tana Basin, Ethiopia: LIP volcanism, Super eruptions

and Eocene-Oligocene environmental change. Earth Planet. Sci. Lett. 443.

Rapprich, V., Žáček, V., Verner, K., Erban, V., Goslar, T., Bekele, Y., Legesa, F., Hroch, T., Hejtmánková, P., 2016. Wendo Koshe Pumice: The latest Holocene silicic explosive eruption product of the Corbetti Volcanic System (Southern Ethiopia). J. Volcanol. Geotherm. Res. 310.

Rapprich, V., (eds.) Čížek, D., Daniel, K., Legesa, F., Habtamu, B., Hroch, T., Kopačková, V, Málek, J., Malík, J., Mišurec, J., Orgoň, A., Šebesta, J., Šíma, J., Tsigehana, T., Verner, K., Yewubinesh, B. 2013: Set of Geoscience maps of Ethiopia at scale 1:50,000: Sub-sheet 0738-C4 Hawasa with Explanation booklet. 46 p. – Česká geologická služba, Praha; AQUATEST, Praha; Geological Survey of Ethiopia, Addis Ababa.

Redlands, C.E.S.R.I., 2011. ArcGIS Desktop: Release 10.6.1.

Ring, U., 2014. The East African rift system. Austrian J. Earth Sci. 107.

Ring, U., 1994. The influence of preexisting structure on the evolution of the Cenozoic Malawi rift (East African rift system). Tectonics 13.

Rochette, P., Tamrat, E., Féraud, G., Pik, R., Courtillot, V., Ketefo, E., Coulon, C., Hoffmann, C., Vandamme, D., Yirgu, G., 1998. Magnetostratigraphy and timing of the Oligocene Ethiopian traps. Earth Planet. Sci. Lett. 164.

Rogers, N.W., 2006. Basaltic magmatism and the geodynamics of the East African Rift System. Geol. Soc. Spec. Publ. 259.

Rogers, N.W., De Mulder, M., Hawkesworth, C.J., 1992. An enriched mantle source for potassic basanites: evidence from Karisimbi volcano, Virunga volcanic province, Rwanda. Contrib. to Mineral. Petrol. 111.

Rooney, T.O., 2020. The Cenozoic magmatism of East Africa: Part IV – The terminal stages of rifting preserved in the Northern East African Rift System. Lithos 360–361.

Rooney, T.O., 2017. The Cenozoic magmatism of East-Africa: Part I — Flood basalts and pulsed magmatism. Lithos 286–287.

Rooney, T.O., 2010. Geochemical evidence of lithospheric thinning in the southern Main Ethiopian Rift. Lithos 117.

Rooney, T.O., Hanan, B.B., Graham, D.W., Furman, T., Blichert-toft, J., Schilling, J.G., 2012. Upper mantle pollution during Afar plume-continental rift interaction. J. Petrol. 53.

Rosendahl, B.R., 1987. Architecture of continental rifts with special reference to East Africa. Annu. Rev. earth Planet. Sci. Vol. 15.

Royer, J.Y., Gordon, R.G., Horner-Johnson, B.C., 2006. Motion of Nubia relative to Antartica since 11 Ma: Implications for Nubia-Somalia, Pacific-North America, and India-Eurasia motion. Geology 34.

Saemundsson, K., 2010. East African Rift System - An overview, in: East African Rift System-An Overview, Short Course V on Exploration for Geothermal Reservoirs, United Nations Geothermal Training Programme-KenGen, Lake Bogoria and Lake Naivsha.

Saria, E., Calais, E., Stamps, D.S., Delvaux, D., Hartnady, C.J.H., 2014. Present-day kinematics of the East African Rift. J. Geophys. Res. Solid Earth 119.

Sengör, A.M.C., Burke, K., 1978. Relative timing of rifting and volcanism on Earth and its tectonic implications. Geophys. Res. Lett. 5.

Şengör, A.M.C., Natal'in, B.A., 2001. Rifts of the world. Spec. Pap. Geol. Soc. Am. 352.

Shackleton, R.M., 1986. Precambrian collision tectonics in Africa. Geol. Soc. Spec. Publ. 19.

Shinjo, R., Chekol, T., Meshesha, D., Itaya, T., Tatsumi, Y., 2011. Geochemistry and geochronology of the mafic lavas from the southeastern Ethiopian rift (the East African Rift System): Assessment of models on magma sources, plume-lithosphere interaction and plume evolution. Contrib. to Mineral. Petrol. 162.

Stamps, D.S., Calais, E., Saria, E., Hartnady, C., Nocquet, J.M., Ebinger, C.J., Fernandes, R.M., 2008. A kinematic model for the East African Rift. Geophys. Res. Lett. 35.

Stamps, D.S., Kreemer, C., Fernandes, R., Rajaonarison, T.A., Rambolamanana, G., 2021. Redefining East African Rift System kinematics. Geology 49.

Stern, R.J., 2002. Crustal evolution in the East African Orogen: A neodymium isotopic perspective. J. African Earth Sci. 34.

Stern, R.J., 1994. Arc assembly and continental collision in the Neoproterozoic East African Orogen: implications for the consolidation of Gondwanaland. Annu. Rev. Earth Planet. Sci. 22.

Stern, R.J., Ali, K.A., Abdelsalam, M.G., Wilde, S.A., Zhou, Q., 2012. U-Pb zircon geochronology of the eastern part of the Southern Ethiopian Shield. Precambrian Res. 206–207.

Stern, R.J., Dawoud, A.S., 1991. Late Precambrian (740 Ma) charnockite, enderbite, and granite from Jebel Moya, Sudan: a link between the Mozambique Belt and the Arabian-Nubian Shield. J. Geol. 99.

Stewart, K., Rogers, N., 1996. Mantle plume and lithosphere contributions to basalts from southern Ethiopia. Earth Planet. Sci. Lett. 139.

Stüwe, K., 2007. Geodynamics of the lithosphere: An introduction, Geodynamics of the Lithosphere: An Introduction.

Turcotte, D.L., Emerman, S.H., 1983. Mechanisms of active and passive rifting. Tectonophysics 94.

Ukstins, I.A., Renne, P.R., Wolfenden, E., Baker, J., Ayalew, D., Menzies, M., 2002. Matching

conjugate volcanic rifted margins: 40Ar/39Ar chrono-stratigraphy of pre- and syn-rift bimodal flood volcanism in Ethiopia and Yemen. Earth Planet. Sci. Lett. 198.

Verner, K., Buriánek, D., Svojtka, M., Peřestý, V., Megerssa, L., Tadesse, T., Kussita, A., Alemayehu, D., Hroch, T., 2021. Tectonometamorphic evolution and U–Pb dating of the high-grade Hammar Domain (Southern Ethiopian Shield); implications for the East-African Orogeny. Precambrian Res. 361.

Verner, K., Megerssa, L., (eds.) Hroch, T., Buriánek, D., Martínek, K., Yakob, M., Haregot, A., Janderková, J., Šíma, J., Kryštofová, E., Valenta, J., Bewketu, H., Mosisa, A., Balke, G., Assefa, G., Pécskay, Z., Hejtmánková, P., Krejčí, Z. 2018: Explanatory notes to the thematic geoscientific maps of Ethiopia at a scale of 1 : 50,000, Map Sheet 0638-D2 Mejo. 131 pages, 3 annexes, 4 maps. Czech Geological Survey, Prague; AQUATEST Ltd., Prague; Geological Survey of Ethiopia, Addis Ababa.

Versfelt, J., Rosendahl, B.R., 1989. Relationships between pre-rift structure and rift architecture in Lakes Tanganyika and Malawi, East Africa. Nature 337.

Wernicke, B., 1981. Low-angle normal faults in the Basin and Range Province: Nappe tectonics in an extending orogen.

White, R.S., 1992. Magmatism during and after continental break-up. Geol. Soc. Spec. Publ. 68.

Winchester, J.A., Floyd, P.A., 1977. Geochemical discrimination of different magma series and their differentiation products using immobile elements. Chem. Geol. 20.

WoldeGabriel, G., Aronson, J.L., 1987. Chow Bahir rift: A “failed” rift in southern Ethiopia. Geology 15.

Woldegabriel, G., Aronson, J.L., Walter, R.C., 1990. Geology, geochronology, and rift basin development in the central sector of the Main Ethiopia Rift. Bull. Geol. Soc. Am. 102.

WoldeGabriel, G., Yemane, T., Suwa, G., White, T., Asfaw, B., 1991. Age of volcanism and rifting in the Burji-Soyoma area, Amaro Horst, southern Main Ethiopian Rift: geo- and biochronologic data. J. African Earth Sci. 13.

Wolfenden, E., Ebinger, C., Yirgu, G., Deino, A., Ayalew, D., 2004. Evolution of the northern Main Ethiopian rift: Birth of a triple junction. Earth Planet. Sci. Lett. 224.

Worku, H., Schandelmeier, H., 1996. Tectonic evolution of the Neoproterozoic Adola Belt of southern Ethiopia: Evidence for a Wilson Cycle process and implications for oblique plate collision. Precambrian Res. 77.

Yirgu, G., Ebinger, C.J., Maguire, P.K.H., 2006. The Afar volcanic province within the East African Rift System: Introduction. Geol. Soc. Spec. Publ. 259, 1–6.

Žáček, V. - Rapprich, V. - Aman, Y. - Berhanu, B. - Čížek, D. - Dereje, K. - Erban, V. - Ezra, T. -

Legesa, F. - Habtamu, M. - Hroch, T. - Kopačková V. - Kycl, P. - Mišurec, J. - Orgoň, A. - Pécskay, Z. - Šíma, J. - Tarekegu, D. - Verner, K. 2014. Explanation Booklet of the set of Geoscience maps of Ethiopia at scale 1: 50 00, Subsheet 0738-D3 Shashemene: Geological map, Hydrogeological map, Geohazards map. Neuveden. 52 s. – Czech Geological Survey, Prague, AQUATEST a.s., Prague, Geological Survey of Ethiopia, Addis Ababa. Praha.

Zhao, D., 2001. Seismic structure and origin of hotspots and mantle plumes. Earth Planet. Sci. Lett. 192.

Ziegler, P.A., Cloetingh, S., 2004. Dynamic processes controlling evolution of rifted basins. Earth-Science Rev. 64.

Annexes:

Annexes-1. Geological map of Sidama area

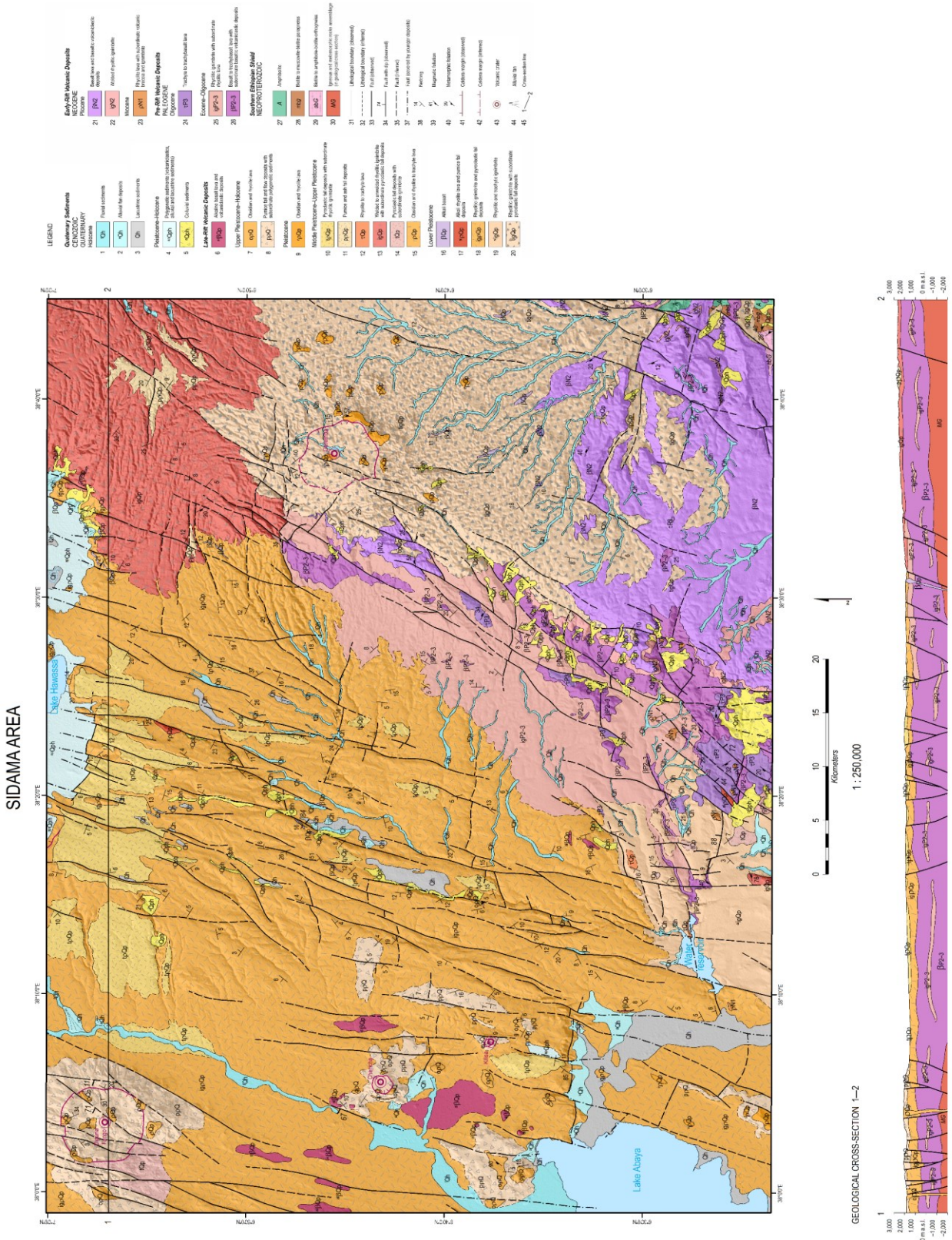

Annexes-2. Geological map of Gamo area

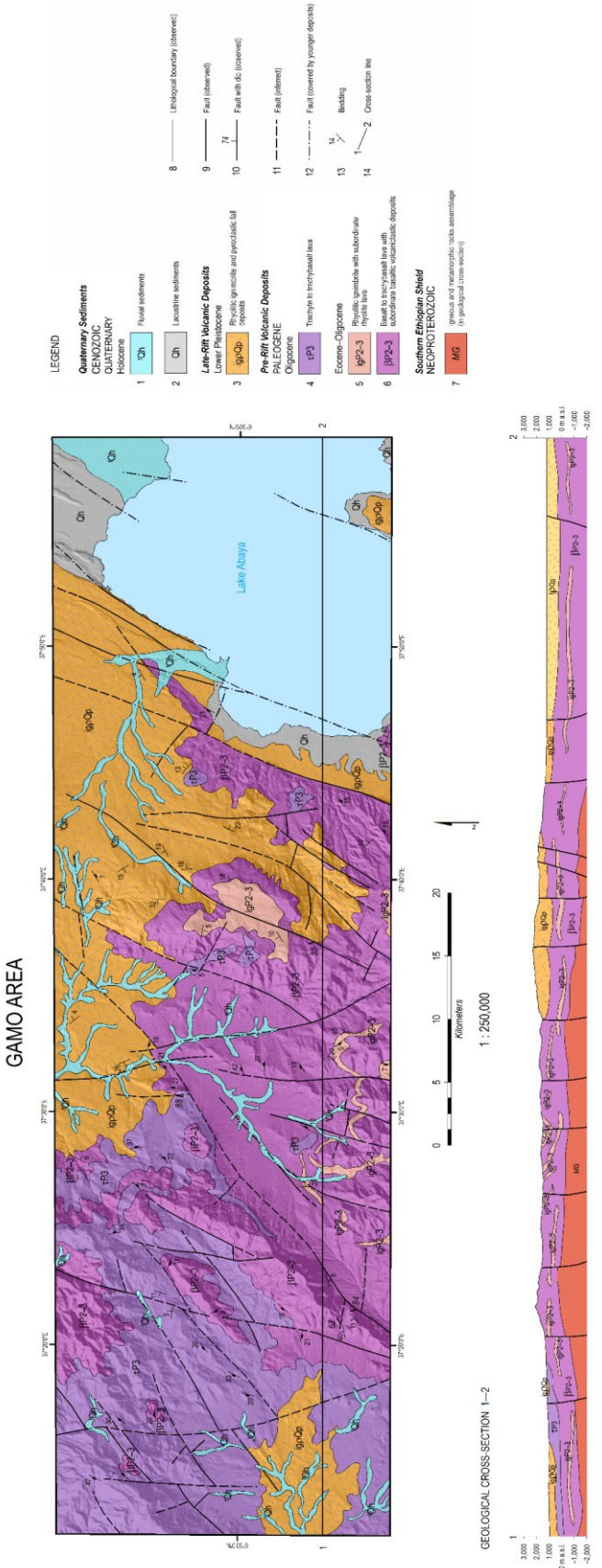

Annexes-3. Lithostratigraphic scheme for geological map of Sidama, after (Verner and Megerssa eds., in print).

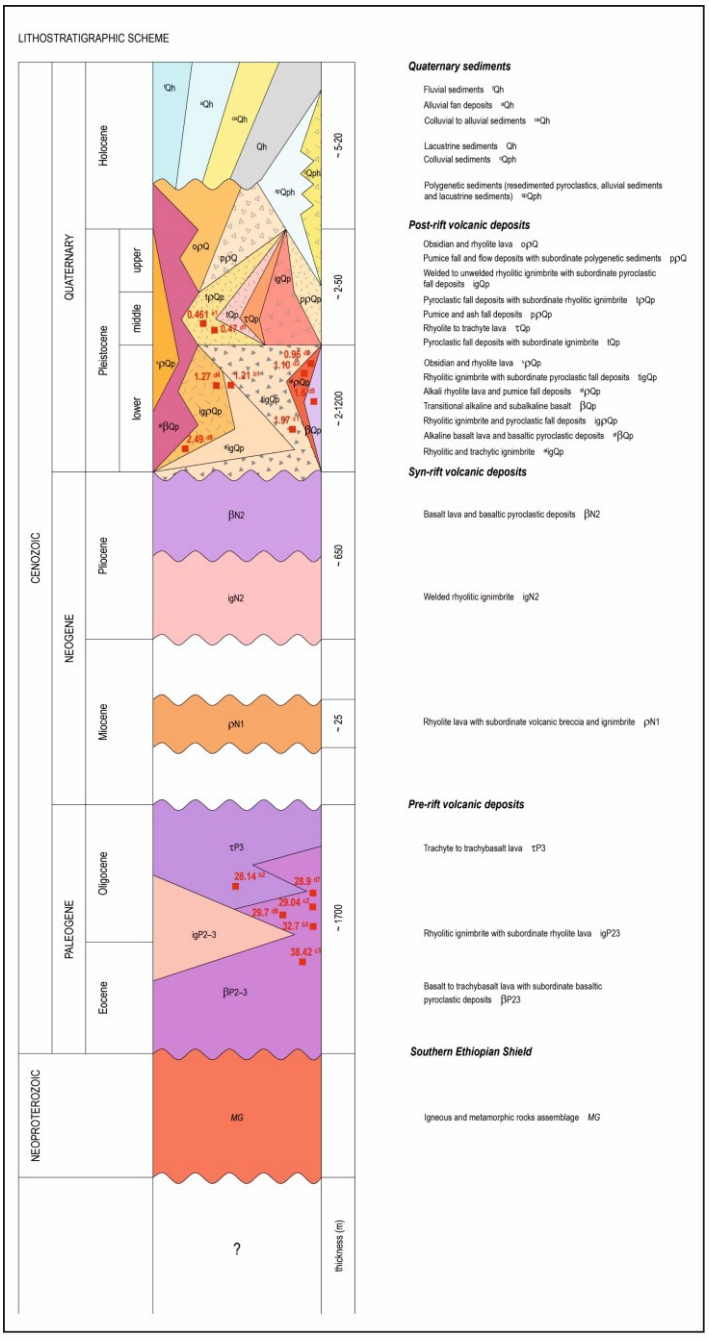

Annex-4. Topographic map with selected area of study.

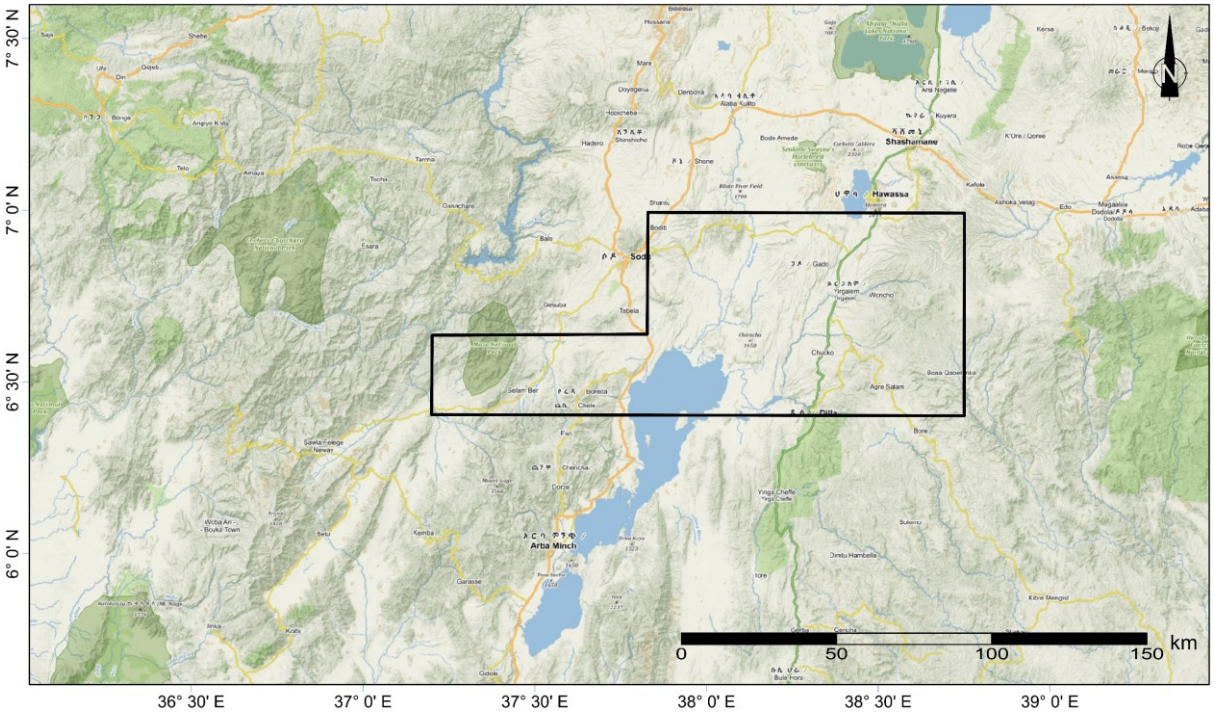

Annex-5. Map of field observation points for Sidama.

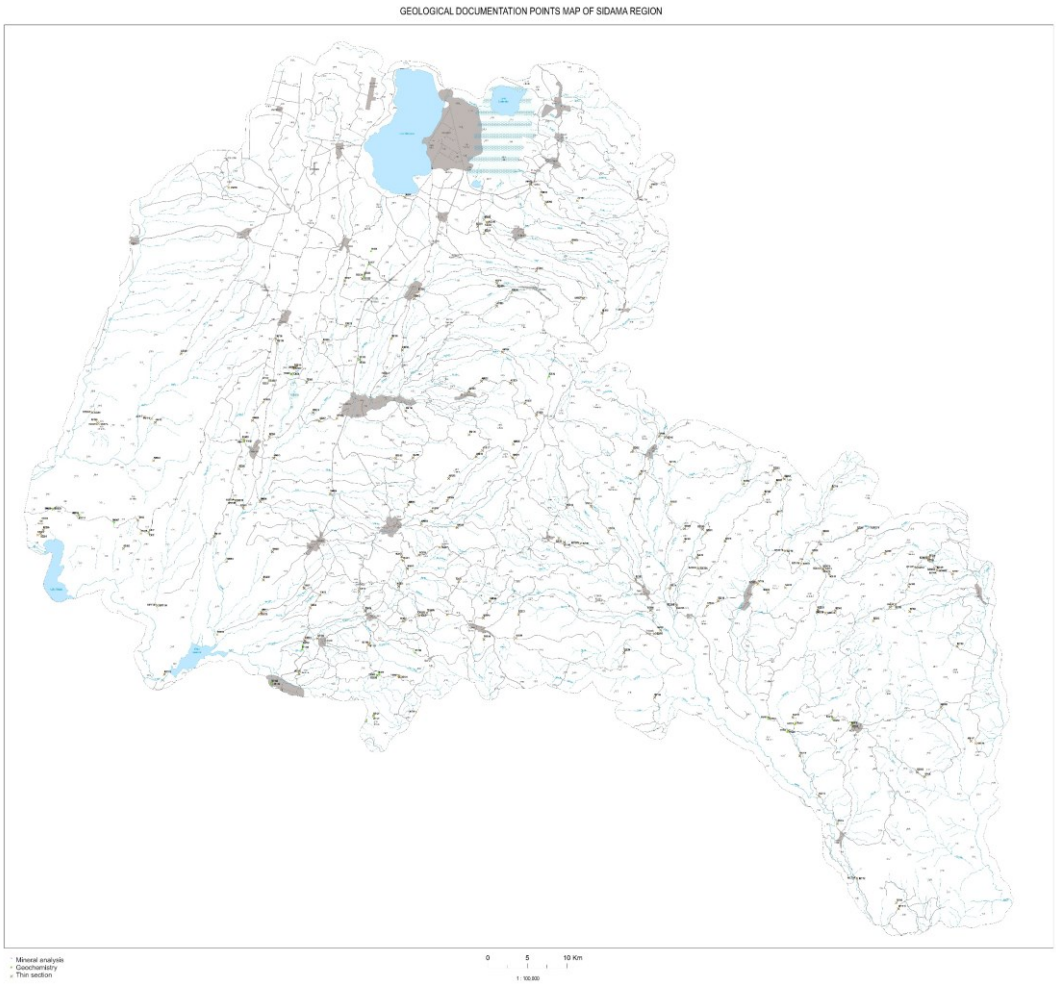

Table 1. Whole-rock compositions of volcanic rocks (oxide wt. % for major elements and ppm for trace elements).

Sample	DE001	DE025	DE035	KE001	TE028	DE201	DE525
rock	ignimbrite	ignimbrite	rhyolite	trachyte	rhyolite	basalt	Rhyolite
map	Leku	Leku	Leku	Leku	Leku	Leku	Boricha
lithology	Rhyolitic ignimbrite and pyroclastic fall deposits	Rhyolitic ignimbrite and pyroclastic fall deposits	Alkali rhyolite lava and pumice fall deposits	Alkali rhyolite lava and pumice fall deposits	Alkali rhyolite lava and pumice fall deposits	Alkali basalt	Alkali rhyolite lava and pumice fall deposits
wt %							
SiO2	75.13	71.94	73.16	73.97	73.66	45.39	74.2
Al2O3	10.9	10.39	12.76	12.27	12.52	15.05	11.95
Fe2O3	3.46	4.88	2.57	2.83	2.77	13.1	2.82
MgO	0.09	0.14	0.16	0.14	0.14	5.64	0.12
CaO	0.24	0.19	0.16	0.15	0.14	10.11	0.11
Na2O	4.63	4.19	4.93	4.41	4.69	2.8	4.84
K2O	4.57	4.88	5.18	5.03	5.04	0.87	5
TiO2	0.22	0.34	0.35	0.31	0.33	2.95	0.3
P2O5	0.01	0.01	0.02	0.01	0.02	0.36	0.02
MnO	0.14	0.2	0.13	0.14	0.14	0.2	0.13
Cr2O3	<0.002	<0.002	<0.002	<0.002	<0.002	0.008	<0.002
LOI	0.4	2.5	0.4	0.6	0.4	3.2	0.3
Sum	99.78	99.71	99.81	99.82	99.82	99.73	99.76
ppm							
Mo	1.4	0.2	0.1	0.3	0.4	0.6	<0.1
Cu	0.5	1.4	0.2	<0.1	0.1	44.2	0.3
Pb	3.6	2.2	15.3	16.5	13.4	0.7	12.8
Zn	26	42	14	10	32	82	17
Ni	0.6	1.1	0.2	0.2	0.3	49.6	0.1
As	<0.5	<0.5	<0.5	0.5	<0.5	<0.5	<0.5
Cd	0.1	0.2	0.2	<0.1	<0.1	<0.1	<0.1
Sb	<0.1	<0.1	<0.1	0.1	<0.1	<0.1	0.1
Bi	<0.1	<0.1	<0.1	<0.1	<0.1	<0.1	<0.1
Ag	<0.1	<0.1	<0.1	<0.1	<0.1	<0.1	<0.1
Au	0.7	<0.5	<0.5	<0.5	<0.5	0.8	<0.5
Hg	<0.01	<0.01	<0.01	<0.01	<0.01	<0.01	<0.01
Tl	<0.1	<0.1	<0.1	<0.1	<0.1	<0.1	<0.1
Se	<0.5	<0.5	0.7	<0.5	<0.5	<0.5	<0.5

Table 1. (continued)

Sample	BZ015	TD011	BM014	BM007	BM009	AT012
rock	Basalt	Obsidian	Basalt (Qh)	Pumice	Rhyolite	Rhyolite
map	Kilisa	Kilisa	Kilisa	Kilisa	Kilisa	Wijirga
lithology	Alkaline basalt lava and basaltic volcaniclastic deposits	Pumice fall and flow deposits with subordinate polygenetic sediments	Alkaline basalt lava and basaltic volcaniclastic deposits	Pumice fall and flow deposits with subordinate polygenetic sediments	Pumice fall and flow deposits with subordinate polygenetic sediments	Welded to unwelded rhyolitic ignimbrite with subordinate pyroclastic fall deposits
wt %						
SiO2	44.44	70.33	45.19	66.83	69.44	73.38
Al2O3	14.58	10.98	14.01	10.63	10.46	12.4
Fe2O3	12.34	5.92	13.5	6.44	7.41	2.82
MgO	6.24	0.27	7.9	0.26	0.23	0.15
CaO	10.36	0.28	11	0.31	0.25	0.14
Na2O	2.68	6.02	2.56	4.55	5.02	4.63
K2O	0.92	4.83	0.68	5.44	4.89	5.03
TiO2	2.75	0.48	2.92	0.49	0.51	0.33
P2O5	0.61	0.04	0.5	0.04	0.01	0.01
MnO	0.19	0.3	0.19	0.3	0.27	0.13
Cr2O3	0.03	<0.002	0.038	<0.002	<0.002	<0.002
LOI	4.5	0.2	1.2	4.4	1.2	0.8
Sum	99.7	99.68	99.7	99.69	99.71	99.79
ppm						
Mo	0.3	<0.1	0.2	0.1	0.1	<0.1
Cu	20.9	<0.1	20.6	0.3	0.3	0.3
Pb	1.4	0.2	0.3	0.8	14.8	13.3
Zn	75	4	63	13	134	19
Ni	118.2	0.2	67.1	0.7	1.1	0.2
As	<0.5	<0.5	<0.5	<0.5	<0.5	<0.5
Cd	<0.1	<0.1	<0.1	<0.1	<0.1	<0.1
Sb	<0.1	<0.1	<0.1	<0.1	<0.1	<0.1
Bi	<0.1	<0.1	<0.1	<0.1	<0.1	<0.1
Ag	<0.1	<0.1	<0.1	<0.1	<0.1	<0.1
Au	<0.5	1	<0.5	0.6	<0.5	2.9
Hg	<0.01	<0.01	<0.01	<0.01	0.02	<0.01
Tl	<0.1	<0.1	<0.1	<0.1	<0.1	<0.1
Se	<0.5	<0.5	<0.5	<0.5	<0.5	<0.5

Table 2. Trace element analyses of volcanic rocks (ppm).

Sample	DE001	DE025	DE035	KE001	TE028	DE201	DE525
Ba	17	150	10	16	24	272	3
Sc	5	4	6	6	6	25	6
Be	5	7	3	4	6	<1	3
Co	6.7	3	4.3	2.1	2.6	44.9	1.1
Cs	0.6	1.5	0.4	0.4	0.2	<0.1	0.2
Ga	25.5	26.9	25.4	26.2	27.8	17.9	27.9
Hf	22.1	27.6	18.8	22.6	20.8	4.1	23.4
Nb	109.7	145.7	95	106.1	99	22.7	113
Rb	99.9	122.9	119.2	143.6	134.5	20	160.6
Sn	6	8	6	6	7	1	7
Sr	8.6	14	3	3.2	3.6	527.4	1.3
Ta	6.9	8.7	5.8	6.8	6.8	1.5	7
Th	14.8	16.7	14.7	17.3	16.6	1.6	18
U	3.6	4.7	2.4	2.2	2	0.5	1.5
V	8	<8	<8	8	<8	321	<8
W	35.2	10.1	20.6	9.6	13.8	4.8	5.3
Zr	890.9	1140.3	770	891.4	746.3	144.5	940.1
Y	91.6	122.9	69.2	72.1	53	26.1	62.3
La	102.2	135.5	94.8	48.2	85.3	19.9	38.7
Ce	211	268.9	176	150.4	149.6	45.6	90.2
Pr	24.58	31.35	21.54	11.95	21.89	5.5	9.33
Nd	93.4	117	79.3	44.2	76.6	25	36.4
Sm	18.07	22.59	14.88	9.23	13.95	5.36	7.5
Eu	1.55	3.39	1.87	1.09	1.54	2.11	0.9
Gd	16.48	21.97	13.56	10.27	10.9	6.01	8.36
Tb	2.74	3.66	2.23	1.89	1.82	0.88	1.49
Dy	16.32	21.7	13.46	12.45	11.01	5.03	9.76
Ho	3.37	4.49	2.67	2.74	2.16	0.92	2.13
Er	9.49	13.36	8.03	8.29	6.84	2.49	6.89
Tm	1.46	2.01	1.22	1.27	1.06	0.33	1.08
Yb	9.72	12.72	8	8.53	7.58	2.07	7.46
Lu	1.49	1.99	1.25	1.32	1.21	0.28	1.2

Table 2. (continued)

Sample	BZ015	TD011	BM014	BM007	BM009	AT012
Ba	377	9	365	9	24	5
Sc	26	8	26	8	8	6
Be	<1	5	<1	4	8	3
Co	56.8	5.5	52.3	1.6	1	0.8
Cs	0.3	1.3	<0.1	1.1	0.5	0.2
Ga	14.9	30.9	13.6	31.2	33.8	26.8
Hf	4	25.6	2.5	23.7	26.3	20.2
Nb	25.3	193.9	18.7	193.8	200.6	102.5
Rb	17.3	135	8.3	126.3	137.7	127.8
Sn	2	7	<1	7	8	6
Sr	584.8	1	541.9	2.1	4.2	2.5
Ta	1.6	11	1.1	10.8	12	6.3
Th	1.6	19.4	1	15.5	18	15.2
U	0.2	4.5	0.4	3.9	0.4	1.7
V	290	<8	290	<8	<8	<8
W	2.9	29.8	5.8	6.7	3	2.2
Zr	165.7	1058.7	102.2	993.1	1101.8	844.7
Y	26.4	103.3	24.6	110.3	56	83
La	26.3	149.5	23.2	148.4	125.8	70.8
Ce	52.6	281.5	40.4	275.2	158	111.1
Pr	6.89	32.16	5.53	32.16	27.28	15.87
Nd	29.4	115.8	24.9	116.3	91.7	57
Sm	6.43	20.54	5.28	21.59	15.37	11.07
Eu	2.32	3.56	2.05	3.87	2.55	1.26
Gd	6.49	19.09	5.81	19.49	11.13	10.42
Tb	0.93	3.2	0.82	3.35	1.94	1.88
Dy	5.25	19.38	4.65	20.46	11.53	12.53
Ho	1.02	3.95	0.89	4.25	2.32	2.83
Er	2.78	11.58	2.34	12.19	7.08	8.77
Tm	0.36	1.69	0.3	1.78	1.09	1.34
Yb	2.14	10.78	1.75	11.38	7.6	8.82
Lu	0.31	1.64	0.25	1.73	1.24	1.38

Table 3. Representative chemical composition of feldspars.

Number	1	38	8	50	110	65	60	103	44
Sample	BZ132	NG037	DE037	DE521	DE522	AM027	BZ126	AM66	DE523A
wt%									
SiO_2	66.88	62.25	66.94	66.97	66.36	67.22	66.17	50.54	66.87
$P2O_5$	0.02	0.07	0.00	0.00	0.00	0.00	0.00	0.09	0.01
$Al2O_3$	17.61	22.57	18.06	17.89	17.62	18.19	19.04	30.26	17.88
FeO	1.11	0.73	0.76	0.87	1.07	0.74	0.49	1.05	1.14
CaO	0.00	4.72	0.00	0.00	0.00	0.03	0.35	13.86	0.00
Na_2O	6.94	7.49	6.18	6.23	6.14	7.16	7.76	3.43	5.93
K2O	6.44	1.74	7.98	7.53	7.80	6.35	5.16	0.11	7.92
BaO	0.00	0.15	0.00	0.02	0.00	0.02	0.11	0.00	0.00
Rb_2O	0.00	0.00	0.00	0.00	0.00	0.00	0.00	0.00	0.00
Total	98.999	99.57	99.921	99.482	98.999	99.687	98.957	99.325	99.735
Si	3.033	2.795	3.015	3.031	3.019	3.020	2.979	2.323	3.026
Al	0.941	1.194	0.958	0.954	0.945	0.963	1.010	1.639	0.953
Fe	0.042	0.028	0.029	0.033	0.041	0.028	0.018	0.040	0.043
P	0.001	0.003	0.000	0.000	0.000	0.000	0.000	0.003	0.000
T-site	4.017	4.019	4.002	4.018	4.005	4.011	4.008	4.006	4.023
K	0.373	0.100	0.459	0.435	0.453	0.364	0.297	0.006	0.457
Na	0.610	0.652	0.539	0.547	0.542	0.624	0.677	0.305	0.520
Ca	0.000	0.227	0.000	0.000	0.000	0.001	0.017	0.682	0.000
Ba	0.000	0.003	0.000	0.000	0.000	0.000	0.002	0.000	0.000
Rb	0.000	0.000	0.000	0.000	0.000	0.000	0.000	0.000	0.000
O-site	0.983	0.981	0.998	0.982	0.995	0.989	0.992	0.994	0.977
An	0	23	0	0	0	0	2	69	0
Ab	62	67	54	56	54	63	68	31	53
Or	38	10	46	44	46	37	30	1	47

Table 4. Representative chemical composition of pyroxenes.

Number	30	25	26	27	16	17	33	35	36	42	58
Sample	DE522A-30	DE522A-25	DE522A-26	DE522A-27	DE522A-16	DE522A-17	NG037-3	NG037-5	NG037-6	NG037-12	NG037-28
wt%											
SiO_2	51.83	51.77	51.66	50.46	51.77	51.54	52.32	52.49	51.64	51.57	52.18
TiO_2	1.02	1.58	2.23	0.43	1.14	1.05	0.34	0.48	0.93	0.92	0.43
Al_2O_3	0.24	0.29	0.36	0.19	0.25	0.20	1.45	1.96	1.44	1.53	2.01
Cr_2O_3	0.01	0.01	0.00	0.00	0.00	0.00	0.02	0.02	0.00	0.00	0.00
FeO	30.40	29.82	29.08	29.77	29.95	30.07	20.58	17.58	13.40	13.46	19.74
MnO	0.16	0.15	0.39	0.85	0.15	0.23	0.91	0.70	0.77	0.82	0.82
MgO	0.00	0.00	0.01	0.20	0.00	0.02	22.43	24.20	14.99	15.28	22.40
CaO	1.15	0.95	2.88	8.93	0.99	1.60	1.70	2.02	16.06	15.83	1.95
Na2O	12.10	12.42	11.21	7.31	12.18	11.81	0.06	0.05	0.31	0.36	0.05
K2O	0.00	0.00	0.01	0.00	0.00	0.00	0.00	0.01	0.03	0.03	0.02
Si	2.010	2.001	2.002	2.005	2.015	2.011	1.944	1.929	1.947	1.937	1.938
Al	0.000	0.000	0.000	0.000	0.000	0.000	0.056	0.071	0.053	0.063	0.062
Al	0.011	0.013	0.017	0.009	0.012	0.009	0.007	0.014	0.011	0.005	0.027
$Fe(^{2+})$	0.819	0.823	0.693	0.518	0.811	0.801	0.034	0.033	0.012	0.033	0.015
$Fe(^{2+})$	0.167	0.141	0.249	0.471	0.163	0.180	0.606	0.507	0.410	0.390	0.598
Cr	0.000	0.000	0.000	0.000	0.000	0.000	0.001	0.000	0.000	0.000	0.000
Ti	0.030	0.046	0.065	0.013	0.033	0.031	0.009	0.013	0.026	0.026	0.012
Mn	0.005	0.005	0.013	0.029	0.005	0.008	0.029	0.022	0.025	0.026	0.026
Mg	0.000	0.000	0.000	0.012	0.000	0.001	1.243	1.326	0.843	0.856	1.240
Ca	0.048	0.039	0.120	0.380	0.041	0.067	0.068	0.079	0.649	0.637	0.078
Na	0.910	0.931	0.842	0.563	0.919	0.893	0.004	0.003	0.023	0.026	0.004
K	0.000	0.000	0.000	0.000	0.000	0.000	0.000	0.001	0.001	0.001	0.001
TOTAL	4	4	4	4	4	4	4	4	4	4	4

Table 5. Representative chemical composition of olivines.

Number	14	15	16	1	89	90	94	95	105	106
Sample	BZ132-OL14	BZ132-ol15	BZ132-ol16	DE037	AM66-8	AM66-9	AM66-13	AM66-14	AM66-24	AM66-25
wt%										
SiO_2	29.92	29.58	29.87	29.35	38.96	39.33	39.00	39.08	39.25	39.22
TiO_2	0.11	0.08	0.63	0.04	0.04	0.06	0.04	0.04	0.03	0.03
Al_2O_3	0.00	0.17	0.19	0.07	0.03	0.04	0.06	0.07	0.04	0.06
Cr_2O_3	0.01	0.00	0.02	0.00	0.03	0.01	0.00	0.02	0.02	0.00
FeO	62.34	55.92	55.47	66.07	18.77	18.11	17.39	17.04	17.75	17.74
MnO	6.31	4.92	4.95	0.00	0.25	0.27	0.26	0.25	0.27	0.25
MgO	2.85	2.08	2.12	3.25	41.67	41.71	43.11	42.64	42.65	42.47
NiO										
CaO	0.19	0.18	0.17	0.78	0.25	0.24	0.25	0.23	0.24	0.27
TOTAL	101.71	92.94	93.42	99.56	99.99	99.77	100.12	99.35	100.24	100.04
Si	0.982	1.040	1.039	0.980	0.997	1.004	0.991	0.998	0.997	0.998
Ti	0.003	0.002	0.016	0.001	0.001	0.001	0.001	0.001	0.001	0.001
Al	0.000	0.007	0.008	0.003	0.001	0.001	0.002	0.002	0.001	0.002
Cr	0.000	0.000	0.000	0.000	0.001	0.000	0.000	0.000	0.000	0.000
$Fe^{(2+)}$	1.710	1.643	1.614	1.844	0.401	0.387	0.369	0.364	0.377	0.377
Mn	0.175	0.147	0.146	0.000	0.005	0.006	0.006	0.005	0.006	0.005
Mg	0.139	0.109	0.110	0.162	1.589	1.588	1.633	1.623	1.614	1.611
Ni	0.000	0.000	0.000	0.000	0.000	0.000	0.000	0.000	0.000	0.000
Ca	0.007	0.007	0.006	0.028	0.007	0.007	0.007	0.006	0.006	0.007
TOTAL	3.016	2.955	2.940	3.018	3.002	2.994	3.008	3.000	3.002	3.001
Endmembers										
Fo	7	6	6	8	80	80	81	81	81	81
Fa	84	87	86	92	20	20	18	18	19	19
Tp	9	8	8	0	0	0	0	0	0	0

Table 6. Representative chemical composition of amphiboles.

Number	15	20	21	23	24	31	40	41
Sample	DE522A-15	DE522A-20	DE522A-21	DE522A-23	DE522A-24	DE522A-31	DE523A	DE523A
wt%								
SiO_2	48.351	48.461	48.577	48.897	48.875	48.572	48.514	48.23
$P2O_5$	0.04	0	0.04	0.014	0.012	0.017	0	0.026
TiO_2	1.502	1.462	1.443	1.369	1.362	1.351	1.736	1.742
Al_2O_3	0.814	0.828	0.751	0.701	0.725	0.724	0.887	0.923
Cr_2O_3	0	0	0	0	0	0	0.02	0.028
MnO	1.279	1.325	1.337	1.375	1.371	1.331	0	0
FeO	33.548	33.196	34.052	34.645	34.998	34.555	31.179	31.744
ZnO	0.106	0.07	0.069	0.052	0.006	0.045	0.109	0
MgO	1.015	1.161	0.966	0.617	0.646	0.784	3.013	2.731
CaO	3.469	3.576	3.013	2.588	2.626	2.844	4.44	4.467
Na_2O	6.34	6	6.297	6.492	6.397	6.191	5.315	5.162
K_2O	1.29	1.285	1.351	1.299	1.329	1.394	1.299	1.293
F	1.189	1.097	1.096	1.076	1.037	1.074	1.43	1.409
Cl	0.014	0.028	0.022	0.004	0.01	0.021	0.035	0.022
O=F,Cl (calc)	-0.5	-0.47	-0.47	-0.45	-0.44	-0.46	-0.61	-0.6
Initial Total	98.457	98.019	98.544	98.679	98.954	98.443	97.367	97.177
Normalization procedures used for average formula (apfu)	Si–Mg&Li =13 Si–K=16	Si–Ca&Li= 15 Si–Mg&Li =13 Si–K=16	Si–Mg&Li =13 Si–K=16	Si–Ca&Li= 15 Si–Mg&Li =13 Si–K=16	Si–Mg&Li =13 Si–K=16	Si–Ca&Li= 15 Si–Mg&Li =13 Si–K=16	Si–Ca&Li= 15 Si–Mg&Li =13 Si–K=16	Si–Ca&Li= 15 Si–Mg&Li =13 Si–K=16
Group	OH,F,Cl	OH,F,Cl	OH,F,Cl	OH,F,Cl	OH,F,Cl	OH,F,Cl	OH,F,Cl	OH,F,Cl
Subgroup of (OH,F,Cl)	Na-Ca	Na-Ca	Na-Ca	Na-Ca	Na-Ca	Na-Ca	Na-Ca	Na-Ca
Species	ferro-ferri-katophorite	ferro-ferri-katophorite	ferro-ferri-katophorite	ferro-ferri-katophorite	ferro-ferri-katophorite	ferro-ferri-katophorite	ferro-ferri-katophorite	ferro-ferri-katophorite
T (ideally 8 apfu)								
Si	7.784	7.829	7.799	7.864	7.814	7.835	7.794	7.779
P	0.003		0.003	0.001	0.001	0.001		0.002
Al	0.154	0.158	0.142	0.133	0.137	0.138	0.168	0.175
Ti	0.058	0.013	0.057	0.002	0.049	0.026	0.038	0.044
Fe3+								
T subtotal	7.999	8	8.001	8	8.001	8	8	8
C (ideally 5 apfu)								
Ti	0.123	0.165	0.118	0.164	0.115	0.138	0.172	0.168
Al								
Cr							0.003	0.004
Fe3+	0.322	0.208	0.409	0.291	0.484	0.304	0.173	0.192
Zn	0.013	0.008	0.008	0.006	0.001	0.005	0.013	
Mn2+	0.103	0.062	0.071	0.022	0.051	0.007		
Fe2+	4.195	4.277	4.163	4.368	4.195	4.358	3.918	3.981
Mg	0.244	0.28	0.231	0.148	0.154	0.189	0.722	0.657
C subtotal	5	5	5	4.999	5	5.001	5.001	5.002
B (ideally 2 apfu)								
Mn2+	0.071	0.119	0.111	0.165	0.134	0.175		
Fe2+							0.099	0.11
Ca	0.598	0.619	0.518	0.446	0.45	0.492	0.764	0.772
Na	1.331	1.262	1.371	1.389	1.416	1.333	1.137	1.118
B subtotal	2	2	2	2	2	2	2	2
A (from 0 to 1 apfu)								
Na	0.649	0.618	0.589	0.635	0.567	0.603	0.519	0.496
K	0.265	0.265	0.277	0.267	0.271	0.287	0.266	0.266
A subtotal	0.914	0.883	0.866	0.902	0.838	0.89	0.785	0.762
O (non-W)	22	22	22	22	22	22	22	22
W (ideally 2 apfu)								
OH	1.391	1.432	1.438	1.452	1.473	1.446	1.264	1.275
F	0.605	0.561	0.556	0.547	0.524	0.548	0.727	0.719
Cl	0.004	0.008	0.006	0.001	0.003	0.006	0.01	0.006
W subtotal	2	2.001	2	2	2	2	2.001	2

Table 6. (continued)

Number	49	51	118	119	121	122	123	124	80
Sample	DE523A	DE523A	DE522	DE522	DE522	DE522	DE522	DE522	BZ126
wt%									
SiO_2	47.773	48.177	47.452	47.583	47.261	48.197	47.48	47.605	51.847
$P2O_5$	0	0.016	0.007	0	0	0	0	0.015	0
TiO_2	1.686	1.641	2.162	1.98	2.021	1.966	2.035	1.487	1.602
Al_2O_3	0.994	0.896	0.969	0.984	0.998	0.807	0.975	0.953	1.804
Cr_2O_3	0	0.015	0	0	0	0.002	0.007	0.01	0.005
MnO	0.005	0	0	0.013	0	0.004	0	0.01	0
FeO	31.692	34.069	32.619	32.313	32.305	33.089	31.358	34.043	10.996
ZnO	0.078	0.04	0.106	0.039	0.042	0.063	0.033	0.095	0.008
MgO	2.575	1.588	1.454	1.773	1.822	1.107	2.427	0.961	15.91
CaO	4.317	4.003	3.966	4.108	4.028	3.581	4.277	3.686	5.622
Na_2O	5.373	5.378	5.501	5.632	5.634	5.681	5.417	5.62	6.476
K_2O	1.234	1.258	1.376	1.299	1.29	1.307	1.324	1.342	1.344
F	1.482	1.331	1.3	1.43	1.356	1.363	1.499	1.34	3.721
Cl	0.027	0.016	0.034	0.025	0.037	0.033	0.021	0.028	0.012
O=F,Cl (calc)	-0.63	-0.56	-0.56	-0.61	-0.58	-0.58	-0.64	-0.57	-1.57
Initial Total	96.606	97.868	96.386	96.569	96.214	96.62	96.213	96.625	97.777
Normalization procedures used for average formula (apfu)	Si–Ca&Li=15 Si–Mg&Li=13 Si–K=16	Si–Ca&Li=15 Si–Mg&Li=13 Si–K=16	Si–Ca&Li=15 Si–Mg&Li=13 Si–K=16	Si–Ca&Li=15 Si–Mg&Li=13 Si–K=16	Si–Ca&Li=15 Si–Mg&Li=13 Si–K=16	Si–Ca&Li=15 Si–Mg&Li=13 Si–K=16	Si–Ca&Li=15 Si–Mg&Li=13 Si–K=16	Si–Ca&Li=15 Si–Mg&Li=13 Si–K=16	Si–Mg&Li=13 Si–K=16
Group	OH,F,Cl	OH,F,Cl	OH,F,Cl	OH,F,Cl	OH,F,Cl	OH,F,Cl	OH,F,Cl	OH,F,Cl	OH,F,Cl
Subgroup of (OH,F,Cl)	Na-Ca	Na-Ca	Na-Ca	Na-Ca	Na-Ca	Na-Ca	Na-Ca	Na-Ca	Na-Ca
Species	ferro-ferri-katophorite	ferro-ferri-katophorite	ferro-ferri-katophorite	ferro-ferri-katophorite	ferro-ferri-katophorite	ferro-ferri-katophorite	ferro-ferri-katophorite	ferro-ferri-katophorite	fluoro-richterite
T (ideally 8 apfu)									
Si	7.768	7.781	7.781	7.78	7.757	7.877	7.76	7.82	7.652
P		0.001						0.001	
Al	0.19	0.171	0.187	0.19	0.193	0.123	0.188	0.179	0.314
Ti	0.042	0.047	0.032	0.03	0.05		0.052		0.035
Fe3+									
T subtotal	8	8	8	8	8	8	8	8	8.001
C (ideally 5 apfu)									
Ti	0.165	0.152	0.235	0.214	0.199	0.242	0.198	0.184	0.143
Al						0.032		0.006	
Cr		0.002					0.001	0.001	0.001
Fe3+	0.19	0.249	0.134	0.125	0.147	0.131	0.14	0.202	0.138
Zn	0.009	0.005	0.013	0.005	0.005	0.008	0.004	0.012	0.001
Mn2+									
Fe2+	4.012	4.21	4.263	4.225	4.203	4.317	4.065	4.36	1.217
Mg	0.624	0.382	0.355	0.432	0.446	0.27	0.591	0.235	3.5
C subtotal	5	5	5	5.001	5	5	4.999	5	5
B (ideally 2 apfu)									
Mn2+	0.001			0.002		0.001		0.001	
Fe2+	0.108	0.143	0.076	0.069	0.084	0.074	0.08	0.115	0.002
Ca	0.752	0.693	0.697	0.72	0.708	0.627	0.749	0.649	0.889
Na	1.139	1.164	1.227	1.209	1.208	1.298	1.171	1.235	1.109
B subtotal	2	2	2	2	2	2	2	2	2
A (from 0 to 1 apfu)									
Na	0.555	0.52	0.522	0.576	0.585	0.502	0.546	0.555	0.744
K	0.256	0.259	0.288	0.271	0.27	0.273	0.276	0.281	0.253
A subtotal	0.811	0.779	0.81	0.847	0.855	0.775	0.822	0.836	0.997
O (non-W)	22	22	22	22	22	22	22	22	22
W (ideally 2 apfu)									
OH	1.23	1.316	1.316	1.254	1.286	1.286	1.219	1.296	0.26
F	0.762	0.68	0.674	0.739	0.704	0.704	0.775	0.696	1.737
Cl	0.007	0.004	0.009	0.007	0.01	0.009	0.006	0.008	0.003
W subtotal	1.999	2	1.999	2	2	1.999	2	2	2

Table 6. (continued)

Number	75	85	28	29	30	40	49	104
Sample	126(Cordier	BZ126b	DE521_28	DE521_29	DE521_30	DE521_40	DE521_49	AM66-23
wt%								
SiO_2	52.409	50.186	47.284	46.267	41.176	46.84	46.666	44.287
$P2O_5$	0	0	0	0.007	0.012	0.011	0.014	0.052
TiO_2	1.592	2.157	1.955	1.867	1.978	1.91	1.897	2.781
Al_2O_3	1.405	2.815	1.335	1.38	1.136	1.472	1.519	17.313
Cr_2O_3	0.003	0.005	0	0	0.006	0	0.019	0.005
MnO	0	0.005	1.62	1.677	1.514	1.604	1.527	0.005
FeO	12.082	10.267	30.671	30.334	36.863	30.314	29.477	12.631
ZnO	0.041	0	0.042	0.092	0.158	0.033	0.059	0.01
MgO	15.164	16.525	2.69	2.859	2.346	2.947	3.494	1.131
CaO	4.913	6.424	4.917	4.949	4.993	5.262	5.39	2.186
Na_2O	6.763	5.874	5.478	5.71	5.725	5.303	5.555	0.392
K_2O	1.382	1.297	1.055	1.151	0.816	1.119	1.026	0.749
F	3.663	3.616	2.177	2.362	2.137	1.808	2.712	0
Cl	0	0.025	0.04	0.025	0.009	0.029	0.046	0.227
O=F,Cl (calc)	-1.54	-1.53	-0.93	-1	-0.9	-0.77	-1.15	-0.05
Initial Total	97.877	97.666	98.334	97.68	97.969	97.882	98.251	81.719
Normalization procedures used for average formula (apfu)	Si–Mg&Li =13 Si–K=16	Si–Mg&Li =13 Si–K=16	Si–Ca&Li= 15 Si–Mg&Li =13 Si–K=16	Si–Mg&Li =13 Si–K=16	Si–Mg&Li =13 Si–K=16	Si–Ca&Li= 15 Si–Mg&Li =13 Si–K=16	Si–Mg&Li =13 Si–K=16	Si–Ca&Li= 15 Si–Na=15
Group	OH,F,Cl	OH,F,Cl	OH,F,Cl	OH,F,Cl	OH,F,Cl	OH,F,Cl	OH,F,Cl	OH,F,Cl
Subgroup of (OH,F,Cl)	Na-Ca	Na-Ca	Na-Ca	Na-Ca	Na-Ca	Na-Ca	Na-Ca	Ca
Species	fluoro-richterite	fluoro-richterite	ferro-fluoro-richterite	ferro-fluoro-richterite	ferro-ferri-fluoro-katophorite	ferro-richterite	ferro-fluoro-richterite	Ti-rich ferro-tschermakite
T (ideally 8 apfu)								
Si	7.748	7.4	7.617	7.506	6.745	7.567	7.513	7.334
P					0.001	0.001	0.001	0.004
Be								
Al	0.245	0.489	0.253	0.264	0.219	0.28	0.288	0.662
Ti	0.007	0.111	0.13	0.228	0.244	0.152	0.198	
Fe3+				0.001	0.792			
T subtotal	8	8	8	7.999	8.001	8	8	8
C (ideally 5 apfu)								
Ti	0.17	0.128	0.107			0.08	0.032	0.346
Al								2.717
Cr		0.001			0.001		0.002	0.001
Fe3+	0.129	0.224	0.193	0.415	1.146	0.19	0.304	
Zn	0.004		0.005	0.011	0.019	0.004	0.007	0.001
Mn2+			0.11	0.183	0.149	0.111	0.152	
Fe2+	1.354	1.015	3.938	3.699	3.112	3.906	3.664	1.656
Mg	3.342	3.632	0.646	0.691	0.573	0.71	0.839	0.279
C subtotal	4.999	5	4.999	4.999	5	5.001	5	5
B (ideally 2 apfu)								
Mn2+		0.001	0.111	0.047	0.061	0.108	0.057	0.001
Fe2+	0.01	0.027						0.094
Ca	0.778	1.015	0.849	0.86	0.876	0.911	0.93	0.388
Na	1.212	0.957	1.041	1.092	1.063	0.981	1.014	0.126
B subtotal	2	2	2.001	1.999	2	2	2.001	0.609
A (from 0 to 1 apfu)								
Na	0.727	0.722	0.67	0.704	0.755	0.68	0.72	
K	0.261	0.244	0.217	0.238	0.171	0.231	0.211	0.158
A subtotal	0.988	0.966	0.887	0.942	0.926	0.911	0.931	0.158
O (non-W)	22	22	22	22	22	22	22	22
W (ideally 2 apfu)								
OH	0.287	0.308	0.88	0.781	0.89	1.068	0.607	1.936
F	1.713	1.686	1.109	1.212	1.107	0.924	1.381	
Cl		0.006	0.011	0.007	0.002	0.008	0.013	0.064
W subtotal	2	2	2	2	1.999	2	2.001	2

Table 6. (continued)

Number	95	82	83	86	91	93	96	97	102
Sample	BZ126d	AM066-1	AM66-2	AM66-5	AM66-10	AM66-12	AM66-15	AM66-16	AM66-21
wt%									
SiO_2	43.244	46.245	46.18	46.437	46.72	42.779	46.356	46.419	46.547
$P2O_5$	0.016	0.411	0.414	0.386	0.388	0.299	0.421	0.385	0.418
TiO_2	0.282	2.426	2.483	2.502	2.47	2.301	2.511	2.541	2.481
Al_2O_3	22.593	15.946	15.848	16.014	16.014	14.725	16.488	15.932	15.911
Cr_2O_3	0	0	0	0.007	0	0	0.01	0	0.001
MnO	0	0.207	0.155	0.185	0.202	0.158	0.201	0.193	0.208
FeO	14.705	11.948	12.02	11.975	11.757	14.424	11.949	11.859	11.794
ZnO	0.175	0.054	0.018	0.061	0	0.065	0	0	0.023
MgO	4.11	7.16	7.248	7.001	7.254	9.274	6.231	7.089	7.195
CaO	1.001	9.829	9.77	9.786	9.748	5.252	10.036	9.815	9.889
Na_2O	0.063	3.014	2.885	2.974	2.908	2.07	2.927	2.956	2.98
K_2O	1.262	0.464	0.447	0.433	0.46	0.352	0.49	0.47	0.454
F	0	0	0	0	0	0	0	0	0
Cl	0	0.014	0.038	0.022	0.017	0.061	0.018	0.023	0.008
O=F,Cl (calc)	0	0	-0.01	0	0	-0.01	0	-0.01	0
Initial Total	87.451	97.718	97.496	97.783	97.938	91.75	97.638	97.672	97.909
Normalization procedures used for average formula (apfu)	Si–Ca&Li=15 Si–Na=15	Si–Ca&Li=15 Si–Mg&Li=13	Si–Ca&Li=15 Si–Mg&Li=13	Si–Ca&Li=15 Si–Mg&Li=13	Si–Ca&Li=15 Si–Mg&Li=13 Si–Na=15	Si–Ca&Li=15 Si–Na=15	Si–Ca&Li=15 Si–Mg&Li=13 Si–Na=15	Si–Ca&Li=15 Si–Mg&Li=13	Si–Ca&Li=15 Si–Mg&Li=13
Group	OH,F,Cl	OH,F,Cl	OH,F,Cl	OH,F,Cl	OH,F,Cl	OH,F,Cl	OH,F,Cl	OH,F,Cl	OH,F,Cl
Subgroup of (OH,F,Cl)	Mg-Fe-Mn	Ca	Ca	Ca	Na-Ca	Na-Ca	Ca	Ca	Ca
Species	grunerite	tschermakite	tschermakite	tschermakite	barroisite	barroisite	ferro-tschermakite	tschermakite	tschermakite
T (ideally 8 apfu)									
Si	6.749	6.673	6.676	6.689	6.705	6.579	6.687	6.691	6.693
P	0.001	0.025	0.025	0.024	0.024	0.019	0.026	0.023	0.025
Be									
Al	1.25	1.302	1.299	1.287	1.271	1.401	1.288	1.286	1.282
Ti									
Fe3+									
T subtotal	8	8	8	8	8	7.999	8.001	8	8
C (ideally 5 apfu)									
Ti	0.033	0.263	0.27	0.271	0.267	0.266	0.272	0.276	0.268
Al	2.906	1.41	1.401	1.432	1.438	1.267	1.515	1.421	1.415
Cr				0.001			0.001		
Fe3+					0.001	0.079			
Zn	0.02	0.006	0.002	0.006		0.007			0.002
Mn2+		0.025	0.019	0.023	0.025		0.025	0.024	0.025
Fe2+	1.084	1.442	1.453	1.443	1.411	1.254	1.441	1.43	1.418
Mg	0.956	1.54	1.562	1.503	1.552	2.126	1.34	1.523	1.542
C subtotal	4.999	4.686	4.707	4.679	4.694	4.999	4.594	4.674	4.67
B (ideally 2 apfu)									
Mn2+						0.021			
Fe2+	0.835					0.523			
Ca	0.167	1.52	1.513	1.51	1.499	0.865	1.551	1.516	1.524
Na	0.019	0.48	0.487	0.49	0.501	0.591	0.449	0.484	0.476
B subtotal	1.021	2	2	2	2	2	2	2	2
A (from 0 to 1 apfu)									
Na		0.363	0.322	0.341	0.308	0.026	0.37	0.342	0.354
K	0.251	0.085	0.082	0.08	0.084	0.069	0.09	0.086	0.083
A subtotal	0.251	0.448	0.404	0.421	0.392	0.095	0.46	0.428	0.437
O (non-W)	22	22	22	22	22	22	22	22	22
W (ideally 2 apfu)									
OH	2	1.997	1.991	1.995	1.996	1.984	1.996	1.994	1.998
F									
Cl		0.003	0.009	0.005	0.004	0.016	0.004	0.006	0.002
W subtotal	2	2	2	2	2	2	2	2	2

Table 7. List of observation points and analyzed samples with applied methods.

Sample	Rock type	Coordinates (WGS84)		Methods	
Number		Northing	Easting	Thin section	Geochemistry
BZ158	Bi to Bi-Ms paragneiss	6.33692167	39.0462933		
NG30	orthogneiss	6.398095	39.0497117		
BZ176	Quartz dike	6.173648	38.993979		
BZ174	amphibolite	6.157028	38.97073		
BZ184	basalts to trachybasalts	6.520413	39.00474		
AM032	basalts to trachybasalts	6.77088667	38.5236967	X	
AM009	rhyolitic ignimbrite	6.69461333	38.5372317		
BZ152	trachyte to trabasalt	6.557835	39.0214017		
BZ126	trachyte	6.57358	38.985675	X	
BZ087	welded ignimbrite	6.454315	38.5995883		
TD021	basalt	6.50263667	38.4524633		
AM027	welded ignimbrite	6.74544	38.57358	X	
BZ132	welded ignimbrite	6.69160167	38.697195	X	
BZ225	welded ignimbrite	6.54021833	38.839505		
TD023	unwelded ignimbrite	6.525925	38.3391917		
KE409	welded ignimbrite	6.7036567	38.25173		
DE037	pyroclastic fall deposits	6.885616	38.366883	X	
NG037	alkaline basalt	6.95269	38.53142	X	
DE522	obsidiane lava	6.9519	38.087301	X	
DE522A	pyroclastic deposits	6.9519	38.087301	X	
DE521	trachyte lava	6.978821	38.063548	X	
SD006	rhyolite lava	6.977817	38.063422		
DE523A	pyroclastic fall deposits	6.955471	38.089696	X	
BZ228	welded ignimbrite	6.94786833	38.5192533		
BZ239	pumice and ash fall deposits	6.91102833	38.6742833		
BZ238	paleo-soil	6.91066333	38.6751333		
AM066	pyroclastic fall deposits	6.992125	38.23386	X	
SD005	pumice fall and flow deposits	6.985281	38.060131		
SD002	obsidiane lava	6.6211953	38.0253478		
BZ297	alkaline basalt	6.721725	38.08528		
BZ296	fluvial sediment	6.73445667	38.0782933		
BZ264	unwelded ignimbrite	6.76446333	38.34654		
BZ199	basalt	6.52225167	39.0081717		
KE407	pyroclastic fall deposits	6.5906728	38.1266667		
BZ175	orthogneiss	6.149308	38.988686		
SD024	basalt	6.040913	37.408071		
DE201	Alkali basalt	6.770039	38.279723		X
BZ015	Alkaline basalt lava and basaltic volcaniclastic deposits	6.634152	38.242548		
TD011	Pumice fall and flow deposits with subordinate polygenetic sediments	6.597387	38.1431		X
BM014	Alkaline basalt lava and basaltic volcaniclastic deposits	6.616895	38.06287		X
BM007	Pumice fall and flow deposits with subordinate polygenetic sediments	6.60866	38.10349		X
BM009	Pumice fall and flow deposits with subordinate polygenetic sediments	6.623813	38.03357		X
AT012	Welded to unwelded rhyolitic ignimbrite with subordinate pyroclastic fall deposits	6.776457	38.60112		X
DE001	Rhyolitic ignimbrite and pyroclastic fall deposits	6.979804	38.434856		X
DE025	Rhyolitic ignimbrite and pyroclastic fall deposits	6.794189	38.3829		X
DE035	Alkali rhyolite lava and pumice fall deposits	6.890604	38.388507		X
KE001	Alkali rhyolite lava and pumice fall deposits	6.905176	38.393443		X
TE028	Alkali rhyolite lava and pumice fall deposits	6.920864	38.397185		X
DE525	Alkaline basalt lava and basaltic volcaniclastic deposits	6.376384	38.354111		X

Table. 8. Physical properties of rocks for gravimetry analysis.

Sample	mineralogical (calculated)	porosity	gain_size	texture	main minerals	minor minerals	accesories
BE002	density	Percentage	fine grained	nonwelded	Qtz, Pl, glass	-	-
BM009	(g.cm-3)	(%)	fine grained	panxenomorphic	Qtz, Pl, Kfs	-	Opq
BM014	2.333805691	57.29125668	fine grained	ophitic	Pl, Px, glass	Ol	Opq
BZ014	2.687893356	19.31772818	glassy	welded	Qtz, Pl, glass	Kfs	-
BZ015A	3.008106441	18.22047244	fine grained	spherulitic	Pl, Kfs, Qtz	Amp	-
DE246	2.518773703	29.72949525	medium grained	lepidogranoblastic	Qtz, Pl, Kfs	Bt, Ep	-
DE259	2.565713772	10.65927575	glassy	welded	Qtz, Pl, glass	-	Opq
DE260	2.736812192	0.368570271	fine grained	ophitic	Pl, Cpx	-	Mag
DE269	2.661517832	18.39846833	glassy	hyaloophitic	Pl, glass, Cpx	-	Opq
DE412	2.924820698	1.259867634	fine grained	lepidoblastic	Ms	Qtz, Pl, Ky	Ap, Mag
DE427A	2.874521111	2.941238041	fine grained	trachytic	Kfs, Pl	glass	-
DE428	2.727636862	6.493047372	fine grained	trachytic	Pl, Px	glass, Kfs	Mag
DE462	2.639029003	4.125351703	glassy	welded	Pl, Kfs, glass	lithic fragment	
DE489	2.667904858	0.955538222	medium grained	garnoblastic	Pl, Cpx	Kfs	Ttn, Ap
DE489B	2.444815452	12.75602528	medium grained	granoblastic	Qtz, Pl, Amp	Px	Ttn, Ap, Mag
DE501	2.897842242	0.426864847	medium grained	symplectitic	Grt, Pl, Amp	Bt	Ap, Opq
DE507	2.902462283	0.620283558	medium grained	granoblastic	Qtz, Pl, Amp	Px	Ttn, Ap
DE508	3.011420912	6.064053203	medium grained	garnoblastic	Kfs, Qtz, Pl	Bt	Ms, Ap, Zr
DE554	2.833501052	0.800496983	fine grained	-	-	-	-
DE559	2.63746336	1.54437516	fine grained	-	-	-	-
DE561	2.858895603	1.567990748	fine grained	-	-	-	-
DE602	2.909214901	0.769343137	fine grained	-	-	-	-
DE610	2.853749607	2.400744056	fine grained	vesicular	-	-	-
DE611	2.666446751	1.105854887	fine grained	ophitic	Pl, Px, glass		Opq
E006B	2.731607569	41.51693025	medium grained	granoblastic	Px, Pl	Qtz, Amp, Scp	Opq, Ap
E011	2.80907027	1.404684998	medium grained	nematoblastic	Amp	Px, Scp	Ap
E050B	2.851798756	1.786388225	fine grained	porphyritic	Pl, glass	Px, Kfs	Opq
E052	3.103521321	0.503826099	glassy	porphyritic	Pl, glass	Px	Opq
E053	2.78378226	10.7270449	fine grained	porphyritic	Pl, glass	Px	Opq
E055	2.827327489	1.146279155	fine grained	porphyritic	Pl, glass	Px, Kfs, Amp	Opq
E061	2.835845952	5.042562527	medium grained	granonematoblastic	Px, Amp	-	Opq
KV230A	2.680202562	15.10241413	medium grained	lepidoblastic	Tc	Atg	Mag
MB007	3.270300007	2.012153363	-	vesicular	Pl, Kfs, glass	-	-
TD007	2.722795494	3.282491446	glassy	welded	Qtz, Pl, glass	Kfs	-
TD011	1.943595835	66.58531759	glassy	-	Pl, glass	Amp	-

Table 9. Results of paleostress analysis from ROCK 2019 software.

*** Program ROCK2019 *** J.M.2019
data file : E1 total 35 data correct 35 data

Phase : E1_f1
****

	alfa	beta	gama	psi
Results	-0.0070	-0.6400	0.0317	1.8734
Error	0.0086	0.0087	0.0071	0.2833

Main plane : 0 90

Tensor result

-0.345	-0.007	0.032
-0.007	-0.640	-0.640
0.032	-0.640	0.985

Eigen numbers	vl[1]	vl[2]	vl[3]	fi	azi
1.208	-0.022	0.346	-1.000	70.857	356.370
-0.346	1.000	0.014	-0.017	0.989	89.220
-0.862	0.008	-1.000	-0.347	19.115	179.563

Parameter R = 0.249

Phase : E1_f2
****

	alfa	beta	gama	psi
Results	0.0578	-0.8800	-1.1200	3.1416
Error	0.0118	0.0128	0.0645	0.4614

Main plane : 0 90

Tensor result

-0.999	0.058	-1.120
0.058	0.543	-0.880
-1.120	-0.880	0.456

Eigen numbers	vl[1]	vl[2]	vl[3]	fi	azi
1.660	0.439	0.810	-1.000	47.347	28.445
0.015	0.564	-1.000	-0.562	26.097	150.566
-1.675	-1.000	-0.218	-0.615	31.020	257.696

Parameter R = 0.507

Fit of angle
****

Cis	f	D	P	Ds	Ps	Or	Od1	Str1	Or1	Od2	Str2	Or2	Od3	Str3	Or3
1	0	91	72	123	69	N	36.8	18	N	162.2	71	R			
2	1	96	88	180	72	N	13.7	64	N	169.9	47	R			
3	1	100	83	129	82	N	7.4	41	N	159.9	55	R			
4	1	102	81	153	76	N	15.2	33	N	157.7	57	R			
5	1	105	76	137	74	N	16.0	18	N	134.0	60	R			
6	1	109	86	170	82	N	4.9	41	N	150.4	50	R			
7	1	111	85	111	85	N	10.8	37	N	136.9	49	R			
8	1	112	76	163	69	N	19.3	15	N	128.5	53	R			
9	1	118	82	133	82	N	6.4	27	N	118.9	45	R			
10	1	118	68	77	62	N	12.8	3	N	71.6	42	N			
11	0	121	86	43	71	N	34.4	36	N	101.5	41	R			